HZDR-101

# ULTRAFAST RESPONSE OF PHOTOEXCITED CARRIERS IN TRANSITION METAL OXIDES UNDER HIGH PRESSURE

Johannes Martin Braun

Wissenschaftlich-Technische Berichte
HZDR-101 · ISSN 2191-8708

WISSENSCHAFTLICH-
TECHNISCHE BERICHTE

HZDR

HELMHOLTZ
ZENTRUM DRESDEN
ROSSENDORF

Wissenschaftlich-Technische Berichte
**HZDR-101**

Johannes Martin Braun

# ULTRAFAST RESPONSE OF PHOTOEXCITED CARRIERS IN TRANSITION METAL OXIDES UNDER HIGH PRESSURE

HZDR
HELMHOLTZ
ZENTRUM DRESDEN
ROSSENDORF

Druckausgabe: ISSN 2191-8708

Elektronische Ausgabe: ISSN 2191-8716

https://www.hzdr.de/publications/Publ-29324

urn:nbn:de:bsz:d120-qucosa2-341882

Die vorliegende Arbeit wurde sowohl als Dissertation an der Fakultät Mathematik und Naturwissenschaften der Technischen Universität Dresden sowie als Wissenschaftlich-Technischer Bericht des Helmholtz-Zentrum Dresden – Rossendorf mit der Berichtsnummer **HZDR-101** veröffentlicht.

2019

Herausgegeben vom

Helmholtz-Zentrum Dresden - Rossendorf

Bautzner Landstraße 400

01328 Dresden

Germany

# Ultrafast Response of Photoexcited Carriers in Transition Metal Oxides under High Pressure

## Dissertation

zur Erlangung des akademischen Grades
Doctor rerum naturalium
(Dr. rer. nat.)

durchgeführt am
Helmholtz-Zentrum Dresden-Rossendorf

vorgelegt
dem Bereich Mathematik und Naturwissenschaften
der Technischen Universität Dresden

von
M. Sc. Johannes Martin Braun
geboren in Bayreuth

Die Dissertation wurde in der Zeit von Juli 2014 bis September 2018 am Institut für Ionenstrahlphysik und Materialforschung des Helmholtz-Zentrum Dresden-Rossendorf (HZDR) angefertigt.

Eingereicht am: 19.12.2018
Verteidigt am: 21.05.2019

Erstgutachter: Prof. Dr. Manfred Helm (Technische Universität Dresden & HZDR)
Zweitgutachter: Prof. Dr. Jure Demsar (Johannes Gutenberg-Universität Mainz)

# Abstract

In this work, optical pump – near-infrared probe and near-infrared pump – mid-infrared probe spectroscopy are used for the investigation of pressure-induced insulator-to-metal transitions in transition metal oxide compounds. The materials under study are $\alpha$-$Fe_2O_3$, also known as hematite, and $VO_2$. Both materials undergo pressure-induced metallization. However, the physical mechanisms of this phase transition are very different for these systems and have not been fully understood up to now. Using ultrafast pump-probe spectroscopy we obtain an insight into the evolution of the band structure and electron dynamics across the insulator-to-metal transition.

In the case of $VO_2$, our near-infrared pump – mid-infrared probe experiments reveal a non-vanishing pumping threshold for photo-induced metallization even at our highest pressures around 20 GPa. This demonstrates the existence of localized charge carriers and the corresponding persistence of a band gap. Besides the threshold behaviour for photo-induced metallization, the carrier relaxation time scale, and the linear reflectivity and transmissivity have been studied under pressure increase. An anomaly in the threshold behaviour as well as the linear reflectivity and transmissivity at a critical pressure around 7 GPa indicates band gap filling under pressure. This is further supported by results obtained under decompression, where the changes of the linear reflectivity turned out to be almost fully reversible. The observations on $VO_2$ are highly reproducible and can be explained in terms of a pressure-induced bandwidth-driven insulator-to-metal transition.

$Fe_2O_3$ has been studied via optical pump – near-infrared probe spectroscopy up to pressures of 60 GPa. In the pressure range up to 40 GPa, the changes of the response can be explained by photo-induced absorption and bleaching. The pressure-dependent study of the relaxation dynamics allows to identify cooling of the electron system as origin of the picosecond relaxation process. A sharp anomaly found in the response of $Fe_2O_3$ at 40 GPa indicates a strong rearrangement of the electronic band structure which could be explained by an insulator-to-metal phase transition induced by pumping.

The successful demonstration of pump-probe experiments in diamond anvil cells using pulses from optical to mid-infrared wavelengths and reaching pressures of several tens of GPa is a good basis for further experimental high-pressure studies. Our results obtained on $VO_2$ and $Fe_2O_3$ can serve as a benchmark for the development of advanced material models.

# Kurzfassung

In der vorliegenden Arbeit wird der druckinduzierte Isolator–Metall-Phasenübergang in den Übergangsmetalloxiden $\alpha$-$Fe_2O_3$ (Hämatit) und $VO_2$ mittels ultraschneller Anrege-Abfrage-Spektroskopie (engl. pump-probe spectroscopy) untersucht. Hämatit wird dazu im sichtbaren Spektralbereich angeregt und im nahen Infrarot (NIR) abgefragt, bei $VO_2$ wurde zur Anregung NIR und zur Abfrage mittleres Infrarot (MIR) verwendet. Beide Materialien werden bei hinreichend hohem Druck metallisch, wobei die jeweils dem Isolator–Metall-Phasenübergang zugrundeliegenden Mechanismen verschieden und noch nicht vollständig verstanden sind. Dies motiviert den Einsatz von ultraschneller Anrege-Abfrage-Spektroskopie, die einen Einblick in die Änderung der Bandstruktur und der Ladungsträgerdynamik während des Isolator–Metall-Übergangs gewährt.

Beim Überschreiten eines Schwellenwertes der Anregung wird $VO_2$ photoinduziert metallisch. In unseren NIR-MIR Anrege-Abfrage-Experimenten zeigt sich, dass der Schwellenwert auch bei den höchsten Drücken dieser Messreihe (ca. 20 GPa) nicht verschwindet. Dies weist auf die Existenz lokalisierter Ladungsträger hin und damit verbunden auf das Fortbestehen der Bandlücke. Neben dem Schwellenwert für photoinduzierte Metallisierung wurden auch die Druckabhängigkeiten der Relaxationsdynamik der Ladungsträger sowie des linearen Reflexions- und Transmissionsvermögens untersucht. Eine Anomalie im druckabhängigen Verlauf des Anrege-Schwellenwertes sowie des linearen Reflexions- und Transmissionsvermögens bei einem kritischen Druck von ca. 7 GPa deutet darauf hin, dass durch das Anlegen von Druck Zustände innerhalb der Bandlücke induziert werden. Diese Interpretation wird auch durch während der Dekompression gewonnene Messdaten unterstützt. Die druckinduzierte Änderung des linearen Reflexionsvermögens erwies sich als nahezu vollständig reversibel. Unsere Beobachtungen an $VO_2$ sind reproduzierbar und lassen sich als druckinduzierter, Bandbreiten-getriebener Isolator–Metall-Übergang nachvollziehen.

$Fe_2O_3$ wurde mittels Anrege-Abfrage-Spektroskopie bei Drücken bis zu 60 GPa untersucht. Änderungen im Druckbereich bis 40 GPa können als Wechselspiel eines photoinduzierten Absorptionsbandes und der photoinduzierten Unterdrückung eines anderen Absorptionskanals erklärt werden. Die druckabhängige Untersuchung der Relaxationsdynamik ermöglicht es, der Relaxation auf der Zeitskala weniger Pikosekunden Kühlungsdynamik als Ursache zuzuordnen. Eine scharfe Anomalie im qualitativen Verlauf des Anrege-Abfrage-Signals von $Fe_2O_3$ bei einem Druck von 40 GPa weist auf deutliche Änderungen in der elektronischen Bandstruktur hin, welche als Signatur eines photoinduzierten Isolator–Metall Phasenübergangs interpretiert werden können.

Die erfolgreiche Demonstration von Anrege-Abfrage-Experimenten in Diamantstempeldruckzellen mit Laserimpulsen vom sichtbaren Spektralbereich bis hin zum mittleren Infrarot und bei Drücken von 20 GPa bis zu 60 GPa liefert die solide Basis für weitergehende Hochdruck-Experimente. Die an $VO_2$ und $Fe_2O_3$ erzielten Ergebnisse sind eine gute Grundlage für die Weiterentwicklung der theoretischen Beschreibung solcher Materialsysteme.

# Contents

**Abstract** iii

**Kurzfassung** v

**1 Introduction** 1

**2 Fundamentals I: metal – insulator transitions** 5

2.1 Band insulators, Peierls transition . . . . . . . . . . . . . . . . . . . . 5

2.2 Mott-Hubbard transition . . . . . . . . . . . . . . . . . . . . . . . . . 7

2.3 Anderson insulators . . . . . . . . . . . . . . . . . . . . . . . . . . . 13

**3 Fundamentals II: Experimental techniques** 15

3.1 High-pressure spectroscopy with diamond anvil cells . . . . . . . . . . . 15

3.2 Pump-probe spectroscopy . . . . . . . . . . . . . . . . . . . . . . . . 20

3.3 Adaption for the use with the free electron laser at HZDR . . . . . . . . 27

**4 Pressure-induced band gap filling in $VO_2$ observed by pump-probe spectroscopy** 31

4.1 Introduction and motivation . . . . . . . . . . . . . . . . . . . . . . . 31

4.1.1 Structural phases of $VO_2$ . . . . . . . . . . . . . . . . . . . . . 31

4.1.2 Electronic properties of $VO_2$ . . . . . . . . . . . . . . . . . . . 35

4.1.3 The ultrafast insulator-to-metal transition in $VO_2$ . . . . . . . . 37

4.1.4 Electronic properties of $VO_2$ under pressure . . . . . . . . . . . . 38

4.2 Sample characterization . . . . . . . . . . . . . . . . . . . . . . . . . 40

4.2.1 Sample preparation . . . . . . . . . . . . . . . . . . . . . . . . 40

4.2.2 Raman study under pressure . . . . . . . . . . . . . . . . . . . . 40

4.2.3 Temperature-driven insulator–metal transition . . . . . . . . . . . 40

4.3 Ultrafast pump-probe results . . . . . . . . . . . . . . . . . . . . . . . 42

4.3.1 Data acquisition . . . . . . . . . . . . . . . . . . . . . . . . . . 42

4.3.2 Temperature-dependent pump-probe measurements . . . . . . . 44

4.3.3 Pressure- and fluence-dependent pump-probe measurements . . . 45

4.4 Analysis and interpretation . . . 47
4.4.1 Threshold fluence fitting . . . 47
4.4.2 Pre-edge pump-probe signal . . . 50
4.4.3 Pump-probe signal as a function of pressure . . . 50
4.4.4 Decompression behaviour . . . 52
4.4.5 Estimates of carrier and excitation densities . . . 54
4.4.6 Discussion of the linear reflectivity behaviour . . . 55
4.4.7 Relaxation dynamics . . . 59
4.5 Discussion . . . 60
4.5.1 Band gap filling scenario . . . 60
4.5.2 Comparison of the proposed scenario with prior experimental studies . . . 63
4.6 Summary . . . 67

**5 Ultrafast response of $Fe_2O_3$ under pressure 69**
5.1 Introduction and motivation . . . 69
5.1.1 Structural phases of $Fe_2O_3$ . . . 69
5.1.2 Magnetic and electronic properties of $Fe_2O_3$ under pressure . . . 72
5.2 Experimental details . . . 75
5.3 Pump-probe results . . . 78
5.4 Discussion . . . 81
5.4.1 Origin of the pump-probe response . . . 81
5.4.2 The band structure under pressure . . . 83
5.4.3 Slow relaxation dynamics . . . 87
5.4.4 Transition at 40 GPa . . . 87
5.5 Summary and outlook . . . 90

**6 Summary and conclusions 91**

**Appendix: Additional pump-probe results on diamond and KCl 93**

**Bibliography 95**

**List of abbreviations 113**

**Publications 115**

**Danksagung 119**

**Versicherung 121**

# 1 Introduction

An efficient way to advance the understanding of a material is to characterize it under different conditions, which is often done by varying the temperature or an external magnetic or electric field. Application of pressure allows the tuning of material properties as well. At pressures of several GPa, the volume of solid matter and with it the interatomic distances typically decrease on the scale of percent. As a consequence, pressure not only affects lattice properties like phonons, but also the electronic structure [1]. For example, in GaAs application of 1 GPa (=10 kbar) leads to an increase of the direct band gap from 1.43 eV (at ambient conditions) to 1.54 eV and at a pressure of 4.2 GPa a crossover from the direct to an indirect band gap occurs [2, 3].

There are manifold motivations for the usage of high pressure. Among them is the exploration of phase diagrams including the discovery of new phases and compounds as well as the test of theoretical models. With such information, a better understanding of material properties and their microscopic mechanisms can be gained, which in turn helps to improve models. Moreover, high-pressure experiments help to design new materials. One example is the discovery of $YBa_2Cu_3O_7$, the first superconductor with $T_\mathrm{c}$ above the boiling temperature of liquid nitrogen [4]. After it had been observed that the $T_\mathrm{c}$ of LaBaCuO grows with pressure, the substitution of La with the smaller cation Y was then the successful attempt to replace the effect of external pressure with the introduction of chemical pressure [5–7]. Yet a main driving force for the development of high-pressure technique are geosciences. In order to understand processes in the inner earth like convection or the origin of the earth's magnetic field, it is desirable to know about the state of matter under comparable high pressure and temperature conditions. The production of artificial diamonds under high pressure and temperature [8] was an early milestone for the commercial use of high-pressure technology. A quite recent highlight was the achievement of superconductivity in the sulfur hydride system at temperatures up to 203 K, which could only be stabilized by high pressure around 155 GPa [9]. The sulfur hydride system is also an example for a material that is metallic only under pressure [9].

From a simplistic point of view, application of pressure leads to a broadening of the valence and conduction bands of a material and thus may increase conductivity or even lead to an insulator-to-metal transition [1]. However, experiments on elemental alkali metals have demonstrated that, at sufficiently high compression, interaction with inner electrons can actually induce a metal-to-insulator transition. Sodium, for example, becomes insulating around 200 GPa which corresponds to a reduction of the volume by about 80 %, a factor of 5 [10].

Here we will study insulator-to-metal transitions (IMT) of transition metal oxides. As is typical for materials with partially filled d-shell (or f-shell), they are quite sensitive to pressure [11]. The narrow confinement of the d- and f-shell orbitals leads to strong interaction of electrons in these orbitals; therefore, small changes of external parameters like temperature, doping or pressure will have strong impact on such a correlated electron system [11]. The transition metal ions are surrounded by several oxygen ligands and – besides the overlap of orbitals – pressure can affect the coordination, the crystal field splitting, and the spin state, for example [12]. The materials are highly interesting for technological purposes, and it is desirable to get more insight into the underlying physics.

The materials under study are vanadium dioxide ($VO_2$) and hematite ($Fe_2O_3$), both archetypical strongly correlated electron materials. There are many works on the temperature-induced IMT in $VO_2$, but only a limited number of pressure-dependent studies. In contrast, $Fe_2O_3$ as material of high interest for geoscience has been studied extensively under high pressure – however, there the focus is clearly on the structural transformations. We combine nonlinear pump-probe spectroscopy with high-pressure technique in order to obtain insight into the pressure-induced changes of the electron system.

There are two general concepts for the generation of high pressure: On the one side pressure cells for the application of static pressure [13], on the other side shock-waves for dynamic compression [14]. Each method has its limitations. Thus, by the shock-wave approach higher pressures can be obtained (several TPa instead of several hundred GPa up to 1 TPa), but it allows only experiments at elevated temperatures [15, 16], which for example would not be suitable to study $VO_2$, since there the IMT appears just above room temperature.

As we are interested in the carrier dynamics starting from pressurized, static states, all experimental high-pressure data shown in this work have been obtained using pressure cells, more precisely diamond anvil cells (DAC). The available pressure range depends strongly on the individual construction of a DAC. In addition, the pressure apparatus sets contraints to the experimental methods that can be used for the analysis of matter under pressure. For example, surface sensitive methods like photoemission spectroscopy cannot be applied, since the sample is encapsulated in the pressure cell.

As a word of caution, it has to be mentioned that pressure cannot be applied as cleanly as the other thermodynamic variables like temperature or magnetic field, since always a pressure transmitting medium is needed, which in the best case exerts nearly hydrostatic pressure [4]. However, in comparison to doping, pressure affects a sample much more homogeneously.

Ultrafast time-resolved spectroscopy offers unique possibilities to study non-equilibrium dynamics of elementary excitations. This includes time scales of relaxation or switching to other phases, as well as the coupling to the lattice, for example. Until now, optical or infrared (IR) pump-probe studies under high pressure [17, 18] are rare, and in these studies only pressures of a few GPa have been used. Concerning insulator-to-metal transitions, mid-infrared (MIR) radiation is a perfect probe for free charge carriers due to its low photon energy [19]. However, the small available sample volume in DACs, required in order to be able to obtain high pressures, sets a limit, since the larger the wavelength, the larger is the achievable minimum spot size.

To the best of our knowledge, we demonstrate here for the first time near-infrared (NIR) pump – MIR probe experiments in a DAC. This approach enables us to disentangle different kinds of phase transitions and study the dynamics of insulator-to-metal transitions unavailable in temperature-dependent studies. Our high-pressure experiments not only aim to figure out the nature of the high-pressure state, they also will allow to draw conclusions on the ground state of a material, the state at ambient conditions. Finally, we present optical pump – NIR probe experiments at pressures up to 60 GPa.

In chapter 2 we will give a brief overview about the fundamental physics of metal–insulator transitions, where the focus will be on different mechanisms for Mott transitions. The basics of static pressure generation are explained in chapter 3, which summarizes the experimental techniques used in this study. Besides detailed information on our pressure cell, there also our different set-ups for ultrafast spectroscopy are introduced. In chapter 4, results obtained on the strongly correlated electron system of vanadium dioxide are presented [20]. While this work was done in the pressure range up to about 20 GPa, for the study of $Fe_2O_3$ presented in chapter 5 pressures up to 60 GPa have been applied. The summary of chapter 6 is followed by a short appendix on special experimental aspects and the bibliography.

# 2 Fundamentals I: metal – insulator transitions

Understanding the electronic properties of materials is a central challenge for solid state physics. As fascinating it may be how slight changes of parameters can cause drastic changes of the conductance, as challenging can it be to describe and model such behaviour. In this chapter we will present a rough overview about mechanisms leading to insulating behaviour; more detailed information can be found in literature [12]. For clarity, we separate different effects that can cause a transition between metallic and insulating regimes, however, we have to stress that in real materials some of these can appear in combination.

## 2.1 Band insulators, Peierls transition

In band theory, non-interacting electrons in a periodic lattice potential, as it is present in crystals, can occupy states in allowed energy bands that are separated by forbidden states, giving rise to energy gaps. According to the Pauli principle, each allowed state can be occupied by two electrons with opposite spin. The system tends to minimize its energy and at zero temperature the allowed states are occupied up to the so-called *Fermi energy* $E_{\mathrm{F}}$. Electrons can only be itinerant when the Fermi energy is within an energy band. If the highest occupied energy band is completely filled, a material is insulating.

In this simple view, shifting of bands in energy or tuning of their bandwidth could drive transitions between metallic and insulating behaviour. Changes of the crystal lattice can affect the electronic band structure and cause such transitions. Let us consider a linear chain of atoms with periodicity $a$ as shown in blue in Fig. 2.1(a). The black dots are only a guide for the eye to demonstrate the periodicity. In Fig. 2.1(b) the corresponding electron dispersion relation $E(k)$ is schematically shown. For a half filled band, *i. e.* a Fermi wave vector $k_{\mathrm{F}} = \frac{\pi}{2a}$, the sample system behaves as a metal. Now we assume a periodic lattice distortion (PLD), where the atoms pair along the chain as depicted by the red balls in Fig. 2.1(a). This pairing leads to a doubling of

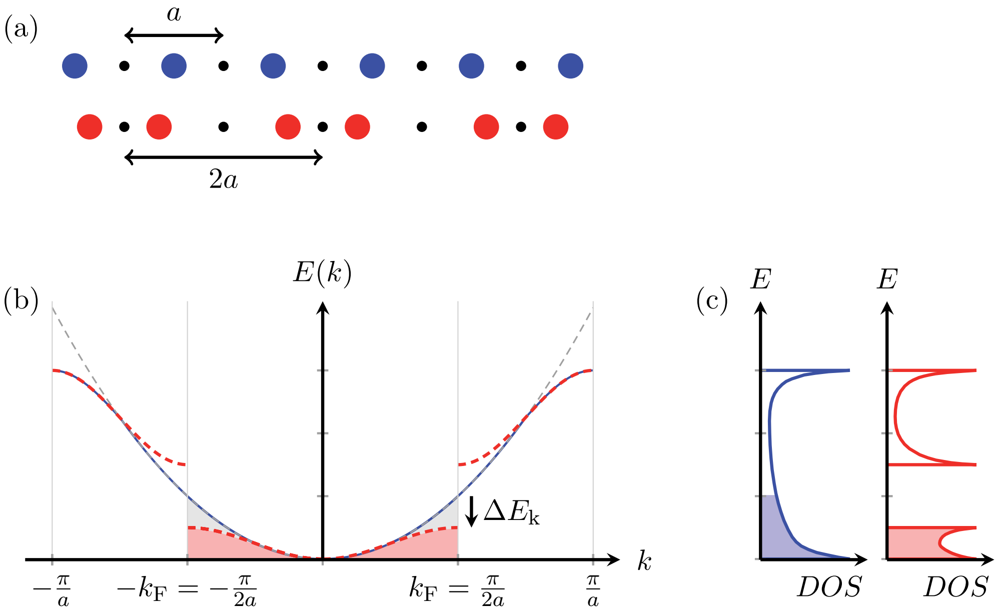

Figure 2.1: Model of a linear chain of atoms. (a) real space lattices for a chain with equidistant atoms (blue) and for a chain with a periodic distortion (red). The black dots are a guide for the eye to demonstrate the periodicities of $a$ and $2a$. (b) Corresponding electron dispersion relations $E(k)$ for the two chains shown in (a). The doubling of the lattice parameter leads to a halving of the Brillouin zone and opening of a band gap (see dashed red curve at $k_\mathrm{F}$). The grey area symbolizes how the energy of the electron system is decreased due to the periodic lattice distortion. (c) Schematic density of states (DOS) on the horizontal axis as function of the energy $E$ for the two one-dimensional electron dispersions of (b). Shaded areas in (c) correspond to occupied states.

the real space lattice constant and consequently to a decrease of the Brillouin zone by 50 % and a changed band structure. In the special case of the originally half filled band, this results in a completely filled valence band as demonstrated in Fig. 2.1(c). While the PLD costs energy, since the potential energy of the atoms increases, the opening of a band gap leads to a decrease of the energy of the electron system. The latter is sketched in Fig. 2.1(b) with the grey and red filled areas. For each wave vector the energy of the electrons is reduced, in our example by $\Delta E_\mathrm{k}$ at $k_\mathrm{F}$; the total energy of the electron system $\int_{-k_\mathrm{F}}^{+k_\mathrm{F}} E(k)\mathrm{d}k$ decreases by the area shaded in grey. It is this decrease of energy of the electron system that enables the PLD [21]. The effect is connected to charge density waves (CDW) [22]. The metal-to-insulator transition accompanied with a PLD is called *Peierls transition* after Rudolf Peierls who discovered the instability of a 1D chain [23]. In reality 1D materials are unstable, however, there exist quasi-1D materials [21]. CDWs also appear in higher-dimension materials, but can have different origin and do not necessarily induce insulating behaviour [21, 22].

Sometimes, materials are expected to be metallic according to band theory, but in reality they behave as insulators. In the next two sections, underlying mechanisms for such behaviour will be discussed.

## 2.2 Mott-Hubbard transition

In so-called *Mott insulators*, electronic correlations cause the opening of an energy gap such that the valence band is completely filled. A first insight into this mechanism can be obtained from the Hubbard model [24], the simplest model to describe interacting electrons on a lattice:

$$\mathcal{H} = - \sum_{\langle ij \rangle, \sigma} t_{ij} c_{i\sigma}^{\dagger} c_{j\sigma} + U \sum_{i} n_{i\uparrow} n_{i\downarrow}, \tag{2.1}$$

with $\langle ij \rangle$ for the sum over pairs of neighbouring sites and with $c_{i\sigma}^{\dagger}$ and $c_{i\sigma}$ as creation and annihilation operators for electrons at site $i$ and with spin $\sigma$. The electron density at site $i$ with spin $\sigma$ can be obtained as $n_{i\sigma} = c_{i\sigma}^{\dagger} c_{i\sigma}$. The matrix element $t_{ij}$ describes the hopping of electrons with spin $\sigma$ between the sites $i$ and $j$; it is proportional to the probability of electron tunnelling between these two sites. While the first term on the right hand side of equation (2.1) describes the gain of kinetic energy of itinerant charge carriers, the second term involves the Coulomb interaction between charge carriers at the same site. In order to bring a second electron to the same site, the on-site Coulomb repulsion energy $U$ has to be invested.

The hopping charge carriers form energy bands with bandwidth $W$ (of non-interacting charge carriers) proportional to the hopping energy $t$ [12]. For $U \gg W$ a band gap $E_{\text{gap}} \approx U - W$ appears. It separates the so-called *lower* (LHB) and *upper* (UHB) *Hubbard bands*. A remarkable difference of the Hubbard subbands in contrast to classical bands is that the distribution of their number of states depends on the occupation of the lower Hubbard band. Removing an electron from the LHB decreases the number of states of the UHB by one and increases the number of free states in the LHB by two [12]. If the number of carriers equals the number of sites, the electrons will be localized and the system is insulating for $U \gg W$, since the LHB is completely filled. In order to be able to move, an electron has to be excited into the UHB. Such an insulating phase is called *Mott insulator*. The same term is also used in a more generalized way for the classification of materials, where it describes a system that can be tuned to

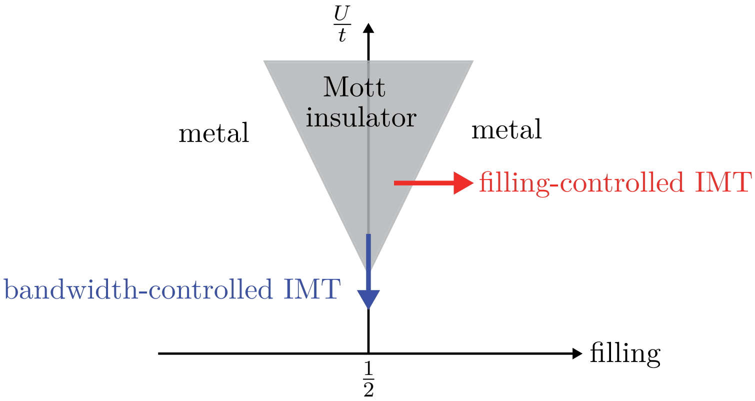

Figure 2.2: Metal–insulator phase diagram based on the Hubbard model. The horizontal axis corresponds to the filling of the Hubbard bands, the vertical axis is the ratio of the intersite Coulomb repulsion $U$ and the hopping energy $t$. Adapted from [26]

an insulating state caused by electronic correlations. The name goes back to Nevill Mott, who together with Rudolph Peierls recognized in 1937 [25] that electrostatic interactions are essential in order to explain the insulating behaviour. A *Mott transition* (also named as *Mott-Hubbard transition*) refers to a transition between a metallic and a Mott insulating phase.

In Fig. 2.2, a schematic metal–insulator phase diagram based on the Hubbard model is shown. The horizontal axis corresponds to the filling of the Hubbard bands. On the vertical axis, the strength of the Coulomb repulsion in units of the hopping energy (proportional to the bandwidth $W$) $U/t$ is plotted; the vertical axis crosses the horizontal axis at half filling, *i. e.* with filled LHB and empty UHB. Only above a critical ratio $U/t$, the system can be in the insulating phase. In order to drive an insulator-to-metal transition, the ratio $U/t$ has to be lowered sufficiently and/or the filling has to be detuned from half-filling. These two ways, marked by the blue and red arrows in Fig. 2.2, are typically referred to as *bandwidth-controlled* IMT and *filling-controlled* IMT [26]. Chemical doping can be used to modify the filling. In order to tune the filling without changing the chemical composition of a material, for example photodoping can be used. With a sufficient number of photoexcited charge carriers, the correlations can be overcome and the system is switched into a metallic phase. The ratio $U/t$ can be tuned by application of pressure. In general, under pressure the overlap of orbitals is improved as their distance is reduced. This leads to an increased hopping probability and therefore an increased bandwidth $W$, while typically the Coulomb repulsion energy $U$ is almost pressure-independent. Thus, such kind of IMT is termed *bandwidth-controlled*.

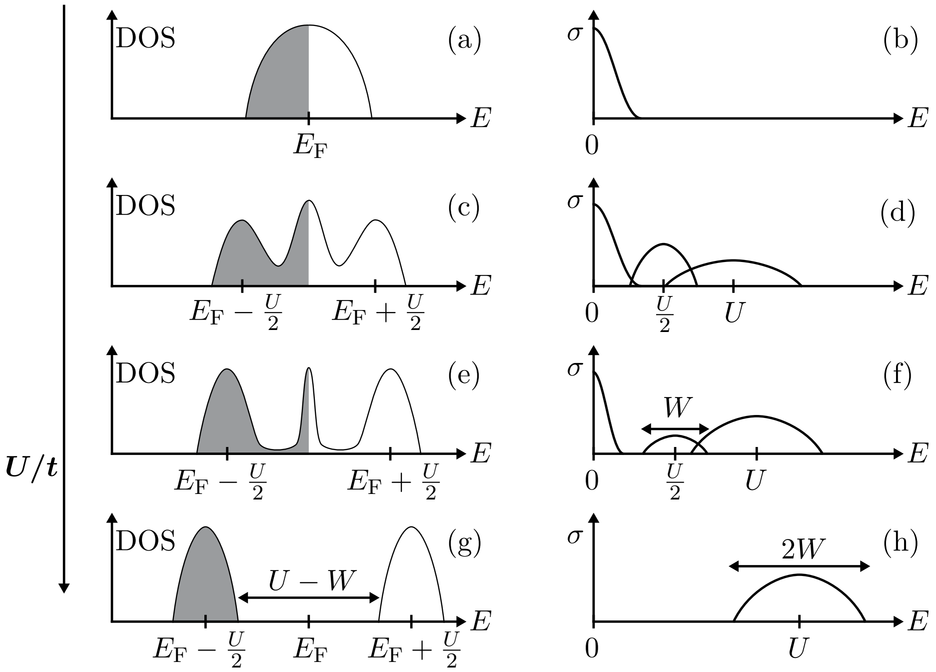

Figure 2.3: (a), (c), (e) and (g) show the evolution of the density of states (DOS) as it is obtained by dynamical mean field theory (DMFT) for the Hubbard model. On the right side the corresponding conductivity spectrum is sketched in the plots (b), (d), (f) and (h). The electronic correlation charaterized by the ratio $U/t$ increases from the plots in the top to the plots in the bottom. Arrows help to estimate energy differences by linking it to the Coulomb repulsion $U$ and the bandwidth of the Hubbard bands $W$. Adapted from [11, 12, 28]

.

Until now we have described the metallic phase and the splitting into two Hubbard bands leading to localization as the two limiting cases of a Mott-Hubbard transition. The treatment of the Hubbard model with dynamical mean field theory (DMFT) reveals that the density of states (DOS) does not just split into two bands during the Mott transition, but it evolves via a three-peak structure [11, 12, 27]. In Fig. 2.3 the DOS and the corresponding optical response are shown from top to bottom for an increasing electron correlation characterized by the ratio $U/t$. In the case of independent electrons, the DOS is concentrated at one band with the Fermi level in the center, see Fig. 2.3(a), where the grey area symbolizes occupied states. This metallic phase is characterized by a strong Drude response as shown in Fig. 2.3(b) where the optical conductivity $\sigma$ is plotted.

When moderate correlations are switched on, spectral weight of the DOS peak centered at the Fermi level is transferred into two satellite peaks that are separated by the Coulomb repulsion energy. The central peak in the DOS is called *quasiparticle peak* (QP) as it accounts for the free charge carriers that give rise to the Drude response, see Figs. 2.3(c) and 2.3(d). The satellites can be understood as Hubbard bands broadened by the QP. Optical transitions from the lower to the upper Hubbard band and from the lower Hubbard band to the QP or from the QP to the upper Hubbard band lead to broad features around $U$ and $U/2$ in the conductivity spectrum. With increasing electronic correlation, the width of the QP reduces for the benefit of the satellite peaks, which are less broadened. Consequently, this spectral weight transfer leads to narrowed peaks in the conductivity spectrum as depicted in Figs. 2.3(e) and 2.3(f). Thus, the width of the peak around $U/2$ will roughly equal the bandwidth $W$ of a satellite peak. While the intensity of the Drude peak and the peak around $U/2$ is weakend with increasing electronic correlation, the peak centered around $U$ will get stronger. Considering the weaker broadening of the peaks, there might occur a small gap in the spectra between the Drude peak and the peak around $U/2$. However, the contrast between gap and band would be low due to the weakened weight of the neighbouring bands. Finally, in case of sufficiently strong electronic correlations the QP disappears and the DOS is split into a completely occupied lower Hubbard band and an empty upper Hubbard band, which is demonstrated in Fig. 2.3(g). The Hubbard bands with bandwidth $W$ are separated by a gap of $E_{\text{gap}} = U - W$. Optical transitions are only possible in the spectral range from $U - W$ up to $U + W$, see Fig. 2.3(h).

The system is insulating only in the situation of Fig. 2.3(g). The three-peaked DOS of 2.3(e) charaterizes a strongly correlated metal. The persistence of the optical band centered around $U$ at the Mott-Hubbard transition is a fundamental difference to the classical IMT which directly switches from the situation depicted in Figs. 2.3(g) and 2.3(h) to that of Figs. 2.3(a) and 2.3(b). The comparison of Figs. 2.3(e) and 2.3(f) with Figs. 2.3(a) and 2.3(b) demonstrates that the Mott-IMT occurs at the onset of the increase of the dc-conductivity. However, a dc-measurement does not allow to determine whether metallization is just the consequence of an improved overlap of two bands or if a three-peaked DOS occurs. With linear spectroscopy it is difficult if not impossible to resolve different contributions to the conductivity spectrum expected from a three-peaked DOS [28, 29]. In the course of this work, we demonstrate that with the help of nonlinear spectroscopy it is possible to identify such a scenario.

For a better understanding, in the plots of Fig. 2.3, the energy scale is always the same. The sketched Mott-transition is mainly driven by the increase of the Coulomb interaction $U$ which grows from the plot at the top to the plot in the bottom. The

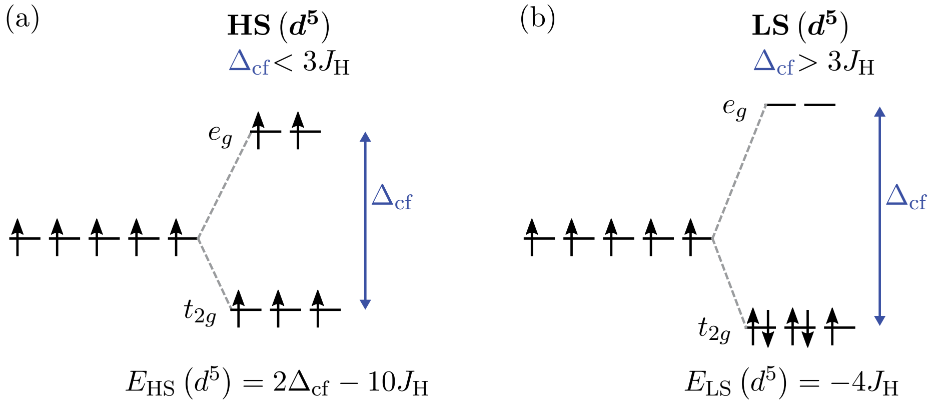

Figure 2.4: Comparison of (a) high-spin (HS) and (b) low-spin (LS) orbital occupation for $d^5$ configuration.

same transition can analogously be achieved by just modifying the hopping $t$ and with this the bandwidth $W$.

Usually, application of pressure is considered to affect electronic correlations by increasing the hopping $t$. Now we will consider a scenario where pressure has strong impact on the effective value of the Coulomb repulsion $U_{\mathrm{eff}}$. It is defined by the energy cost for moving an electron from one ion to another one, which in case of a transition metal compound can be calculated considering the d-shell by

$$U_{\mathrm{eff}} = E_{\mathrm{final}} - E_{\mathrm{initial}} = 2E(d^n) - E(d^{n-1}) - E(d^{n+1}). \tag{2.2}$$

This energy depends for example on the spin state of the transition metal compounds. To illustrate this, we assume the case of a transition metal ion with 5 electrons in the $d$-shell which is surrounded by an octahedral ligand field. The latter causes a crystal field splitting where the three $t_{2g}$ orbitals are lowered in energy and the two $e_g$ orbitals are upshifted. Depending on the strength of the crystal field splitting $\Delta_{\mathrm{cf}}$, which is the energy difference between the $t_{2g}$ and the $e_g$ orbitals, the spin state will be high-spin (HS) or low-spin (LS) as illustrated in Figs. 2.4(a) and 2.4(b). Each pair of spins oriented in parallel reduces the total energy by the Hund's coupling energy $J_{\mathrm{H}}$. In the HS state the electron system of the $d$-shell of one transition metal ion stores the energy $E_{\mathrm{HS}}(d^5) = 2\Delta_{\mathrm{cf}} - 10J_{\mathrm{H}}$, when we set the reference level ($E = 0$) to the $t_{2g}$ levels neglecting any shift of these levels induced by Hund's interaction. With the same basis, the energy of the LS state is $E_{\mathrm{LS}}(d^5) = -4J_{\mathrm{H}}$, where the three spin-up electrons contribute $-3J_{\mathrm{H}}$, and the two spin-down electrons contribute $-1J_{\mathrm{H}}$ (see Fig. 2.4(b)).

From the energy difference $E_{\mathrm{HS}}(d^5) - E_{\mathrm{LS}}(d^5)$ it can be derived that the energy in the HS state is lower than that of the LS state if the crystal field splitting $\Delta_{\mathrm{cf}} < 3J_{\mathrm{H}}$. Since the application of pressure leads to an increased crystal field splitting, it is possible to induce a HS–LS transition by pressure.

Such spin transition can have a dramatic effect on the effective Coulomb interaction. With the same energy scale used in Fig. 2.4 we determine now $U_{\mathrm{eff}}$ according to equation (2.2) with $n = 5$. From the energy difference of the final and initial state we obtain for the initial HS($d^5$) configuration

$$U_{\mathrm{eff}}^{\mathrm{HS}}(d^5) = U - \Delta_{\mathrm{cf}} + 4J_{\mathrm{H}}, \tag{2.3}$$

and for the initial LS($d^5$) configuration

$$U_{\mathrm{eff}}^{\mathrm{LS}}(d^5) = U - J_{\mathrm{H}}. \tag{2.4}$$

In Fig. 2.5(a) the transition of an electron from one HS($d^5$) transition metal ion to a different one is shown. On the right hand side the final state with one HS($d^4$) and one HS($d^6$) ion is sketched. The electron marked in blue has an additional energy of $U$, since it is the second electron in the orbital. In principle it has to be considered to reside in a different band that is upshifted relative to the skteched $t_{2g}$ levels by $U$. Analogous to the HS case of Fig. 2.5(a), in Fig. 2.5(b) the transition of an electron is shown for a material in low-spin configuration.

Comparing equations (2.3) and (2.4) and taking into account the condition for the HS–LS transition ($\Delta_{\mathrm{cf}} = 3J_{\mathrm{H}}$), such a spin transition is accompanied by a drop of the effective Coulomb repulsion $U_{\mathrm{eff}}$ in the order of $2J_{\mathrm{H}}$. This can lead to a so-called *interaction-controlled* IMT, which is another mechanism for a Mott transition that is independent from the filling-controlled or bandwidth-controlled IMT.

It has to be emphasized that the conditions for the spin-transition vary with the filling of the $d$-shell, and that the change of the effective Coulomb repulsion $U_{\mathrm{eff}}$ depends also on the magnetic ordering [12]. In literature much more can be found about Mott systems, for example different classification schemes that help to understand similarities [12]. However, this is beyond the scope of this introduction, where we concentrated on the explanation of the Mott insulating phase and sketched the variety of Mott transition mechanisms.

(a) initial state HS ($d^5$)

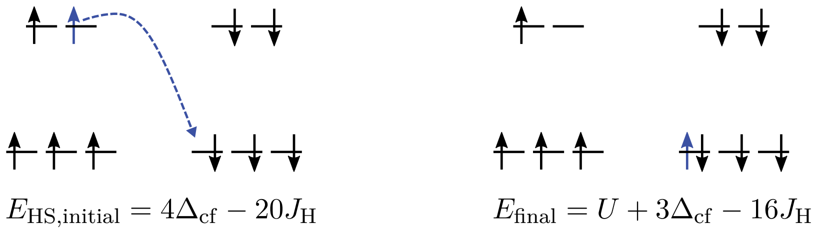

(b) initial state LS ($d^5$)

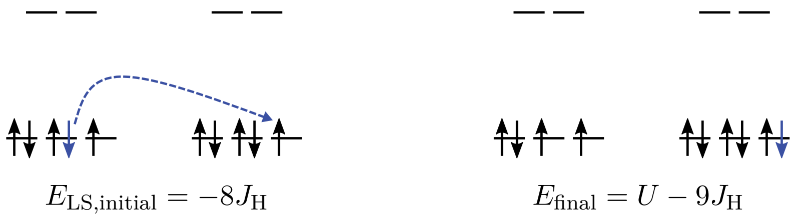

Figure 2.5: Lowest energy *d-d* intersite excitation for (a) a high-spin (HS) and (b) a low-spin (LS) state of a $d^5$ valence shell. On the left hand side the two transition metal ions are shown before the transition, on the right hand side the situation after intersite charge transfer is shown. The energy terms refer to the sum of the electronic energies of the two involved transition metal ions.

## 2.3 Anderson insulators

The formation of insulating phases is not limited to the case of the opening of a band gap. As was shown by Anderson, random lattices can cause the localization of electrons [30]. In the limit of sufficient disorder, the electron wave functions become localized if the DOS is below a certain level [31]. Thus, no metallic conductivity will be possible.

For a better understanding of the mechanism, which is termed *Anderson localization*, we consider to approach the insulating phase starting from the metallic phase of a sample system with periodic lattice potential. In Fig. 2.6(a) an exemplary conduction band for this situation is shown, where the occupied states are hatched. When disorder is switched on and each site has random potential, at energies with sufficiently low DOS, charge carriers become localized on a scale larger than a lattice constant and transport is impossible [12, 31, 32]. Such mobility gaps appear at the band edges or even inside the band at energies where the DOS is too low. This is illustrated by the

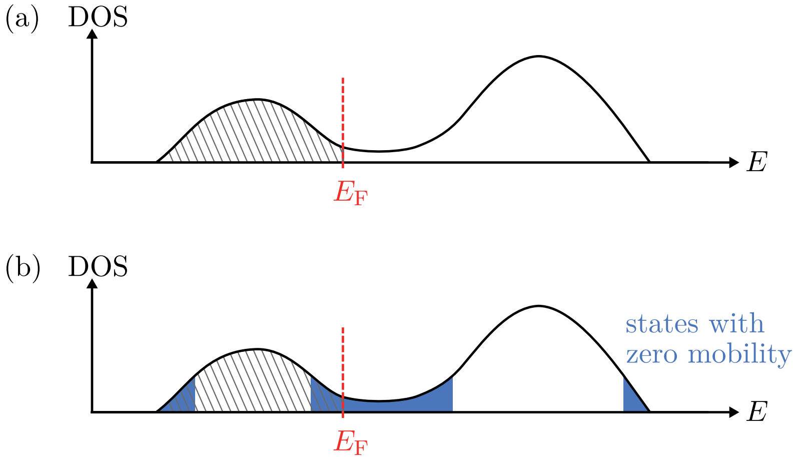

Figure 2.6: Schematic explanation of Anderson insulators. Conduction band (a) before and (b) after introduction of disorder. The hatched region symbolizes occupied states. In (a) the sample is metallic. (b) At energies with sufficiently small density of states (DOS) the mobility of charge carriers vanishes (blue areas). When the Fermi edge (red line) lies within an energy region with zero mobility, the material will be insulating. Adapted from [12].

regions coloured blue in Fig. 2.6(b). With increasing disorder more carriers become localized. When a mobility edge, a boundary between regions with finite mobility and zero mobility, crosses the Fermi energy (red line in Fig. 2.6(b)), an electronic phase transition appears [12]. The system will be insulating when the Fermi energy lies in a region with zero mobility. For example, an IMT can then be induced by changing the number of electrons, such that the Fermi energy is shifted across a mobility edge to a level with sufficiently high DOS.

Since in the scope of this thesis we will study Mott systems, here we refer to literature [31] for further information on Anderson insulators, where also the mixture of different mechanisms that may lead to insulating behaviour is discussed.

# 3 Fundamentals II: Experimental techniques

In this chapter, the main experimental instruments and methods are introduced. The focus is on our specific realizations, while detailed explanations of the general concepts can be found in literature [33–39]. In section 3.1 the high-pressure technique used in our experiments is described. The main measurements presented in this thesis were performed with table-top laser systems which are introduced in section 3.2. The set-up for time-resolved spectroscopy on samples under pressure is fully compatible with MIR pulses provided from the free-electron laser FELBE at HZDR. In section 3.3, the adaption to the large scale facility is demonstrated with exemplary measurements on GaAs. Besides the time-resolved measurements, standard Raman spectroscopy was used to characterize pressure-induced structural changes.

## 3.1 High-pressure spectroscopy with diamond anvil cells

Diamond anvil cells (DAC) are the work horse for spectroscopy on pressurized samples. They use the concept of concentrating a force on a small area in order to achieve high pressures. A typical unit of high pressure is 1 GPa = 10 kbar, which is ten thousand times the atmospheric pressure. For comparison, around 410 km beneath the sea level the pressure is about 14 GPa and the maximum pressure in the core of the earth is around 365 GPa [37, 38].

Diamond as material of the anvils is perfect for high-pressure applications as it is the hardest known material. In addition, its broad transmission spectrum makes diamond interesting for spectroscopic set-ups, as it allows spectroscopic access through the anvils to a sample mounted in a DAC. In our case we used so-called type IIa diamonds. With less than 1 ppm nitrogen and no other notable dopants, they offer minimum absorption and high transmission from ultraviolet (UV) to far-infrared. However, between 2.6 µm and 6.2 µm [40] there is a weak absorption band due to multi-phonon absorption. The indirect band gap of 5.47 eV leads to an inter-band absorption edge around the wavelength of 230 nm [40, 41].

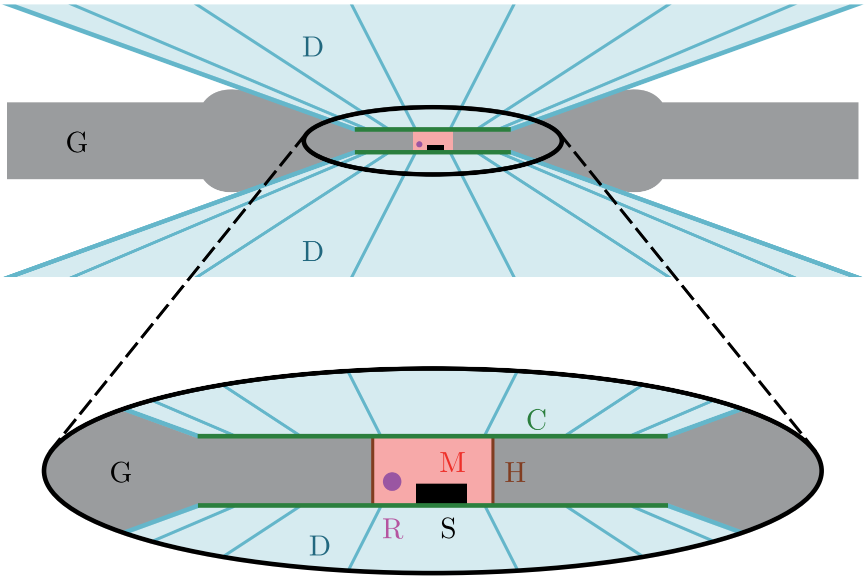

Figure 3.1: Schematic cross-sectional view of a diamond anvil cell: Diamond anvils D (light blue) with sample S (black) in contact with the culet plane C (green) of one diamond; preindented gasket G (grey) with gasket hole H (brown) which is filled with pressure transmitting medium M (light red) surrounding sample S and ruby crystal R (purple) which serves as pressure sensor.

Figure 3.1 shows the central part of a standard diamond anvil cell. There are two opposing diamond anvils (D in Fig. 3.1) that are pushed together thus exerting pressure to a pressure transmitting medium and the sample (M and S in Fig. 3.1) situated between the flat tips of the diamonds, the so-called *culets* (C in Fig. 3.1). The smaller the culets, the higher the maximum available pressure. In order not to put uniaxial, but isotropic pressure to the sample, it is mounted in the hole of a preindented gasket (G and H in Fig. 3.1) and surrounded by a suitable pressure transmitting medium (M in Fig. 3.1). Depending on the selected method of pressure determination, a pressure sensor (R in Fig. 3.1) has to be added in the gasket hole when filling the DAC.

For our measurements, two different types of DAC have been used: A commercial plate DAC from *Almax-easylab* and a BX90 piston-cylinder cell (for ultra high pressures) [13] provided from our cooperation partner at the *Bayerisches Geoinstitut*, Bayreuth. In both cells, pressure is applied by tightening some screws. The main difference is that in our DAC the distance of the diamond anvils is changed by bending two plates, while in the BX90 this happens by pressing a piston into a cylinder. The used BX90 had a culet diameter of 250 µm and allowed to reach pressures up to about 65 GPa, the

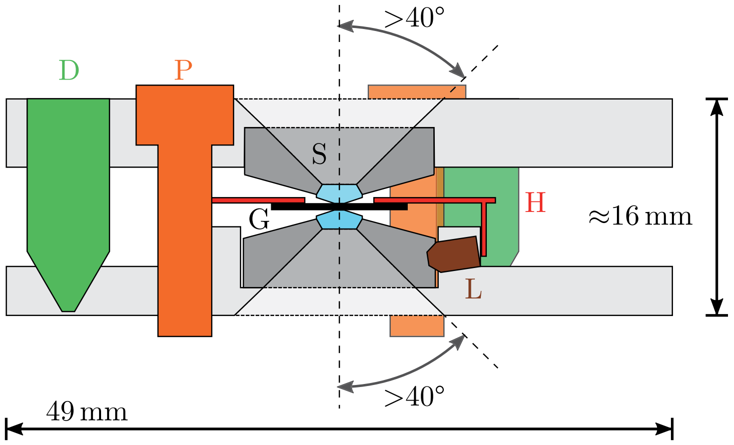

Figure 3.2: Schematic section view of our Almax plate DAC (*Almax-Easylab*). The central dashed line marks the 3-fold symmetry axis. Diamond anvil (blue) mounted to a seat S (dark grey); three set screws D (green) for alignment of the plate (light grey) distance and three set screws L (brown) for lateral positioning of the lower seat; three pressure screws P (orange); gasket holder H (red) with gasket G (black).

maximum pressure of our plate DAC with a culet diameter of 450 µm is around 25 GPa. While for the latter steel gaskets have been used, the BX90 was operated with rhenium gaskets in order to achieve ultra high pressures. Both cells use Boehler diamonds [42], *i. e.* diamonds that are mounted in seats via their side plane, which for this purpose has a conical shape. In comparison to the classical design, this brings the advantage of a much higher field of view. The opening angles are beyond 80°, making such set-ups attractive for X-ray measurements and spectroscopy.

For further details on the BX90 we refer to literature [13] and concentrate now on our plate DAC as schematically shown in Fig. 3.2. Each diamond is mounted in a seat (S in Fig. 3.2) located in the center of a circular plate of about 5 cm diameter and several millimeters thickness. The seats for the anvils are made from tungsten carbide which among others brings the advantage of a high mechanical stability. A couple of set screws (D and L in Fig. 3.2) allow to align the culets in parallel and for perfect lateral overlap. By simultaneous tightening of all three pressure screws (P in Fig. 3.2), it is guaranteed that the alignment of the DAC is not lost during the pressure cycle. The alignment can be tested by closing the empty cell (without gasket) and monitoring the interference pattern between the culets.

The gasket is mounted on a gasket holder (G and H in Fig. 3.2) which can be clamped on the seat of the diamond at the lower plate. We used stainless steel disks of 250 µm thickness for the production of gaskets. After preindentation down to a thickness of 50 µm, holes of about 180 µm have been drilled using a spark eroder. These dimensions of the sample chamber demonstrate that only tiny samples can be studied under high pressures in the DAC. When pressure is applied, the metal of the gasket tends to flow aside of the pressurized area leading to an increase of the gasket hole diameter. If the hole reaches the edge of the culets this would result in an uncontrolled pressure release, typically destroying the load as well as the two anvils. Thus, the gasket flow has to be controlled and careful preparation of the DAC is crucial. In fact, the alignment of the DAC and the preparation of the gasket have strong influence on the maximum pressure that can be reached [43].

Another important point is the selection of an appropriate pressure transmitting medium. In the ideal case, the goal is to keep hydrostatic pressure conditions [44]. However, in reality at a certain pressure the medium solidifies, and differential and shear stresses appear [44]. This is an inevitable issue for high-pressure experiments. From that follows the strategy to approximate the goal by choosing a pressure transmitting medium which has minimal non-hydrostaticity. This is called *quasi-hydrostatic* conditions.

For the majority of our experiments it was necessary to measure the directed reflection from the sample surface. In this situation the sample has to be fixed in the gasket hole. This can be ensured by the use of a solid pressure transmitting medium, in our case finely ground powder of CsI or KCl. In order to avoid interference effects in spectroscopic experiments, the sample was mounted with a large contact area to one of the diamonds. This can be achieved by adding the sample either in the first or in the last step of the filling process.

With respect to minimizing pressure anisotropy, the best pressure transmitting media are noble gases. Even after solidification they show a high degree of hydrostaticity due to very weak van-der-Waals bonding. For the experiments with the highest pressures, *i. e.* with the BX90 pressure cell, such a filling was provided by our cooperation partner at the Bayerisches Geoinstitut. They have a special apparatus allowing to close the DAC in a high-pressure neon atmosphere. In comparison to filling the cell with liquefied gases this method has the advantage to reduce the risk of flushing samples out of the DAC. With a starting pressure beyond 4.8 GPa (solidification pressure of neon at room temperature) the sample position could be fixed.

In contrast to the aforementioned reflection measurements, for Raman measurements no direct contact between sample and diamond is needed, as in the measurement spontaneous emission into all directions is captured. This allowed to use a mixture of methanol:ethanol as pressure medium, with the advantage of lower pressure anisotropy

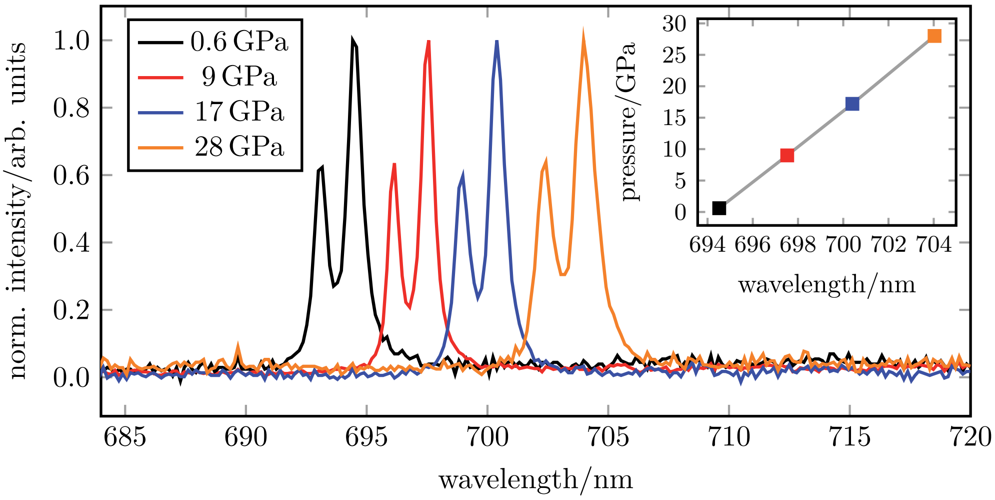

Figure 3.3: Ruby fluorescence spectra captured with the QE65000 spectrometer at different pressures. In the inset, the pressure determined according to [45] is shown as function of the fitted $R_1$ emission line positions.

compared to CsI or KCl. There is another important aspect for the selection of the pressure transmitting medium. It should not affect the spectroscopic measurement, *i. e.* should have high transmission and no absorption in the relevant spectral range.

The pressure in the DAC was determined via the pressure-dependent shift of the ruby fluorescence R-lines which is roughly 1 nm per 3 GPa [45]. We used small ruby crystals of around 10–20 µm diameter as pressure-sensor and excited them by means of a diode pumped solid state laser at 532 nm or with a laser diode at 445 nm. The latter is essential above 30 GPa, as the absorption bands of ruby get short-wave under pressure. The fluorescence spectra have been captured with a QE65000 spectrometer (*Ocean Optics*) with a resolution of about 0.16 nm, see Fig. 3.3. The device was cooled via a Peltier module for improved signal-to-noise ratio and calibrated with a neon calibration lamp (Pen-Ray line source from *LOT-QuantumDesign*). Lorentz-Gauss fits were used to determine the position of the $R_1$ emission line of ruby. From that the pressure was calculated according to Mao *et al.* [45]. The statistical error of the pressure determination is lower than 0.2 GPa. However, there are sources for systematic errors. Heating of the ruby pressure sensor slightly red-shifts the R-lines. For that reason only a few mW of laser power were sent into the DAC for the pressure determination. Pressure inhomogeneity originating from the imperfection of the pressure transmitting medium in the gasket hole is the most relevant systematic error. Tests with several ruby chips at different positions showed that in case of CsI as pressure transmitting medium this uncertainty can be about 1 GPa at a maximum pressure of 10 GPa and up to 25 % at pressures in the order of 20 GPa. For analysis the pressure at the sample was always estimated via the ruby sensor with maximum pressure.

The accuracy of the pressure measurement was also tested by comparison with Raman measurements of the diamond anvils. In a DAC under pressure, the stress in the anvils increases from their base to their culet, leading to a Raman signal with a sharp edge at high frequencies [46, 47]. From the position of this edge, the maximum pressure can be estimated. The difference between the pressure thus determined and that obtained by ruby fluorescence was in the order of one percent.

## 3.2 Pump-probe spectroscopy

The application of pressure (using DACs) allows for tuning of the bandwidth $W$ of a strongly correlated electron system. Moreover, long-time measurements become possible, since the pressure in the cell is quite stable. However, the pressure equipment sets constraints for applicable measurement techniques. For example, surface sensitive methods like photoemission experiments are not compatible with DACs. Standard techniques to study the electronic structure of samples under pressure are linear spectroscopy, X-ray absorption spectroscopy or conductance measurements. Since we are interested in ultrafast dynamics, we need a method sensitive on time scales faster than that of electronic devices. This is possible via pump-probe spectroscopy.

Pump-probe spectroscopy is a common method for the study of ultrafast relaxation dynamics. First, the sample is photoexcited by a strong pump laser pulse and after an adjustable delay time it is probed with a weak laser pulse for pump-induced changes. This measurement is repeated for a series of different delay times thus giving insight into the temporal evolution of the system. In order to have independent results for each pump cycle, the time interval between two pump pulses has to be much larger than the observed relaxation time scales. Averaging the measured signal over several pump-probe cycles for each delay time increases the signal-to-noise ratio and makes possible a time resolution that depends only on the duration of the pump and probe pulses, but is not limited by the electronic measurement devices. The pump-induced change of the probe intensity after reflection from or transmission through the photoexcited sample is termed *pump-probe signal.* Figure 3.4 schematically shows a pump-probe measurement in a DAC.

There are a number of challenges when implementing pump-probe measurements in a DAC. The limited space available for the sample makes it necessary to focus tightly on a very small area in the cell. This in turn increases the need for high mechanical stability and alignment strategies with high reproducibility of the DAC positioning. Neglecting

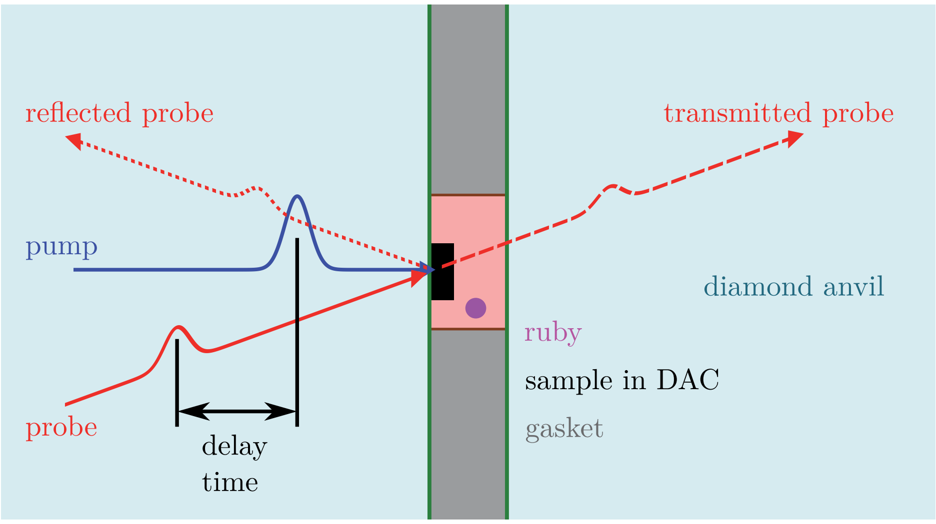

Figure 3.4: Schematic view of a pump-probe experiment in a diamond anvil cell (DAC). The sketches of the laser pulses are intensity profiles. At a variable delay time after pumping (blue), the photoexcited sample (black) is probed (red) for pump-induced changes in reflection (red dotted) and transmission (red dashed).

possible reflections at side facets of the diamonds, there are still several interfaces in the stack (at boundaries between diamond, sample, pressure transmitting medium, diamond) of a DAC that could cause reflections. Therefore it has to be considered at the alignment of the set-up and data interpretation, whether a measurement is affected by back-reflection from such an interface. This holds especially for reflection from the culet plane (green in Fig. 3.4) of the rear diamond and the backside of the sample as they are approximately in the focal plane. We will come back to such points at the analysis of our measurements. In general, it is helpful to focus the probe tighter than the pump beam, since thus a region of a more homogeneous excitation is probed. For the small sample area available in a DAC this means on the one hand to focus the probe as tight as possible. On the other hand, the size of the pump spot has to be small enough to achieve a sufficient pump fluence on the sample, and in order to avoid artifacts, it should be smaller than the sample area.

Our set-up is built in a modular way, offering high flexibilty for two-colour pump-probe experiments, where the pump and probe photon energies differ. The two-colour approach brings technical advantages like the absence of interference between pump and probe pulses and a simplifed filtering of the probe signal from a linear pump background. Hence, the main point of the two-colour pump-probe concept is to have different interaction mechanisms of pump and probe with the sample. For example, a low probe photon energy (not allowing inter-band transitions) is suitable for the detection of pump-induced free charge carriers.

Experiments have been performed with the set-up in configuration for near infrared pump – mid-infrared probe experiments, as shown in Fig. 3.5. The table-top set-up is based on a commercial laser system (*Coherent*). It uses a femtosecond Ti:Sa oscillator (*Coherent* Micra) providing pulses of several nJ at a repetition frequency of 78 MHz. By means of chirped pulse amplification with a regenerative amplifier (*Coherent* RegA) the pulse energy is increased by more than three orders of magnitude while the repetition rate is lowered to 250 kHz. The compressor of the amplifier can be used to chirp its output in order to compensate for the dispersion of optical elements in the set-up, and thus to set the shortest pulse duration at the sample. A portion of the RegA output is always sent to an autocorrelator giving information on the pulse duration. Due to gain narrowing at amplification and spectral clipping in the stretcher and compressor, the pulses have a minimum intensity autocorrelation width of 50-60 fs. After the amplifier, a 4-axis beam stabilization kit (*TEM* $\mu$Aligna) with two motorized mirrors in a distance of roughly 1 m has been installed. It ensures that the laser radiation is always on exactly the same optical path compensating slow drifts in pointing and position that might appear *e. g.* through temperature changes or spectral tuning of the laser system.

The stabilized output of the RegA is split into two beams as shown in Fig. 3.5. One half is used for the pump branch, the other half for the generation of probe pulses via nonlinear frequency conversion by means of a commercial collinear optical parametric amplifier (OPA) and a difference frequency generator (both *Coherent*). The amplified pulses are appropriate to drive a cascade of nonlinear processes. First, in the OPA, with a small part of the incident power a white spectrum is generated via self phase modulation in a sapphire crystal. A selected part (signal) of this broad spectrum is amplified via optical parametric amplification with a beta-barium borate (BBO) crystal. Because of energy conservation, at the same time idler photons are generated at the expense of the fundamental IR light,

$$\hbar\omega_{\mathrm{IR}} = \hbar\omega_{\mathrm{signal}} + \hbar\omega_{\mathrm{idler}}. \tag{3.1}$$

The signal and idler spectrum can be tuned by rotation of the BBO, as this changes the frequency where phase matching is fulfilled. In the next step, the probe frequency is produced by difference frequency generation (DFG) of signal and idler in a $AgGaS_2$ crystal. This again is a three-wave mixing process. Due to energy conservation we have

$$\hbar\omega_{\mathrm{DFG}} = \hbar\omega_{\mathrm{probe}} = \hbar\omega_{\mathrm{signal}} - \hbar\omega_{\mathrm{idler}}. \tag{3.2}$$

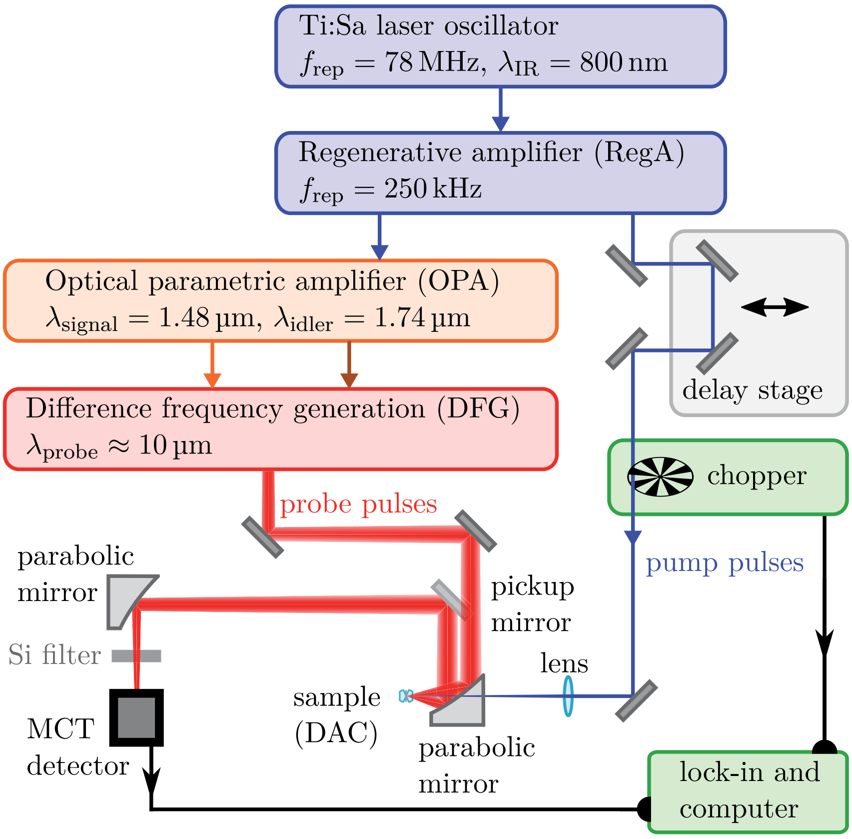

Figure 3.5: Schematic table-top set-up for near-infrared pump – mid-infrared probe experiments in reflection geometry.

In order to obtain a specific desired probe (central) wavelength $\lambda_{\text{probe}}$, the OPA and DFG first have to be prealigned with the help of some apertures to obtain a DFG signal at $4\,\mu\text{m}$. Then, OPA and DFG are tuned and optimized in stages. As there was no spectrometer available for the MIR, we estimated the probe central wavelength by the measured maximum of the signal spectrum. Combining equations (3.1) and (3.2) gives

$$\hbar\omega_{\text{probe}} = 2\hbar\omega_{\text{signal}} - \hbar\omega_{\text{IR}} \quad \Longleftrightarrow \tag{3.3}$$

$$\lambda_{\text{signal}} = 2\frac{\lambda_{\text{IR}}\lambda_{\text{probe}}}{\lambda_{\text{IR}} + \lambda_{\text{probe}}}. \tag{3.4}$$

From this follows that for an intended probe wavelength of $\lambda_{\text{probe}} = 10\,\mu\text{m}$ a signal spectrum centered at $\lambda_{\text{signal}} = 1.48\,\mu\text{m}$ is needed, as the Ti:Sa pulses have a central wavelength of $\lambda_{\text{IR}} = 800\,\text{nm}$. The correspondig idler wavelength is $\lambda_{\text{idler}} = 1.74\,\mu\text{m}$.

For higher conversion efficiency, OPA and DFG have a two-pass geometry. With incident 50 % (0.75 W) of the RegA output power it is possible to generate 1.5 mW probe power at a wavelength of $\lambda = 10\,\mu\text{m}$ and repetition rate of 250 kHz. In principle, the table-top set-up would allow to generate probe pulses centered at a probe wavelength from 1 µm (no DFG needed) up to 12 µm.

Due to the small sample dimensions, it is crucial to be able to tightly focus the long-wave probe pulses onto the sample. For this purpose, a focusing element with short focal length and a large probe mode diameter at the location of this focusing element are beneficial. The latter was achieved by a slight decollimation of the probe beam after the DFG crystal. The beam was then focused using a parabolic mirror with only 2″ focal length and 2″ diameter. Under observation with a PyroCam, the decollimation was aligned for a proper beam diameter and Gaussian beam profile. The spot diameter in focus was determined by the knife edge method. For a Gaussian beam profile with cylindric symmetry the $1/e^2$ intensity width matches the difference between the position where 16 % and the position where 84 % are blocked by the linear edge. Here we used a gold edge evaporated onto a GaAs wafer and moved it with an *xyz*-stage into the beam path. The width was determined in two directions orthogonal to the beam path. The 16 % and 84 % values were calculated according to the difference of the reflected intensity at the gold side and the GaAs side. At a probe wavelength of 10 µm a diameter (FWHM) of 40 µm was achieved in the focus.

The parabolic mirror was also used to collect the reflected probe, see Fig. 3.5. Incident and outgoing probe beam do not overlap so that the latter can easily be picked up and focused on a mercury cadmium telluride (MCT) detector. Overall, the completely reflective optics for the MIR-probe has the advantage of minimum losses and dispersion.

The other part of the amplified Ti:Sa pulses, serving as pump, is focused by a lens and sent through a hole in the parabolic mirror onto the sample. A *Thorlabs* CMOS camera with 3.6 µm pixel size (square) has been used to determine the spot size in the focal plane. Any pump light scattered into the probe path is filtered by means of a Si-filter in front of the MCT detector. The pump-probe signal is measured with a lock-in amplifier (*Stanford* SR830 or *Signal Recovery* 7265) taking the modulation frequency of a chopper wheel in the pump beam as reference. In addition, the total intensity of the probe is measured. The pump-probe signal can then be referenced to the linear signal (signal for blocked pump beam and chopped probe) giving the relative change of reflection and transmission. In addition, a variable filter in the pump path allows to measure the fluence-dependence of the pump-probe signal.

A 400 mm motorized delay stage (*Newport*) in the pump branch allows to tune the relative delay time between pump and probe. When aligned accurately, it enables a scan range of 2.5 ns without any changes in the pointing of the beam. Only the spot

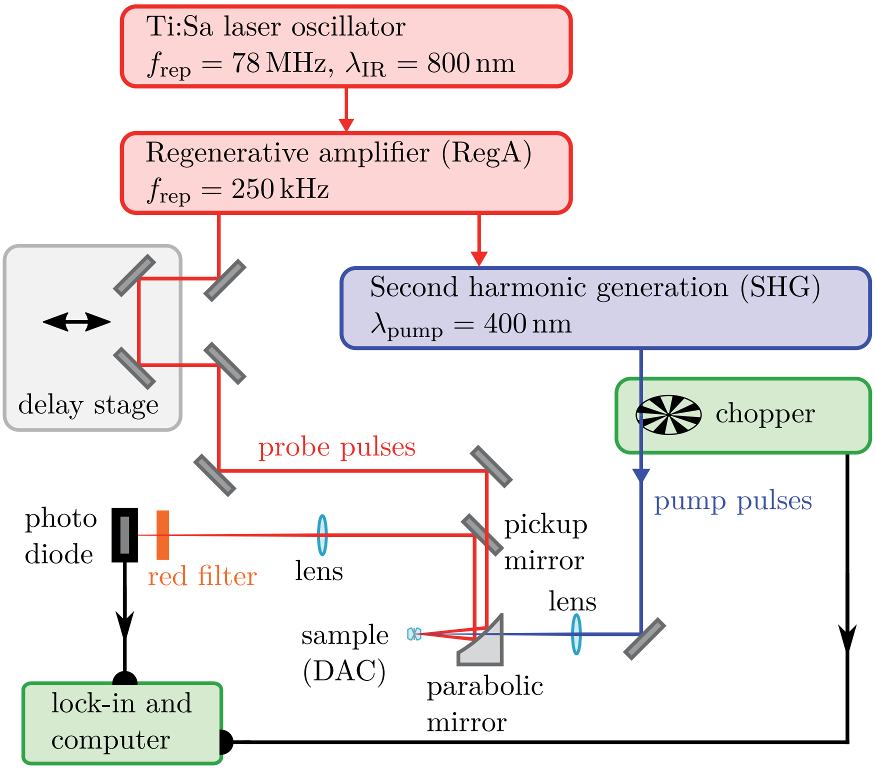

Figure 3.6: Schematic optical pump – NIR probe set-up in reflection geometry

size varies slightly because of finite divergence. The minimum step size of the delay stage is 2.5 µm, which corresponds to a time step of less than 20 fs. Thus, it is the pulse duration that limits the temporal resolution of pump-probe scans.

Besides the NIR pump – MIR probe set-up described above, also a set-up with optical pump – NIR probe configuration as shown in Fig. 3.6 has been assembled. The main differences are that now the amplified Ti:Sa pulses serve as source of the probe, *i. e.* filters are needed to make the probe weaker than the pump, and that the photon energy of the pump is doubled via second harmonic generation (SHG). This frequency doubling is obtained using a BBO crystal. The SHG module assembled in the course of this work is mainly constructed with reflective optics. Residual fundamental NIR light is filtered away in two stages. The overall SHG conversion efficiency is above 25 %. In order to keep the optical path short, the delay stage is again inserted in the branch without nonlinear frequency modification, which is the probe branch in this case. Moreover, a lens optimized for 400 nm light was installed in front of the parabolic mirror. The probe reflected from the sample and recollected by the parabolic mirror was focused by a lens on a Si photodiode, where any scattered pump light contributions are removed with a low-pass filter.

Both set-ups (Fig. 3.5 and 3.6) can be easily adapted or extended for transmission measurements. In such case, the transmitted probe has to be collimated behind the DAC, separated from remaining pump light and focused to a second detector.

For optimum signal quality, it is essential that pump and probe are focused to the same spot on the sample. Another issue is that the DAC has to be removed from the set-up for each tuning of the pressure. The needed accuracy and high reproducibility can be achieved with the help of two alignment lasers of the same colour that are focused by the parabolic mirror and cross precisely at the position of the probe focus. One of these alignment lasers was collinear to the probe beam path, so that it also serves as a guide for the eye. This is useful in particular for the MIR pulses of the DFG set-up, as they are too weak to be detected with viewer cards. The second alignment laser is first aligned parallel to the probe beam and later (if necessary) slightly adapted such that the two beams cross at the probe focal spot. In a next step, the focus of the pump is aligned to this crossing point. This can easily be done with the aforementioned CMOS camera. In case of the MIR probe, the knife edge method is used to mark the probe focal plane. The coincidence of the alignment laser crossing point with the probe focus is then evaluated by observing scattered light of the alignment laser spots on the gold side with a video microscope. It should be emphasized that only the crossing point of the alignment lasers is proper for this. Spectral aberrations hinder the reliable determination of the common focal position by observation of a crossing point of the pump and probe beams. The described strategy enabled reproducible positioning of the DAC with a focal accuracy better than 30 µm. This is an order of magnitude smaller than the Rayleigh length even for the very tightly focused MIR pulses. Therefore the minimum beam diameter is always a good approximation for the spot size on the sample.

The pump fluence was estimated assuming that the full power is homogenously incident on a circular area with the FWHM diameter. Thus, in the center the fluence is underestimated, and at the edge overestimated. In the relevant spectral range, the refractive index of diamond is around 2.4 and pressure-induced changes are smaller than 0.02 for pressures below 40 GPa [48]. Thus, the refractive index of diamond is typically between the refractive index of the sample under study and that of the surrounding air. Therefore, in comparison to reference samples outside a DAC, a higher part of the pump fluence will enter a sample mounted in the DAC. Since there are not always data available for the change of refractive indexes under pressure, in the following all pump fluence values refer to the intensity measured outside the DAC.

The small spot size in the focus make the pump-probe experiments sensitive to spatial drifts. In order to stabilize the spatial overlap, the PID parameters of the cooling system for the Ti:Sa system have been optimized, as well as the air flow of the air conditioning system. In the actual set-up, this was essential in order to overcome modulations on a time scale of a few minutes in the pointing of the laser beams. Despite the installation of a beam stabilization kit, slight drifts of the spots still can appear. A possible reason could be small relaxation effects at mirror holders defining the beam path after the stabilization kit, as they all work with tension springs. This observation also demonstrates that is beneficial to minimize the total optical path. For measurement series extending over longer times it is advisable to readjust the pointing of the pump in regular intervals in order to ensure perfect spatial overlap with the probe.

## 3.3 Adaption for the use with the free electron laser at HZDR

As mentioned above, the developed set-up is compatible with the free electron laser (FEL) FELBE at HZDR. The FEL runs at 13 MHz and can be tuned from 4 up to 250 µm. In comparison to the DFG it offers lower photon energies at much higher pulse energies (at least 2 orders of magnitude), while the spectrum is much narrower and thus the pulse duration defining the temporal resolution of the large scale facility FELBE is not in the order of several ten femtoseconds, but on the level of a picosecond.

Proof of principle NIR pump – MIR probe measurements on GaAs have been performed with the FEL providing MIR probe pulses. The corresponding set-up is sketched in Fig. 3.7. There are more changes than replacing the OPA and DFG modules (Fig. 3.5) with the FEL. Essential for the ultimate time resolution of the two-colour pump-probe experiments is that the sources of pump and probe pulses are synchronized and have a minimum relative timing jitter. The active stabilization is achieved by a piezo-controlled detuning of the cavity length of the Ti:Sa laser oscillator such that our table-top laser runs at the same frequency as the master oscillator (see Fig. 3.7) that feeds the FEL with electron bunches. Remarkably, despite the fact that the different systems are separated by several tens of meters, the timing jitter between Ti:Sa and FEL signals is below one picosecond.

In order to find temporal overlap, pump and probe have been captured with a fast detector connected to a sampling scope (bandwidth 20 GHz corresponding to 50 ps temporal resolution). Then the relative phase of the Ti:Sa oscillator was properly adjusted by short-term cavity detuning and fine aligned by tuning the propagation duration (cable length) of the synchronization signal. Finally, it is necessary to do a pump-probe measurement and scan the delay stage in order to find temporal overlap of pump and probe.

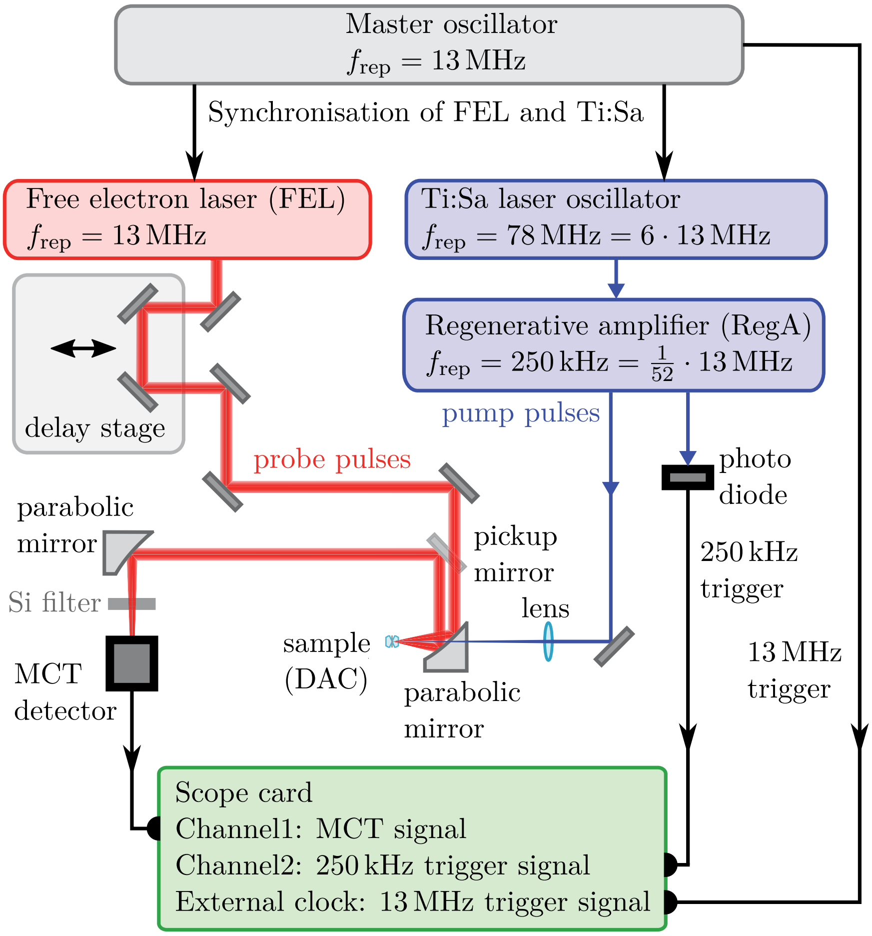

Figure 3.7: Schematic near-infrared pump – mid-infrared probe set-up applying a table-top Ti:Sa laser system in the pump branch which is synchronized to the free electron laser FELBE that delivers MIR probe pulses.

Another change in comparison to the experiment with the OPA and DFG modules is the use of a time-domain filtering technique in order to extract the pump-probe signal. The boxcar method implemented in cooperation with Markus Hähnel allows to directly calculate the pump-induced change as difference of the amplitude of a pump-affected probe pulse and of a probe pulse that arrives at the sample after its relaxation, see Fig. 3.8.

For the same measurement duration, this time-domain filtering technique delivers much better signal-to-noise performance than lock-in measurements (see Fig. 3.9), where due to the mismatch of the repetition rates of pump (250 kHz) and probe (13 MHz) the pump-probe signal is significantly weakened since the pump-induced amplitude is averaged over 26 probe pulses.

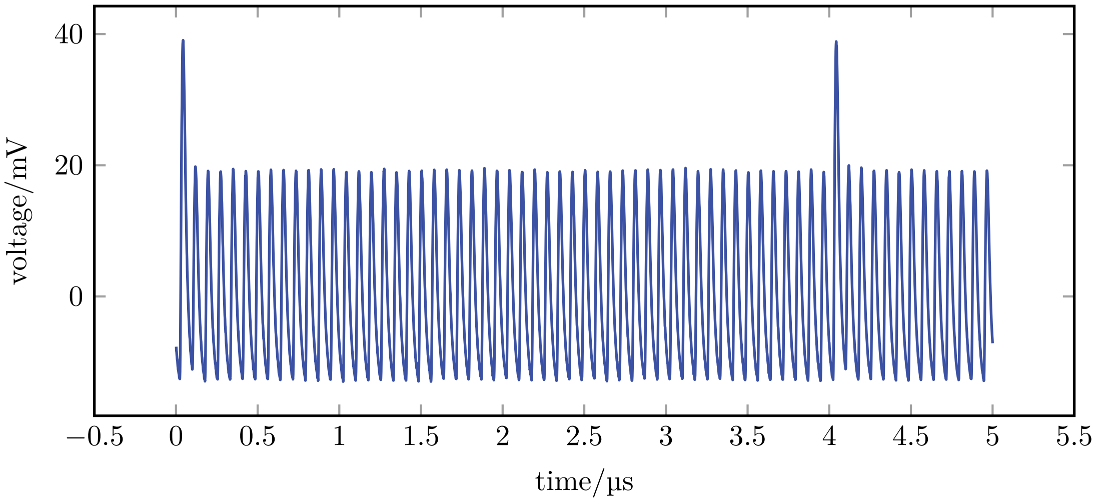

Figure 3.8: Exemplary signal of the MCT detector in Fig. 3.7 captured with a sampling scope in AC-coupling. Every 4 µs, a pump pulse arrives at the GaAs sample leading to the elevated reflection of a probe pulse. Between two pump pulses, 51 probe pulses are detected.

The test measurements on GaAs samples shown in Fig. 3.9 are obtained under special test conditions using a probe wavelength of $\lambda_{\mathrm{probe}} = 30\,\mu\mathrm{m}$ and an IR-microscope (*Bruker* IRscope II) equipped with a Schwarzschild objective. The measurements on a GaAs reference sample and a GaAs sample mounted inside the DAC show an initial increase of reflectivity and after some time a negative signal. This corresponds to the transition of the plasma frequency from above to below the probe frequency. The remarkable difference in the minimum normalized signal amplitude is due to the different refractive indices of air and diamond.

The test measurements were done using a scope card by *GaGe* with a maximum internal bandwidth of 50 MHz for data acquisition. The device was triggered at the pump frequency. In principle, then the pump-probe event should always appear at the same sample. However, it turned out that the triggering of the card had a jitter of 4 samples. This was overcome by not only capturing the signal of the MCT detector, but also measuring the trigger signal with the second channel of the scope card (see Fig. 3.7). Both channels are triggered at the same time, thus it is possible to correct the time axis of the channel with the MCT detector signal according to the position of the trigger peak in the other channel.

Instead of using the highest sampling rate of 50 Msamples/s, it is advisable to use an external clock synchronized with the probe pulses (see Fig. 3.7). In our case this reduced the noise level remarkably by a factor of 20 due to the suppression of beating

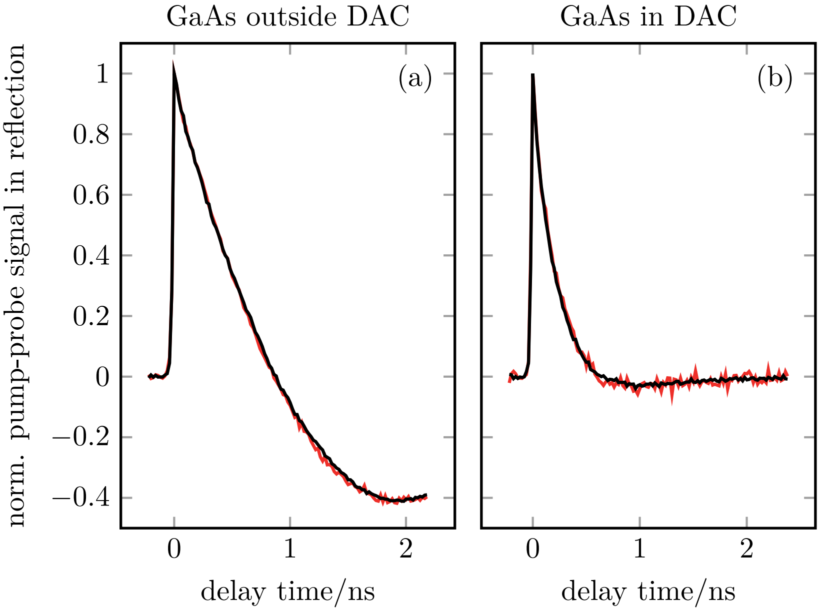

Figure 3.9: Normalized near-infrared pump – mid-infrared probe results on GaAs (a) outside the DAC and (b) on a different GaAs sample mounted in a DAC. The black pump-probe traces have been obtained via time-domain filtering, the red traces are measured with lock-in technique.

effects. However, it is crucial to tune the phase of the external clock such that the maximum signal of the probe pulses is captured.

# 4 Pressure-induced band gap filling in $VO_2$ observed by pump-probe spectroscopy

Vanadium dioxide ($VO_2$) is a strongly correlated electron material that shows an insulator-to-metal transition (IMT) at about 68°C from an insulating low-temperature to a metallic high-temperature phase. The transition temperature close to room temperature and the fact that it can be tuned by chemical doping, make $VO_2$ attractive for many applications [49–51]. In addition, there is a genuine scientific interest to understand the physical mechanisms behind the IMT, which has led to many investigations both experimental and theoretical, over several decades.

In section 4.1, an overview about material properties of $VO_2$ and prior results is given. Our samples are characterized in section 4.2. In the following section 4.3, our findings on $VO_2$ obtained with the new method of NIR pump – MIR probe spectroscopy combined with pressure application are presented. In section 4.4, we will summarize what we directly learn from our measurements and check for plausibility. We will combine these pieces of the puzzle to a uniform scenario in section 4.5 and discuss its relation to literature and our results. A summary of the main results and their interpretation is given in section 4.6.

## 4.1 Introduction and motivation

### 4.1.1 Structural phases of $VO_2$

The IMT in $VO_2$ was first observed by Morin [52] in 1959. It is accompanied by a structural phase transition (SPT) from a monoclinic M1 to a tetragonal R phase of the rutile-type structure, when going from the insulating to the metallic state with increasing temperature [53]. Besides these main phases, a number of polymorphic variants of $VO_2$ has been reported in literature. An overview is given by Galy [54]. Among these phases are the defect- or doping-induced monoclinic M2 and triclinic T phases, the pressure-induced structural phases M1′, X, O, M1″ and the metastable phases $VO_2$(A) and $VO_2$(B). Unfortunately, the nomenclature in literature is not fully consistent, for example, the triclinic T phase is sometimes labelled as M3. In this

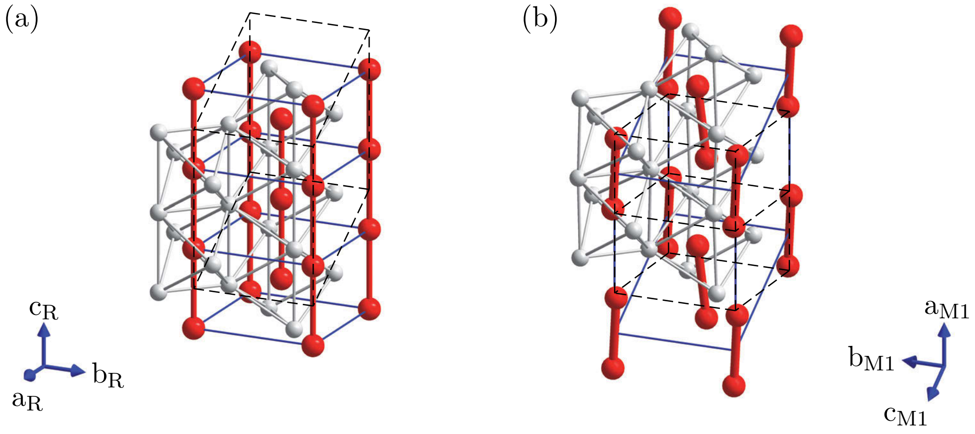

Figure 4.1: The two main structural phases R and M1 of $VO_2$. The red atoms correspond to V, the grey to O. The edges of the oxygen octahedra are marked with grey lines. The solid blue lines represent the unit cell of the structure, the dashed black lines represent the unit cell of the other structural variant. (a) Tetragonal rutile-type structure R with chains of V atoms along the $c_R$ axis, shown in red. (b) Monoclinic M1 structure with V–V dimers, shown in red. The axes are related by $a_{M1} = 2c_R$ and $c_{M1} = a_R - c_R$ [56].

subsection we will describe the two main structural phases in detail and give an overview about the other modifications.

The structure of the metallic rutile-type R phase (space group $P4_2/mnm$) [55] is sketched in Fig. 4.1(a). The vanadium atoms (red) are placed on a body-centered tetragonal lattice. Each vanadium atom is surrounded by an octahedron of oxygen atoms (grey). These octahedra are stacked along the $c_R$ axis to form edge-sharing chains, with their aequatorial four oxygen atoms in one plane. The chains at the cell edge are shifted by $c_R/2$ relative to those at the center of the unit cell. For the two chains, the apical oxygen atoms point in the [110] and $[1\bar{1}0]$ directions, respectively, and connect neighbouring chains by corner-sharing perpendicular to the $c_R$ axis. Thus, the rutile-type phase of $VO_2$ can be considered as a combination of two sets of vanadium chains along the $c_R$ axis, shifted by $c_R/2$.

In the insulating monoclinic M1 structure (space group $P2_1/c$), the vanadium atoms are grouped to dimers along the $c_R$ axis, see Fig. 4.1(b) [56]. This leads to a doubling of the cell in comparison to the rutile-type R phase. In addition, the dimers of the monoclinic M1 structure are slightly tilted by about 5° relative to the orientation of the $c_R$ axis [57]. In the standard definition of the cell parameters, $a_{M1}$ corresponds to $2c_R$. The reorientation of the vanadium atoms leads to a zig-zag shape of the vanadium chains and a corresponding twisting of the octahedra. The phase transition from M1 to R is of first order. At the critical temperature $T_c$, the volume expands by 0.044 % [58], the monoclinic M1 cell has a higher density than the rutile-type R cell.

Under pressure, an isostructural transition from M1 to M1′ at a critical pressure $p_c = 12\,\mathrm{GPa}$ has been found by Mitrano *et al.* [59], who named the isostructural monoclinic phase Mx, but in the meantime M1′ has become the standard designation. The compressibility becomes more anisotropic in the structural phase M1′ [59–61]. While the compressibility along the b axis increases, the lattice parameter $c_{M1'}$ remains almost constant under further compression [59, 60]. Pair distribution function analysis demonstrates that the V–V dimers survive and the oxygen octahedra become more symmetric under pressure [57]. Theoretical calculations predict that the M1′ phase might coexist with another monoclinic phase called M1″, which should be characterized by reduced dimerization and zigzagging [62]. According to the calculations, the difference of lattice parameters between M1′ and the proposed M1″ phase is approximately negligible up to 20 GPa and grows remarkably under further compression, such that the M1″ phase develops slightly towards the rutile-type R phase (at 40 GPa the zigzag-displacement of M1″ is expected to be 40 % smaller than for M1′). The available experimental data does not allow to draw conclusions about this theory, in particular since the mentioned pair distribution function analysis [57] did not cover the relevant pressure range beyond 22 GPa.

However, at room temperature, above a pressure of 34 GPa Bai *et al.* observed the coexistence of the structural phase M1′ with another monoclinic, baddeleyite-like structural phase X, and between 43 GPa and 55 GPa $VO_2$ fully develops into this X phase [61]. These results are essentially confirmed by Zhang *et al.*, but they report a broader pressure range from 26 GPa to 59 GPa for the coexistence of the M1′ and X phases [63]. Li *et al.* observed a coexistence of M1′ and another high-pressure phase between 37 and 51 GPa [60]. Since the observed lattice parameters of this high-pressure phase were different from those of X, they called the phase beyond 51 GPa not X but Mx [60]. Bai *et al.* also studied pressure-induced phase transitions at a temperature $T = 383\,\mathrm{K}$ [61]. At a pressure of 14 GPa, they observed a transition from the rutile-type R to a $CaCl_2$-type orthorhombic phase which they named O [61]. Beyond 38 GPa they report coexistence of the O and X phases and above 53 GPa a pure X phase [61]. Chen *et al.* have determined phase boundaries in the pressure–temperature phase diagram by means of Raman studies [64].

In Fig. 4.2 we show a schematic phase diagram wich summarizes the current knowledge about high-pressure structural phases in the pressure range up to 60 GPa and from room temperature to beyond the critical temperature [59–61, 63, 64]. Only the bound-

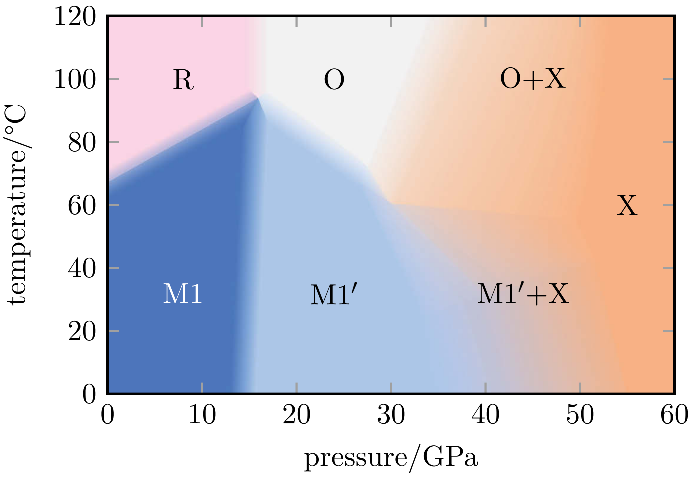

Figure 4.2: Schematic pressure–temperature phase diagram of $VO_2$ structures, adapted from [64] using especially the data of [61]. Shaded areas symbolize uncertainties of the phase boundaries and the regimes of coexistence with the X phase.

aries of the M1 and M1′ have been studied systematically [64]. The shaded transition zones symbolize uncertainties of the transition pressures and temperatures. According to Zhang *et al.* [63], the regimes of coexistence with the X phase extends over a larger pressure range.

According to Bai *et al.*, in the X phase the vanadium chains and their Peierls distortion disappear and metallization is established, as the vanadium ions become 7-fold coordinated [61]. In a recent publication, a successive increase of the coordination number of the vanadium atoms is reported for the pressure range from 30 GPa to beyond 200 GPa [65]. There, it is suggested that the X phase may be monoclinic or orthorhombic. This demonstrates that further experimental work is needed to fully determine the high-pressure structures.

A further monoclinic phase named M2 and an intermediate triclinic phase T (separating M1 and M2, sometimes named M3) can be stabilized at ambient pressure via substitutional doping or through defect states [54, 66–68]. Phase stabilization of these insulating phases can also be achieved by tensile strain [69–73]. In M2 one of the two vanadium chains has unpaired zigzag form and the other chain consists of untwisted V–V dimers [66, 67]. Mitrano *et al.* observed via XRD that M2 and T induced by Cr-doping (in the order of several permille up to percent) develop into the M1 phase when pressure of a few GPa is applied [59]. In addition, Baldini *et al.* report that the pressure-induced M1′ phase is different from the structural phases M2 and T [57].

In literature, there is also work on the so-called $VO_2(A)$ and $VO_2(B)$ phases. These are metastable phases obtained via hydrothermal synthesis or decomposition of $V_2O_5$ in reducing atmosphere [74]. $VO_2(A)$ and $VO_2(B)$ become amorphous under pressure [75, 76]. We expect that these phases play no role in our experiments.

### 4.1.2 Electronic properties of $VO_2$

The electronic band structure of the conducting rutile-type R phase can be derived from molecular orbital theory as demonstrated by Goodenough [53]: The vanadium atoms give 4 electrons to oxygen atoms and keep only one electron. In the octahedral ligand field, the d-orbitals of the $V^{4+}$ atoms split into molecular orbitals of $E_g$ and $T_{2g}$ symmetry, the latter with lower energy [53]. Since the octahedra have shared edges only along the $c_R$ direction and are thus slightly deformed, the states of $T_{2g}$ symmetry are further split [53]. The orbital oriented along $c_R$ has $A_{1g}$ symmetry and is lowered in energy due to overlap of the vanadium orbitals. These orbitals form a band called $d_{||}$ because of their orientation along the vanadium and octahedra chains. The two other former $t_{2g}$ orbitals have $E_g$ symmetry and become $e_g^\pi$ bands. In the metallic rutile-type R phase the $d_{||}$ band overlaps with the $e_g^\pi$ bands [53] and the conductivity shows no anisotropy [77]. A schematic band structure [53, 78] of the conducting rutile-type R phase of $VO_2$ is shown in Fig. 4.3(a).

In the insulating monoclinic M1 phase, the $e_g^\pi$ band is lifted up in energy due to the tilting of the dimers [79], see Fig. 4.3(b). Moreover, the dimerization leads to a splitting of the $d_{||}$ band into bonding and antibonding bands similar to the band splitting known from the 1D chain Peierls transition (see section 2.1). Besides these two effects, the Peierls splitting and the shift of the $e_g^\pi$ band, electronic correlations contribute to the opening of a band gap, which is in total about $E_\mathrm{g} = 0.6\,\mathrm{eV}$ [80] close to $T_\mathrm{c}$ [53, 81, 82].

The metallic rutile-type R phase and the insulating monoclinic M1 phase have been studied by several photoemission spectroscopy (PES) and X-ray absorption spectroscopy (XAS) experiments [78, 79, 83–91]. In addition, there are numerous studies on the electronic and optical properties of the insulating M1 and conducting R phases in equilibrium [80, 92–97]. For high quality samples, resistivity changes around 4 orders of magnitude have been reported [98, 99].

The observation of a coupled structural phase transition (SPT) and insulator-to-metal transition (IMT) raises the fundamental question about the mechanism driving the phase transition. From early times it has been discussed whether the insulating phase originates from a Peierls instability or from electronic correlations [53, 100–102].

A lot of effort was spent on the theoretical description of Mott-Hubbard systems and the archetypical material $VO_2$ [12, 26, 28, 53, 82, 103–113]. The discussion lead to an

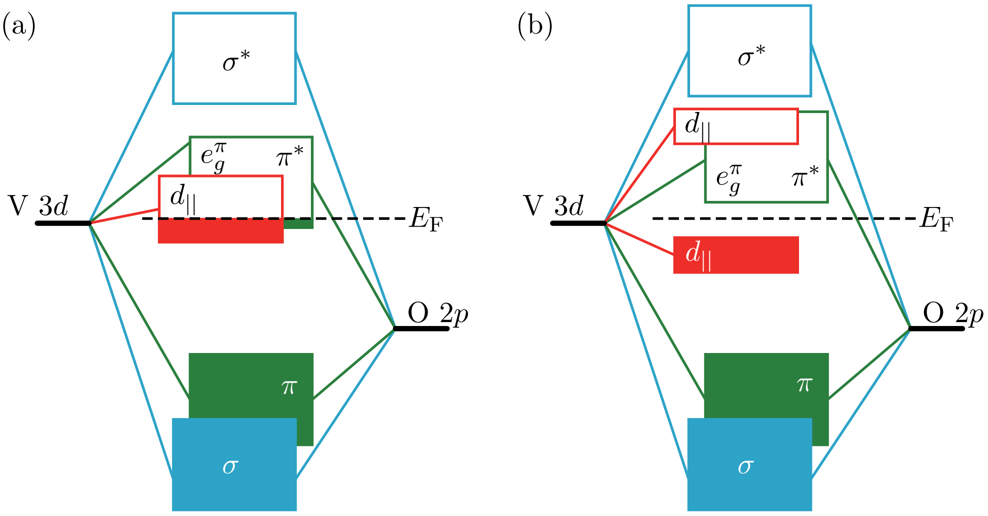

Figure 4.3: Schematic band structure of $VO_2$ in (a) the metallic R and (b) the insulating M1 phase, adapted from Aetukuri *et al.* [78]. Occupied states are marked by coloured filling. The dashed lines correspond to the Fermi energy $E_F$.

understanding of the insulating phase of $VO_2$ as Mott-Peierls insulator. However, contradicting scenarios for the transition mechanism are reported. For example, Biermann *et al.* describe a correlation-assisted Peierls transition [82], while Weber *et al.* report on a Peierls-assisted orbitally selective Mott transition [108]. There are also models able to predict both Mott- as well as Peierls-like behaviour, see for example Nájera *et al.* [111]. Many recent publications are based on density functional theory (DFT) with cluster dynamical mean-field theory, which was introduced by Biermann *et al.* [82], but other approaches have been demonstrated as well, for example parameter-free GW calculations by Gatti *et al.* [112].

Experimental activities have concentrated on a disentangling of the SPT and IMT. Gray *et al.* combine XAS, PES, X-ray diffraction (XRD) and observe that at a temperature $T_{\text{corr}} < T_{\text{IMT}}$ a purely electronic phase transition occurs, when the Coulomb correlations within the dimers soften [79]. This agrees with results obtained via PES, electron microscopy and electron diffraction measurements by Laverock *et al.* [90]. In a quite recent paper, Lee *et al.* [114] report the stabilization of a monoclinic metallic phase of $VO_2$ in a bilayer heterostructure of $VO_{2-\delta}/VO_2$. By combined XRD and IR transmission measurements, Nag *et al.* observe that the hysteresis of the structural transition is wider than the hysteresis of the IR transmission, and conclude that less energy is needed for the completion of the IMT than for the completion of the SPT [115]. Qazilbash *et al.* demonstrated by scattering scanning near-field infrared microscopy that the sample switches inhomogeneously by nucleation and growth, *i. e.* they observed phase coexistence of metallic and insulating regions [116]. Besides such attempts to stabilize and identify an intermediate phase between insulating M1 and conducting R, ultrafast methods have been developed and applied to $VO_2$ in order to track the time-dependent evolution of IMT and SPT and identify transient states.

### 4.1.3 The ultrafast insulator-to-metal transition in $VO_2$

The photo-induced phase transition to a non-equilibrium metallic phase of $VO_2$ on a femtosecond time scale first reported by Becker *et al.* [117] has attracted a lot of attention. Typically, for the ultrafast IMT the electron system of the insulating M1 phase is photoexcited by an optical or NIR pump laser with photon energies larger than the band gap. The electron system has been probed by means of optical, NIR and MIR spectroscopy, as well as THz time-domain spectroscopy [19, 118–125], angle-resolved light scattering technique [125], scattering-type near-field scanning optical microscopy methods [70, 71], ultrafast X-ray and extreme ultraviolet absorption [91, 126, 127], as well as through time-resolved PES [89]. The evolution of the lattice was studied indirectly by means of coherent phonons [18, 19, 125, 128, 129] and directly via ultrafast X-ray diffraction [118, 119], and in particular ultrafast electron diffraction (UED) [130, 131]. An unconventional kind of ultrafast IMT was demonstrated in terms of a THz field-induced tunnelling breakdown of the insulating state [132–134].

When the system is pumped above a critical threshold fluence $\Phi_{\mathrm{th}}$, switching to a transient metallic state can be photo-induced [118, 120, 121]. Via time-resolved PES, Wegkamp *et al.* demonstrated that the photo-induced band structure renormalization appears immediately with the pumping on an ultrafast time scale of several tens of femtoseconds [89]. This is much faster than the structural dynamics, which exhibits three different time scales as reported by Baum *et al.* [130]. First, the dimers stretch with a characteristic time constant $\tau_1 = 300\,\mathrm{fs}$ [130]. This time scale might be even shorter, as the 300 fs match the time resolution of their UED set-up [130]. However, the tilting of the former dimers disappears only on a picosecond time scale ($\tau_2 = 9\,\mathrm{ps}$) and then the lattice relaxes to the rutile-type R cell dimensions on a time scale of several hundred picoseconds [130]. Such different time scales have also been reported by Lysenko *et al.* [125], who used ultrafast angle-resolved light scattering technique and could resolve the role of anisotropic internal misfit strain in the ultrafast SPT dynamics of thin film samples. In conclusion, at the ultrafast IMT, a transient metallic phase evolves and the SPT is driven by the photoexcited electron system [89].

There are several interesting observations about the temperature and fluence dependence of the ultrafast IMT. Pashkin *et al.* found for the temperature range from 250 K to 330 K that after photoexcitation with $\Phi_{\mathrm{th}}$ the energy deposition in the excited surface layer equals the thermodynamic energy difference of the R and M1 phase [120]. From the observed threshold fluences at room temperature $\Phi_{\mathrm{th}}$, a V–V dimer excitation density in the order of 10 % can be estimated [120], which agrees with [130]. Cocker *et al.* captured a $\Phi$–$T$ phase diagram for $10\,\mathrm{K} < T < 330\,\mathrm{K}$ and report four different pump regimes [121]. Depending on the sample temperature and the pump fluence, by photoexcitation an insulating, an intermediate metallic, a regime with nucleation and growth of the metallic state, or a saturation region, where the full sample is switched to a metallic state can be reached [121]. According to Cocker *et al.*, the intermediate metallic regime is not accessible at room temperature [121]. Hilton *et al.* report enhanced photosusceptibility when the sample temperature is approaching $T_{\mathrm{c}}$ from the insulating phase and a significant drop of the pump-probe signal amplitude for temperatures above $T_{\mathrm{c}}$ [122].

### 4.1.4 Electronic properties of $VO_2$ under pressure

The behaviour of $VO_2$ under pressure is a quite new research field. Before 2007, very few studies of $VO_2$ under pressure have been published [29]. These were concerned with the pressure dependence of the critical temperature $T_{\mathrm{c}}$ for the transition from M1 to R [94, 95] and the pressure–temperature phase diagram of chromium doped $VO_2$ [66]. However, pressure is an interesting tool for decoupling the SPT and IMT in $VO_2$. The aforementioned structural studies have demonstrated that at room temperature the lattice symmetry of $VO_2$ stays monoclinic, however, with a variety of polymorphic phases. MIR spectroscopy [29, 60, 63, 135], XAS [136], and transport measurements [61, 64, 137] have been used to study the electric properties of these phases and to search for metallization.

Arcangeletti *et al.* concluded from their MIR reflection and transmission measurements, which they used for the calculations of the optical conductivity $\sigma(\omega)$, that metallization starts at 10 GPa via band gap filling [29]. A similar behaviour is reported for Cr-doped $VO_2$ [135]. Marini *et al.* did X-ray absorption near-edge structure (XANES) measurements up to 15 GPa and observed a small spectral weight transfer under pressure in comparison to the thermal transition, but conclude pressure-induced metallization [136].

In contrast to these reports are conclusions based on dc-resistivity measurements. Bai *et al.* observe a monotonous decrease of resistivity with increasing pressure until the X-phase is reached and conclude that metallization occurs in the X-phase [61]. Results by Chen *et al.* confirm this interpretation [64]. They conclude from temperature-dependent transport measurements above room temperature that $VO_2$ is insulating in the M1′ phase and behaves like a semiconductor. In contrast to Bai *et al.*, they observe a plateau in their pressure-dependent resistivity between 10 and 20 GPa. X. Zhang *et al.* observe a resistivity hysteresis for compression and decompression in the pressure range up to 20 GPa [137]. Taking into account additional temperature dependent resistivity data for $90\,\mathrm{K} < T < 270\,\mathrm{K}$, they relate the corresponding critical pressure of 10.4 GPa with a semiconductor-to-semiconductor transformation [137].

H. Zhang *et al.* [63] and Li *et al.* [60] report saturation of the reflection signal at pressures above 43 GPa and 37 GPa, respectively. The latter interpret this as occurrence of pressure-induced metallization in the M1′ phase that can be attributed to electron-electron correlations [60]. However, according to H. Zhang *et al.* this does not hold for all samples, but some of their own samples become metallic in the X phase, thus indicating that the IMT is caused by the SPT [63].

Such discrepancies as discussed above and reported *e. g.* by H. Zhang *et al.* [63] illustrate the inconsistent description of the electronic properties of $VO_2$ under pressure. This calls for the application of other, innovative techniques to obtain more insight into the nature of the pressure-induced IMT. Especially the pressure range below the appearance of the metallic X phase should be studied for signatures of a bandwidth-driven Mott-Hubbard transition. The experimental challenge is to probe free charge carriers and correlated electrons simultaneously while the samples are kept within a DAC. This challenge can be met with our NIR pump – MIR probe set-up. To the best of our knowledge, we provide here the first data obtained with such a combination of NIR-pump – MIR-probe and pressure technique. Our results are of high interest for testing of novel theoretic results [111].

At this position we acknowledge the pioneering work of Hsieh *et al.* who used optical pump – IR probe technology for a study of coherent phonons on pressurized $VO_2$ [18]. They report the signature of a monoclinic transient metallic phase. Their approach could be useful in order to check the lattice after an ultrafast IMT. On the other hand, with a probe photon energy well above the band gap of $VO_2$, their experiment is not suitable for the detection of free charge carriers. In contrast, our set-up brings the advantages of minimized heat introduction and a probe photon energy far below the expected band gap, thus being highly sensitive to free charge carriers.

To conclude, here we follow the hints that the pressure-induced IMT in $VO_2$ appears to be decoupled from the SPT. Pressure-induced changes in the equilibrium phase could have strong impact on the ultrafast response. Therefore we will examine, how the dynamics and the threshold of the ultrafast IMT evolve under pressure. Finally, the study of the pump-probe response enables us to make conclusions about the non-excited state of $VO_2$ under high pressure.

## 4.2 Sample characterization

### 4.2.1 Sample preparation

Our experiments were performed on single crystals of $VO_2$ provided by the group of Lynn A. Boatner, Oak Ridge National Laboratory [138]. The crystals have been grown via thermal decomposition of $V_2O_5$ under a continuous flow of Ar gas [138]. After 120 h processing time, plate-like crystals of a few hundred microns thickness and several square millimeters area were obtained [138]. The $\mathrm{a_{M1}} = 2\mathrm{c_R}$ axis lies in the plane of the plate-like crystallites. In the monoclinic M1 phase, the crystals show twin domains [138]. For high-pressure experiments, the $VO_2$ crystals were polished to a thickness in the order of 10–30 µm, then of each piece several samples were cut with dimensions suitable for the DAC.

### 4.2.2 Raman study under pressure

The pressure-induced isostructural phase transition from M1 to M1′ at room temperature was observed by Raman spectroscopy. A thin $VO_2$ sample of less than 15 µm thickness and lateral dimensions between 20–30 µm has been used. The sample was excited at a wavelength of 532 nm and unpolarized Raman spectra were measured by means of a Jobin-Yvon LabRAM HR 800 (*Horiba*) spectrometer equipped with a cryogenically cooled silicon CCD camera.

Typical spectra obtained at pressures of 5.5 and 16.9 GPa are shown in Figs. 4.4(a) and 4.4(b) together with the pressure-induced shift of the Raman lines, see Fig. 4.4(c). The results are in excellent agreement with literature [29, 60, 61, 63, 64]. The phonons harden under pressure, *i. e.* their frequencies increase, and for some modes there appears a kink at a pressure around 12 GPa, which is related to the isostructural transition from M1 to M1′ [61].

### 4.2.3 Temperature-driven insulator–metal transition

The thermal phase transition was observed by tracking the temperature-dependent linear reflection signal $R_{\mathrm{lin}}$ at $\lambda = 10\,\mu\mathrm{m}$ from a $VO_2$ crystal mounted in an evacuated cryostat. The attribute *linear* (or subscript *lin*) with respect to reflection and transmis-

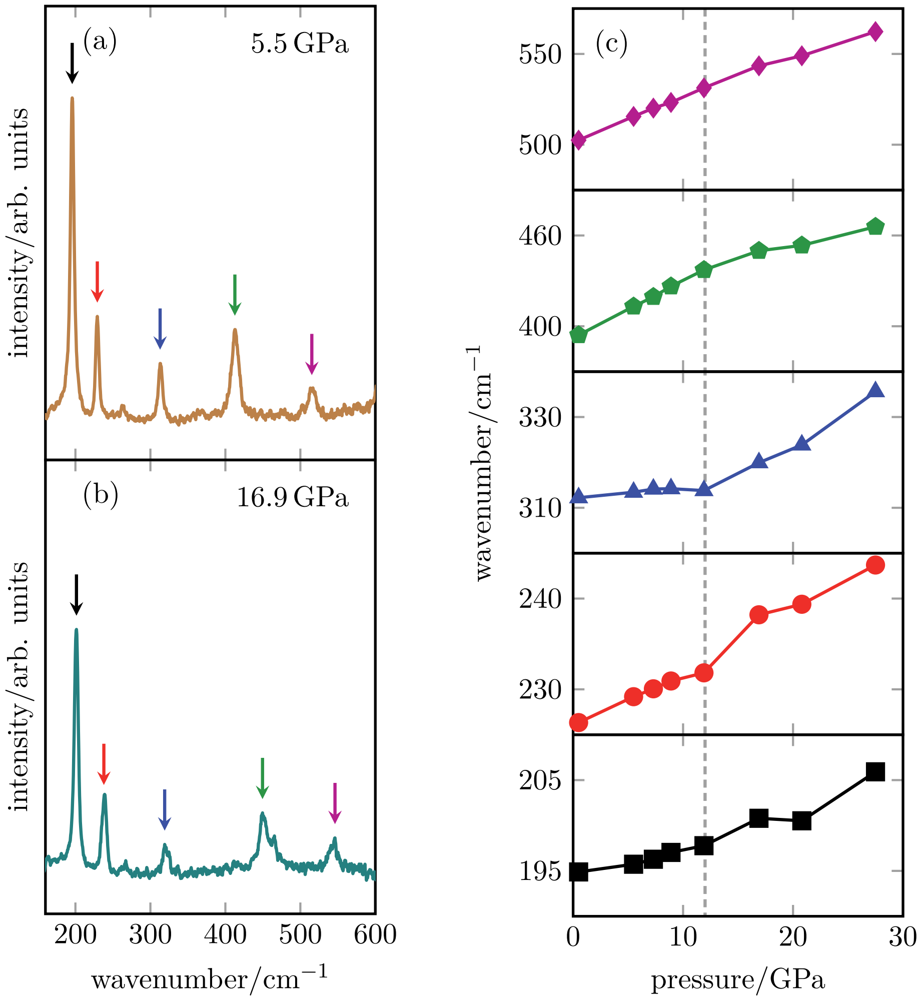

Figure 4.4: Raman spectra obtained at (a) 5.5 GPa and (b) 16.9 GPa. The pressure dependence of the modes marked with coloured arrows in (a) and (b) is shown in (c). The errors are smaller than the size of the symbols.

sion means in the following that we refer to a signal not affected by any pump light. In order to ensure a good thermal coupling between the sample and the cold finger of the cryostat, the crystal had been placed directly with its backside on a Cu mount. Below $T_c$, the measurement might be affected by this mount, as $VO_2$ in the insulating phase is transparent at $\lambda = 10\,\mu m$ and the Cu support might contribute to the reflected signal intensity.

The obtained data shown in Fig. 4.5 are normalized to the initial reflection signal. In perfect agreement with literature, there is a distinct step in reflection at 338 K, marking the critical temperature $T_c$. The transition to a metallic phase is further supported by

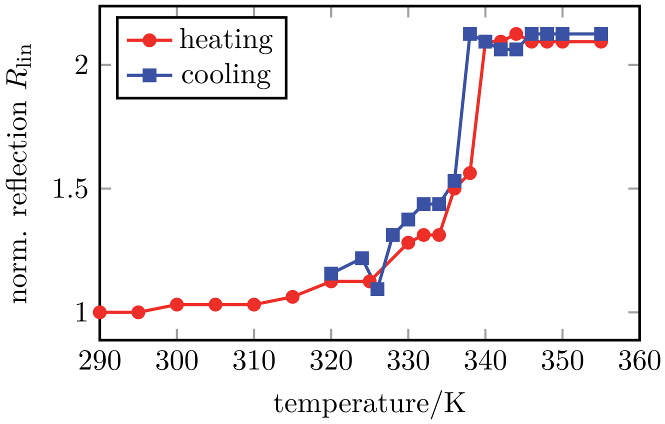

Figure 4.5: Hysteresis of the reflection signal at $\lambda = 10\,\mu\mathrm{m}$ obtained from a $VO_2$ crystal mounted on a Cu sample holder. The data are normalized to the starting value observed under heating from 290 K.

the saturation of the reflection signal at temperatures above 338 K. The small width in the order of 3 K of the hysteresis associated with the first order phase transition demonstrates the high homogeneity and quality of the $VO_2$ crystal. The observed growth of the reflected signal intensity under heating below $T_\mathrm{c}$ is possibly related to interference effects within the sample.

## 4.3 Ultrafast pump-probe results

### 4.3.1 Data acquisition

For the ultrafast measurements, the NIR pump – MIR probe set-up described in section 3.2 was used. With the Ti:Sa pump photons $E_\mathrm{pump} = 1.55\,\mathrm{eV}$, electrons can be excited above the band gap $E_\mathrm{gap}(0\,\mathrm{GPa}) = 0.6\,\mathrm{eV}$ by single photon absorption. In order to be particularly sensitive to free charge carriers, the probe photon energy has to be much smaller than the band gap energy. The probe wavelength was set to $\lambda_\mathrm{probe} = 10\,\mu\mathrm{m}$, which corresponds to a photon energy $E_\mathrm{probe} \approx 0.12\,\mathrm{eV}$.

For an estimate of the band gap we analyze the temperature dependent resistivity traces of Chen *et al.* measured on single-domain nanobeams in quasi four-probe geometry [139]. Approximating the data with an Arrhenius law for the resistance $\rho(T) = \rho_0 e^{\frac{E_\mathrm{g}}{2k_\mathrm{B}T}}$, it can be concluded from the slope that the band gap is larger than 0.6 eV in the pressure range up to 20 GPa. This approximation is much more reliable than the band gap estimates of Bai *et al.* [61] and H. Zhang *et al.* [63]. The former use an Arrhenius law to fit pressure-dependent changes of the resistivity, although the formula describes only the temperature dependence [61]; the latter estimate the band gap energy from the vanishing transmission of a thick sample, which due to absorption at intra-gap states [29] will underestimate the real gap [63]. In summary, according to our estimate the band gap energy is well above the photon energy of our probe.

There are two reasons, not to choose a larger probe wavelength than 10 µm. First, we are interested in the electronic answer of the system. For this purpose the probe photon energy should be above 85 meV, since below this value features of phonon resonances can be observed [19, 97]. Here, we have to take into account phonon hardening under pressure, which shifts the highest phonon mode to about 93 meV at 30 GPa [60, 61]. Second, we have to consider the limited sample area and the achievable spot size in focus. In order to avoid artefacts, the probe spot should be smaller than the sample. Overall, the selected probe wavelength $\lambda_{\mathrm{probe}} = 10\,\mu\mathrm{m}$ is a good compromise for all these requirements.

The pump-probe experiment was performed in reflection geometry for each pressure $p$ with a series of different pump fluences $\Phi$. The pump-induced change in reflection $\Delta R_{\mathrm{lockin}}(\Phi, p, t)$ as function of the delay time $t$ was measured by lock-in technique with chopped pump. In order to obtain the relative pump-induced change of the reflection signal, $\Delta R(\Phi, p, t)$ has to be referenced to the linear reflection signal $R_{\mathrm{lin}}(p)$. At each pressure, the linear reflection signal $R_{\mathrm{lin,scope}}(p)$ was determined by an oscilloscope. This signal is scaled by a calibration factor correcting for the ratio of the probe signals measured by lock-in technique and by the scope, $R_{\mathrm{cal,lin,scope}}/R_{\mathrm{cal,lin,lockin}}$, which was taken at one pressure, when the chopper was placed in the probe beam. Thus, it was not necessary to move the chopper from the pump to the probe beam at each pressure, but only once for the calibration measurement. The relative pump-induced change of the reflection signal is

$$\frac{\Delta R(\Phi, p, t)}{R_{\mathrm{lin}}(p)} = \frac{\Delta R_{\mathrm{lockin}}(\Phi, p, t) - \Delta R_{\mathrm{offset,lockin}}(\Phi, p)}{R_{\mathrm{lin,scope}}(p)} \cdot \frac{R_{\mathrm{cal,lin,scope}}}{R_{\mathrm{cal,lin,lockin}}}, \tag{4.1}$$

where $\Delta$ marks pump-induced signal changes. $\Delta R_{\mathrm{lockin}}(\Phi, p, t)$ is corrected for a small thermal offset $\Delta R_{\mathrm{offset,lockin}}(\Phi, p)$ observed at high fluences $\Phi$. This offset originates from a multi-pulse heating effect in the intervals when the chopper is not blocking the beam. It was determined by averaging data points of the plateau at negative delay time.

### 4.3.2 Temperature-dependent pump-probe measurements

The pressure-dependent pump-probe experiments were performed at room temperature. Before concentrating on these measurement series, we present pump-probe results for a reference sample mounted in a cryostat as described in section 4.2.3. For this experiment the offset-correction is important, as the surface of the sample in the evacuated cryostat can easily heat up under pump fluence.

In Fig. 4.6(a) the fundamental difference of the pump-probe signal from the insulating M1 and the metallic rutile-type R phase is shown. Schematic band diagrams of these two phases are shown in Figs. 4.6(b) and 4.6(c). There the distribution of a finite density of states (DOS) is given on horizontal energy axes and the DOS coloured grey refers to filled states. At 290 K, *i. e.* below $T_\mathrm{c}$, the sample is insulating with a band gap $E_\mathrm{gap}(0\,\mathrm{GPa}) = 0.6\,\mathrm{eV}$. Ti:Sa pump photons $E_\mathrm{pump} = 1.55\,\mathrm{eV}$ excite electrons from the $d_{||}$ band to the $e_g^\pi$ band as marked with a red arrow in the schematic band diagram of Fig. 4.6(b). Thus, pumping produces additional free charge carriers and therefore the reflection rises. The absorption length of $VO_2$ at a wavelength of 800 nm is about 100 nm [130]. This means that we photoexcite only a thin layer at the surface of the sample. However, the probe which cannot excite beyond the band gap is sensitive for much deeper parts of the sample. Consequently, the pump-induced reflectivity increase is only in the order of percent.

Starting from the metallic rutile-type R phase, *i. e.* above $T_\mathrm{c}$, we observe a slight pump-induced reduction of the reflected signal (see red trace in Fig. 4.6(a)). At 360 K the band gap has collapsed as sketched in Fig. 4.6(c). The impact of pumping is limited, since a much higher number of free charge carriers is present than are excited by pump photons. Furthermore, it is not possible to photoexcite charge carriers with the Ti:Sa pump photons $E_\mathrm{pump} = 1.55\,\mathrm{eV}$ from completely filled bands to unoccupied states, as the energy between conduction and valence band is about 2.5 eV [92]. Thus, our pump cannot increase the number of free charge carriers. However, it can excite electrons in the valence band which causes a heating of the electron system. As typical for a metal, a temperature increase leads to reduced conductivity and therefore we observe a small negative pump-probe amplitude in reflection. All these results agree with literature [120].

It will be interesting to check, whether the pump-probe amplitude disappears when pressure is applied on a sample at room temperature in a way similar to the temperature-induced phase transition. Such a behaviour can be expected for a hypothetical pressure-induced band gap closure similar to the thermal IMT.

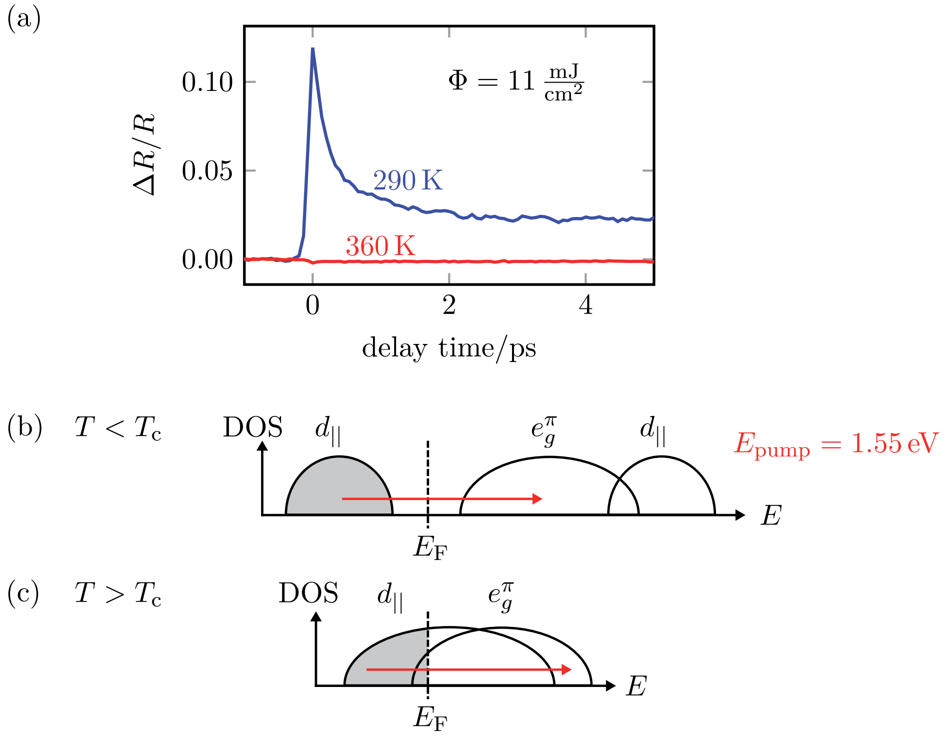

Figure 4.6: (a) Pump-probe signals at a fluence of $11\,\mathrm{mJ/cm^2}$. The blue trace was captured at a base temperature of $290\,\mathrm{K} < T_\mathrm{c}$, the red trace at $360\,\mathrm{K} > T_\mathrm{c}$. Corresponding schematic band diagrams are shown in (b) for the insulating ($T < T_\mathrm{c}$) and (c) for the metallic ($T > T_\mathrm{c}$ phase). The red arrows symbolize how the pump photons excite the charge carriers.

### 4.3.3 Pressure- and fluence-dependent pump-probe measurements

Figure 4.7(a) displays pump-probe traces corrected according to equation (4.1) obtained from $VO_2$ at a pressure of 2.1 GPa. On the horizontal axis, the delay time between the probe and pump pulses is shown, where a positive time means that the probe arrives after the pump. The colour coding describes different pump fluences. All traces show a quasi-instantaneous increase of reflectivity that is only limited by the durations of the pump and probe pulses. The onset is followed by a fast relaxation on a sub-picosecond time scale. At low fluence (blue), this relaxation dominates the pump-probe signal which then vanishes after about 1 ps indicating that all photoexcited charge carriers have returned to localized states. Above a certain fluence level, a persistent change of reflectivity is observed (green trace), becoming more prominent and eventually dominating (orange and red traces) when the fluence is further increased.

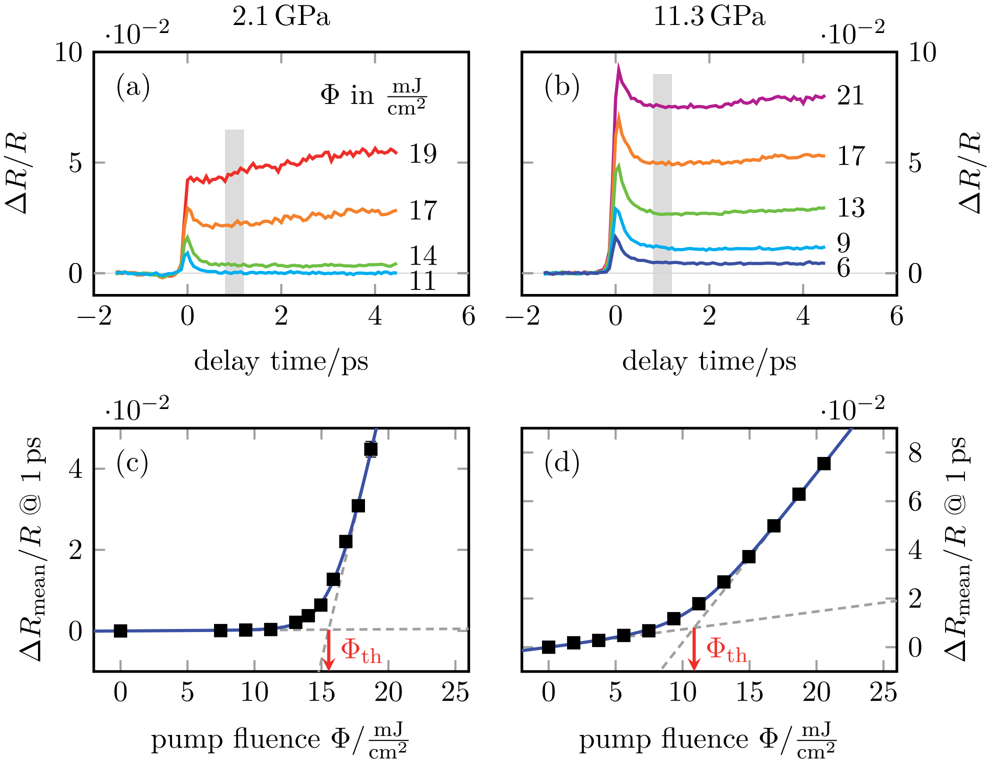

Figure 4.7: Pump-probe signals corrected according to equation (4.1) for different pump fluences $\Phi$ at room temperature and quasi-hydrostatic pressure of (a) 2.1 GPa and (b) 11.3 GPa. Time-averaged pump-probe signals for delay times between 0.8 and 1.2 ps (highlighted as grey area in (a) and (b)) versus pump fluence for (c) 2.1 GPa and (d) 11.3 GPa. Black squares represent experimental data, the blue lines show fits using equation (4.4). The crossing point of the asymptotes of the fit (dashed lines) defines the treshold fluence $\Phi_{\mathrm{th}}$. Details of the threshold fitting are explained in section 4.4.1.

All these observations agree with prior results reported on similar NIR pump – MIR probe experiments carried out at ambient pressure [19, 121]. The photoexcitation increases the number of free charge carriers, thus leading to an increased reflection of the probe beam. Above a threshold fluence $\Phi_{\mathrm{th}}(p, T)$, a critical density of free charge carriers is photoexcited that screen Coulomb interaction and thus induce the collapse of the energy gap and the switching to a metastable metallic state [19, 89]. The continued slow growth of the pump-probe amplitude at the highest fluences shown in Fig. 4.7(a) corresponds to thermal switching of further parts of the sample [121]. This can be due to growing in lateral direction, when only a part of the probed area was excited beyond the critical carrier density, but besides, it always can come from deeper volumes of the sample as we excite only a thin surface layer, but probe much deeper in the sample.

Remarkably, at elevated pressure we observe a pump-induced persistent change in the reflection signal already at very low fluences, see the blue traces in Fig. 4.7(b). However, there is still a non-vanishing threshold fluence $\Phi_{\mathrm{th}}$, above which the long-lived pump-probe response drastically increases. For a detailed analysis, we average the pump-probe signal of each trace in the time-frame $0.8\,\mathrm{ps} \leq t \leq 1.2\,\mathrm{ps}$. The position of this delay time interval is a compromise between completion of the fast relaxation process and low impact of the slowly rising thermal signal.

We plot the obtained $\frac{\Delta R_{\mathrm{mean}}(\Phi,p)}{R(p)}$ as function of the pump fluence $\Phi$ for each pressure. Fig. 4.7(c) corresponds to Fig. 4.7(a), and Fig. 4.7(d) to Fig. 4.7(b), respectively. A threshold behaviour can be clearly seen for both exemplary pressures. In addition, a fundamental difference in the low-fluence regime becomes obvious. A non-vanishing pump-probe signal exists around 1 ps only at the elevated pressure. Therefore, in contrast to literature reporting measurements at ambient pressure conditions [19, 120, 121], we define the threshold fluence $\Phi_{\mathrm{th}}(p)$ by the crossing point (marked by a red arrow) of asymptotes (dashed grey lines) for the high-fluence and low-fluence regime, as shown in Figs. 4.7(c) and 4.7(d).

## 4.4 Analysis and interpretation

### 4.4.1 Threshold fluence fitting

In order to determine the threshold fluence $\Phi_{\mathrm{th}}(p)$ we describe the fluence dependence of the pump-probe signal averaged around 1 ps for each applied pressure $p$ using a phenomenological bi-asymptotic fitting function

$$\frac{\Delta R_{\mathrm{mean}}(\Phi)}{R} = c \ln\left(a e^{s_1 \Phi} + (1-a)\, e^{s_2 \Phi}\right), \tag{4.2}$$

with four independent positive fit parameters $c, a, s_1$ and $s_2$. This definition forces the fit to pass through the origin, which is a proper condition since we have performed an offset correction. In the limit of very large or very small pump fluences, equation (4.2) is dominated by one of the exponential terms and the fitting function becomes nearly linear. The crossing point of these two asymptotes defining $\Phi_{\mathrm{th}}$ can be derived from the equality of both exponential terms:

$$\Phi_{\mathrm{th}} = \frac{1}{s_2 - s_1} \ln\left(\frac{a}{1-a}\right). \tag{4.3}$$

In order to achieve stable operation of the numerical fitting procedure we rewrite equation (4.2) using equation (4.3) and replace the parameter $a$ that exponentially approaches 1 for $\Phi_{\text{th}} \to \infty$ by the threshold fluence $\Phi_{\text{th}}$:

$$\frac{\Delta R_{\text{mean}}(\Phi)}{R} = c \ln \left[ \frac{e^{s_3 \Phi_{\text{th}}}}{1 + e^{s_3 \Phi_{\text{th}}}} e^{s_1 \Phi} + \left( 1 - \frac{e^{s_3 \Phi_{\text{th}}}}{1 + e^{s_3 \Phi_{\text{th}}}} \right) e^{(s_1 + s_3)\Phi} \right], \tag{4.4}$$

where $s_3 = s_2 - s_1$. Thus, the parameters obtained by fitting are $\Phi_{\text{th}}, c, s_1, s_3$.

The analysis of pump-probe traces at different pump fluences and various pressures revealed two key parameters that exhibit anomalous pressure behaviour, the threshold fluence $\Phi_{\text{th}}$ and the slope of the low-fluence asymptote $m_1 = cs_1$. In Fig. 4.8 the pressure dependence of these two parameters is shown together with the linear transmissivity and reflectivity. Black symbols correspond to the first measurement series, where a focus difference with pump smaller than the probe spot – in contrast to the other measurement series with pump larger than the probe spot – was corrected at the calibration, which only affects the $m_1$ values. The transmissivity was corrected for a scattered background signal and as well as the reflectivity referenced to the incident probe power. In Fig. 4.8 both, transmissivity and reflectivity, are normalized to their values at lowest pressure.

Starting from ambient pressure, the threshold fluence $\Phi_{\text{th}}$ monotonically increases up to a critical pressure $p_{\text{c}}$ around 7 GPa, see Fig. 4.8(a). A higher threshold fluence means that more charge carriers have to be photoinjected in order to achieve sufficient screening of Coulomb interactions, and thus to induce a metastable metallic phase. The increase of $\Phi_{\text{th}}$ with pressure is consistent with the reported growth of $T_{\text{c}}$ under pressure [64, 94] and the corresponding estimated increase of the latent heat of the IMT [64].

Around the critical pressure $p_{\text{c}}$ we observe an anomalous drop of the threshold fluence $\Phi_{\text{th}}$ within a pressure interval of a few GPa. Remarkably, the drop of the threshold fluence coincides with the vanishing of the transmissivity (Fig. 4.8(c)), the onset of an increased reflectivity (Fig. 4.8(d)) and of a finite slope $m_1$ of the low-fluence asymptote (Fig. 4.8(b)). These results have been obtained with high reproducibility. Different colours in Fig. 4.8 correspond to three different DAC fillings and pressure runs. For the three different loadings of the DAC we observe very similar trends. In Fig. 4.8 the background shade from grey to yellow highlights the change of behaviour at the critical pressure $p_{\text{c}}$.

With further pressure increase, the threshold fluence slightly decreases, while the reflectivity grows with further pressure increase. The slope $m_1$ decreases until it almost vanishes. It is remarkable that the threshold does not disappear in the studied pressure range (up to 23 GPa). This gives evidence that it is always possible to increase the number of free charge carriers beyond a critical density by photoexcitation over the band gap, and thus to induce a transition to a metallic phase. The persistence of the

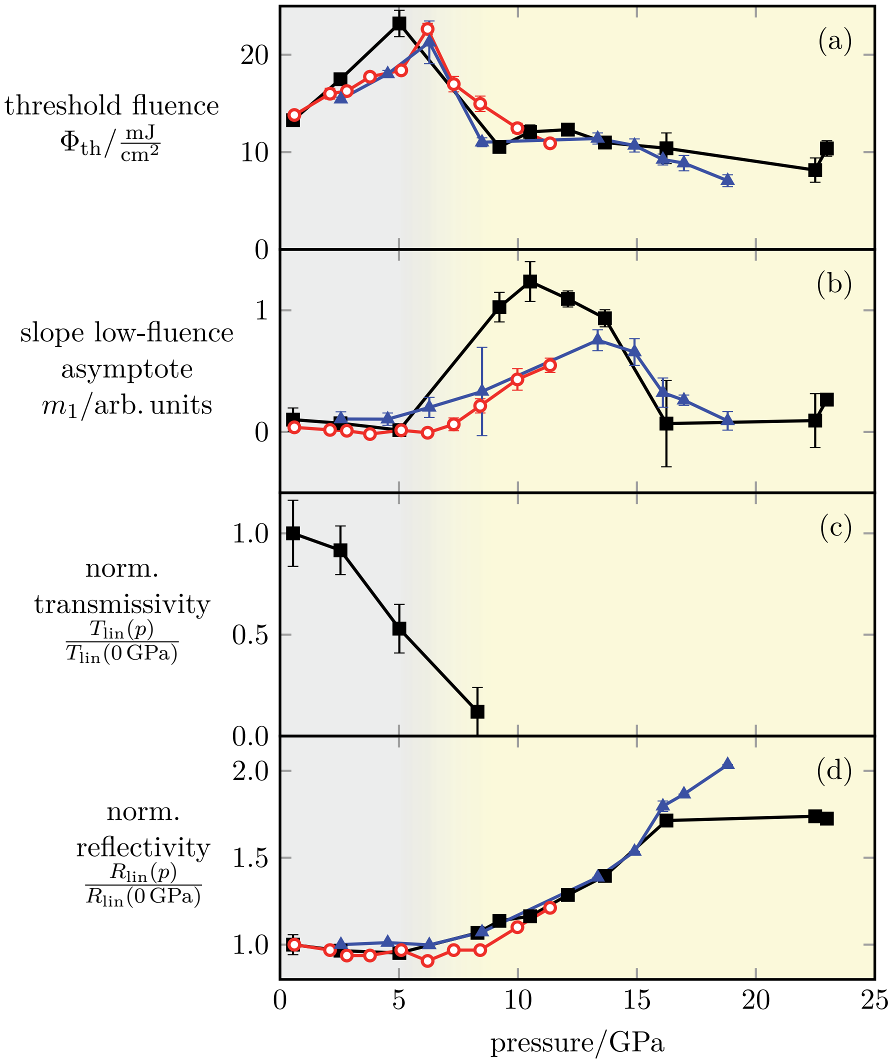

Figure 4.8: Pressure dependence of (a) threshold fluence $\Phi_{\mathrm{th}}$ and (b) slope $m_1$ of the low-fluence asymptote obtained from the fit using equation (4.4). (c) Normalized linear transmissivity and (d) reflectivity of $VO_2$ in the DAC as function of pressure. Different colours and symbols correspond to separate experiments performed on three different $VO_2$ crystals.

threshold agrees with the report of H. Zhang *et al.* [63], who observe that the band gap energy is reduced under pressure, but does not close in the pressure range studied in the present work.

The observed trends in the linear reflectivity and transmissivity are comparable to literature [29, 60, 63]. Identical to the results by Arcangeletti *et al.* [29], the reflectivity is stable up to pressures of several GPa and then starts to grow. The more pronounced decrease in our transmission data is related to the larger thickness of our sample.

A non-vanishing parameter $m_1$ means that it is possible to *non-cooperatively* (there is no critical density) excite charge carriers to a long-lived metastable state. In order to obtain better insight into its origin, we have to consider further experimental observations presented in the following sections.

### 4.4.2 Pre-edge pump-probe signal

The vanishing of the transmission is also visible in the pump-probe data measured in reflection geometry. As long as there is a finite transparency of the sample, reflection at its backside can contribute to the total reflectivity of the sample. The pump-probe experiment allows to test whether such a contribution exists.

At pressures below $p_\mathrm{c}$ we observe a negative pump-probe amplitude for small negative delay times around 0.5 ps, see Fig. 4.9. Simultaneous to the linear transmissivity (see Fig. 4.8(c)), the negative pump-probe amplitude decreases with increasing pressure and disappears above $p_\mathrm{c}$. The negative delay time means that the probe arrives on the sample before the pump. In such a situation, a finite part of the probe intensity will enter the sample and a fraction of this will be reflected at the backside of the sample. However, this back reflected probe light is at least partially suppressed when it returns to the then photoexcited surface of the sample. This pump-induced suppression is the origin of the negative pump-probe signal and with increasing pump fluence the latter gets more pronounced.

This interpretation is supported by the estimate of the propagation duration $t_\mathrm{prop}$ of the probe light in the sample

$$t_\mathrm{prop} = \frac{2 d_\mathrm{sample} n_\mathrm{sample}}{c}, \tag{4.5}$$

where we assume that the probe is incident approximately perpendicular to the sample surface. The factor 2 accounts for the way forward and backward and $c$ is the speed of light. For a sample thickness in the order of $d_\mathrm{sample} = 25\,\mu\mathrm{m}$ and a refractive index $n_\mathrm{sample}$ around 3.2 [97] we estimate a propagation duration of 0.5 ps. This perfectly agrees with the interval at negative delay times, where a negative pump-probe signal appears.

### 4.4.3 Pump-probe signal as a function of pressure

In Fig. 4.7 we have presented the pump-probe amplitude as a function of the fluence at a fixed pressure. However, it is also instructive to discuss the pump-probe signal as a function of increasing pressure at a fixed fluence, see Fig. 4.10, which is a measure

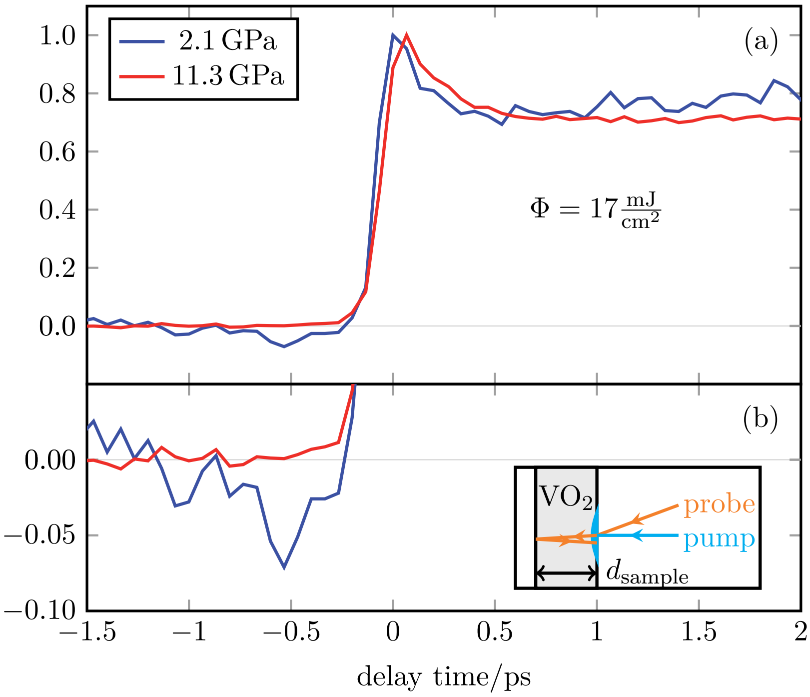

Figure 4.9: (a) Comparison of the normalized pump-probe signal for pressures below and above $p_\mathrm{c}$. (b) Zoom to the signals at small negative delay times. Below $p_\mathrm{c}$ (blue trace), a negative pump-probe amplitude is observed, at pressures above $p_\mathrm{c}$ this feature disappears (red trace). The inset in (b) schematically demonstrates the origin of the negative pump probe signal at negative delay time. The beam diameters are much larger than the arrows in the sketch.

of the photosusceptibility. In order to be able to compare at exactly the same pump fluence, we use the fit parameters obtained through equation (4.4) to interpolate the measured values and calculate the pump-probe signal. It is even possible to slightly extrapolate the fitted fluence range. Most appropriate is the discussion at a fluence above the initial threshold, but below the maximum threshold fluence. Here we have choosen a fluence of 20 mJ/cm$^2$, which means that at a few pressures with low threshold we had to extrapolate slightly beyond the fitted fluence range.

We first observe a drop of the pump-probe signal when $p_\mathrm{c}$ is approached, which is a consequence of the threshold $\Phi_\mathrm{th}$ increasing with pressure. Vice versa, at the critical pressure, the drop of $\Phi_\mathrm{th}$ leads to a drastic increase of the pump-probe signal. With the same amount of photo-induced carriers, a much larger part of the sample can be switched. The switching of a larger part of the sample is also the reason for the growth of the pump-probe signal at a fixed pressure when the fluence is further increased after passing the threshold. Remarkable at the traces shown in Fig. 4.10 is

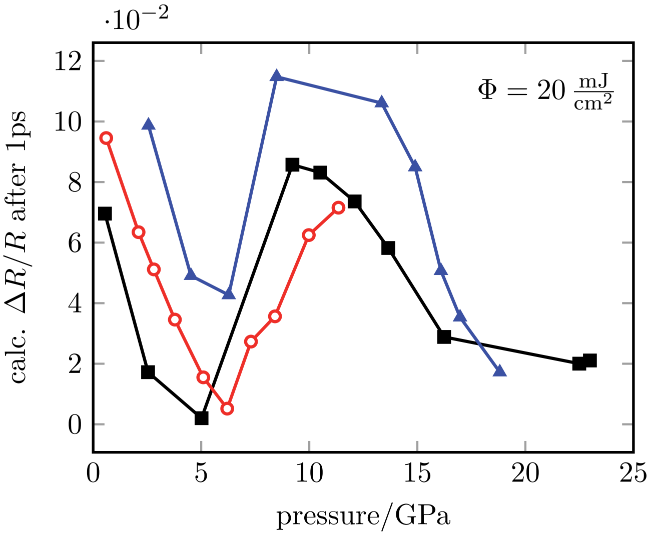

Figure 4.10: Pump-probe signal as function of increasing pressure at a constant pump fluence of 20 mJ/cm$^2$. The signal amplitude was calculated using the fit parameters obtained from equation (4.4). The colour coding corresponds to the three different samples presented in Fig. 4.8.

the significant decrease of the pump-probe signal from 10 GPa to 20 GPa. Following the argumentation around $p_c$ one would expect that the slightly decreasing threshold causes a small increase of the pump-probe amplitude, however, the opposite behaviour is observed. The lowered signal amplitude is not an artefact of extrapolated fitting curves, it also can be clearly observed at lower fluences (not shown).

The reduction of the pump-probe signal above 10 GPa appears to come along with the observed onset of the growth in reflectivity. At an increased level of linear reflectivity, the relative change induced by photoexcitation decreases. While the free charge carriers provided by pumping only have small effect on the linear reflectivity, they still play a major role for the switching to another phase which has slightly higher reflectivity. This observation calls for estimates of the plasma frequency and the critical density of charge carriers needed to drive the IMT. We will come back to this point in section 4.4.5.

### 4.4.4 Decompression behaviour

We also wanted to test the reversibility of the pressure-induced effects in VO$_2$. Since it is known that electronic properties of correlated oxides might not fully recover after decompression [140, 141], we performed measurements only at a few selected pressures under pressure release to see the trend. In Fig. 4.11 we present data obtained on decompression and compare with the results under increasing pressure of Fig. 4.8.

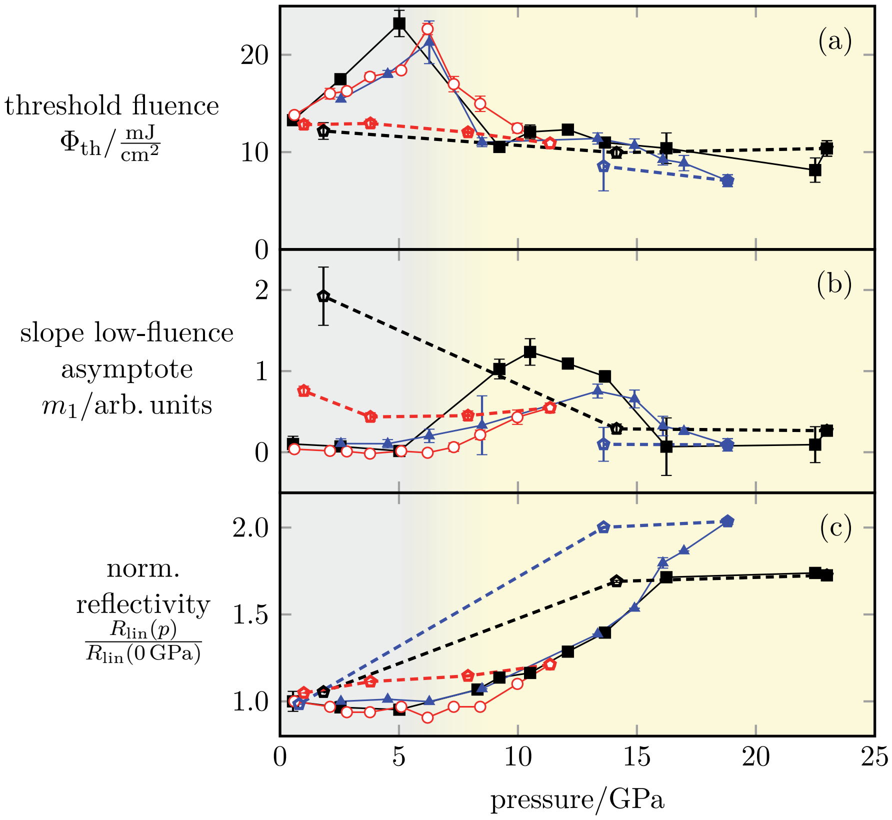

Figure 4.11: Decompression results for the threshold fluence $\Phi$, the slope $m_1$ of the low-fluence asymptote, and the linear reflectivity $R_{\text{lin}}$. For comparison, the results obtained under compression are plotted as well. The colour code is the same as in Fig. 4.8. The data points obtained on pressure release are marked with pentagons and connected by dashed lines.

The linear reflectivity returns on a hysteresis-like path down to its original value at lowest pressure, which agrees with literature [60]. In contrast, we did not observe any recovery of the transmission. This was concluded from the absence of a negative pump-probe signal at negative delay times (see section 4.4.2) and is therefore not shown in Fig. 4.11.

The threshold $\Phi_{\text{th}}$ recovers at least partially under decompression, but we do not observe an anomaly around $p_c$. Remarkably, the slope $m_1$ did not return to small values under decompression, but rose instead. The latter could be related to a different pressure treatment. In the measurement series marked in red in Fig. 4.11(b), between the measurements close to 4 GPa and at 1 GPa the pressure had been fully released, *i. e.* pressure was again applied to collect data at 1 GPa. Such a behaviour cannot just be explained by structural phase mixing under decompression as reported in literature

[60]. It would appear that $m_1$ stores the history of the sample, growing with each compression. This could also be the origin of the higher $m_1$ values for the first measurement series (black symbols in Fig. 4.11), since during the compression series after taking the measurement at 8 GPa the pressure was reduced to 4 GPa in order to check for a transmission signal (see Fig. 4.8(c)). A possible explanation for the behaviour of $m_1$ could be that it is related to the introduction of defect states as will be discussed later (see section 4.5).

The observed decrease of $m_1$ when pressure is increased beyond 12 GPa does not contradict this interpretation. This decrease of $m_1$ is reminiscent of the dramatic reduction of the pump-probe signal (see Fig. 4.10) in the same pressure range hinting to a possibly similar origin of these effects.

### 4.4.5 Estimates of carrier and excitation densities

Assuming homogeneous excitation along the absorption length, the density of charge carriers excited by the pump $n_{\mathrm{e,pump}}$ can be calculated as

$$n_{\mathrm{e,pump}} = \frac{\Phi}{d_{\mathrm{absorption}}(\lambda_{\mathrm{pump}})} \frac{\lambda_{\mathrm{pump}}}{hc}, \tag{4.6}$$

where $h$ is the Planck constant. With an absorption length $d_{\mathrm{absorption}} = 100\,\mathrm{nm}$ at our pump wavelength $\lambda = 800\,\mathrm{nm}$ [130], the density of photo-induced free charge carriers in the excited surface layer of the sample is approximately $n_{\mathrm{e,pump}} = 4.0 \cdot 10^{21}\mathrm{cm}^{-3}$ for the typical threshold pump fluence of $\Phi = 10\,\mathrm{mJ\,cm}^{-2}$. Taking into account that we lose about 20 % pump intensity (see next section) due to reflection at the two interfaces of the diamond anvil, this value reduces to $n_{\mathrm{e,pump}} = 3.2 \cdot 10^{21}\mathrm{cm}^{-3}$.

For comparison, the density of vanadium dimers that equals half the number of electrons that can be photoexcited by our pump is $n_{\mathrm{V-V}} = 1.7 \cdot 10^{22}\mathrm{cm}^{-3}$ (calculated with the structural data of [56]). Thus, at a pump fluence $\Phi = 10\,\mathrm{mJ\,cm}^{-2}$ we excite about 10 % of the vanadium atoms. This is in the order of the reported threshold excitation density of 10 % of the V–V dimers [120, 130].

Now we estimate which carrier density $n_{\mathrm{e}}$ is needed to make the plasma frequency $\omega_{\mathrm{p}}$ equal to our probe signal frequency at $\lambda_{\mathrm{probe}} = 10\mathrm{\mu m}$. The plasma frequency is related to the density of charge carriers $n_{\mathrm{e}}$ and their effective mass $m = Mm_{\mathrm{e}}$ according to

$$\omega_{\mathrm{p}} = \sqrt{\frac{n_{\mathrm{e}} e^2}{\varepsilon_\infty \varepsilon_0 m_{\mathrm{e}} M}}, \tag{4.7}$$

with $e$ for the elementary charge, $\varepsilon_0$ as permittivity of free space and $\varepsilon_\infty$ as dielectric constant in the high frequency limit $\mathrm{Re}\{\varepsilon(\omega \to \infty)\}$. $M$ scales the charge carrier mass $m$ in units of the electron mass $m_\mathrm{e}$. For $M = 1$ and $\varepsilon_\infty \approx 10$ [97] we obtain $n_\mathrm{probe,plasma} = 1.1 \cdot 10^{20}\mathrm{cm}^{-3}$ from equation (4.7) as electron density that corresponds to a plasma frequency equalling our probe signal frequency. This is more than an order of magnitude below the observed densities of charge carriers excited by the pump $n_\mathrm{e,pump}$ needed to drive the ultrafast IMT and corresponds to less than 0.4 % of the electrons of the $\mathrm{d}_{||}$ band. These estimates are quite rough, since the electrons in a band might have a larger mass, such that more carriers are needed to achieve the same plasma frequency. However, as the critical carrier excitation density $n_\mathrm{e,pump}$ is distinctly larger than $n_\mathrm{probe,plasma}$, free charge carriers could play an important role in the pressure-induced increase of the linear reflectivity.

### 4.4.6 Discussion of the linear reflectivity behaviour

This section concerns the observed pressure-induced changes in linear reflectivity, see Fig. 4.8(d) or Fig. 4.11(c). Free charge carriers may not be the sole contributors to the observed pressure-induced changes in the linear reflectivity, however, the estimates in the previous section show that their impact possibly dominates. For better insight we simulate here the linear reflectivity as function of the density of free charge carriers.

Considering absorption at free charge carriers in the Drude model, the frequency dependence of the dielectric constant is given by

$$\varepsilon(\omega, \omega_\mathrm{p}) = \varepsilon_\infty \left(1 - \frac{\omega_\mathrm{p}^2}{\omega^2 + i\omega\omega_\mathrm{c}}\right), \tag{4.8}$$

where $\omega_\mathrm{c} = \frac{2\pi}{\tau}$ is a scattering rate. Assuming normal incidence and that the pressure-induced changes of the refractive index of the diamond anvils are negligible (see section 3.2), the reflectivity of our sample at the frequency $\omega$ is given by

$$R_\mathrm{sample}(p, \omega) = \left| \frac{\sqrt{\varepsilon(\omega, \omega_\mathrm{p}(p))} - n_\mathrm{diamond}}{\sqrt{\varepsilon(\omega, \omega_\mathrm{p}(p))} + n_\mathrm{diamond}} \right|^2 . \tag{4.9}$$

Inserting equations (4.7) and (4.8) into equation (4.9) allows us to estimate the linear reflectivity of our sample at the probe frequency as function of the pressure-dependent charge carrier density $n_\mathrm{e}$.

We have to point out that the linear reflection signal was measured by blocking the pump. With this we lose the restriction that we are only sensitive to the volume of spatial overlap of pump and probe at the sample's surface. It is likely that we also capture probe light reflected from the upper diamond surface. Taking this into consideration, we would understand $R_{\text{lin}}(p)$ as a sum of a pressure-independent linear reflectivity $R_{\text{diamond}}$ of the diamond and the pressure-dependent intrinsic linear reflectivity $R_{\text{sample}}$ of the sample,

$$R_{\text{lin}}(p) = R_{\text{diamond}} + R_{\text{sample}}(p). \tag{4.10}$$

This means that the relative change of the intrinsic linear reflectivity of the sample $R_{\text{sample}}(p)$ can be much higher than the observed relative change of $R_{\text{lin}}(p)$ as shown in Fig. 4.8(d) or Fig. 4.11(c).

Obviously, an additional term like $R_{\text{diamond}}$ is also present in prior work. With $n_{\text{diamond}} = 2.4$ [48], at ambient conditions the reflectivity of VO$_2$ mounted in a DAC should be about $R_{\text{sample}} = 2\,\%$ for perpendicular incidence, however, the values reported in literature are in the order of 5–9 % [29, 60, 63]. Owing to the very low reflectivity $R_{\text{sample}}$, other contributions are dominant despite the fact that people did special calibrations in order to minimize the deviation from $R_{\text{sample}}$.

In the worst case, in our experiment there would be an additional term $R_{\text{diamond}} = \left|\frac{1-n_{\text{diamond}}}{1+n_{\text{diamond}}}\right|^2$ of about 17 %. This would correspond to an underestimation of the pressure-induced changes of $R_{\text{sample}}$ by a factor of 10. However, in our case we expect a smaller error than this. As the upper diamond surface is not in the focus, its reflection will not be collimated and we lose a part of the intensity on the way to the MCT detector.

Combining equations (4.7) to (4.10), we calculate the linear reflectivity $R_{\text{lin}}(p)$ as function of the pressure-dependent density of free charge carriers $n_{\text{e}}$ assuming $M = 1$ and assuming the scattering rate to be $\omega_{\text{c}} = 2\pi \cdot 90\,\text{THz}$ [142]. In Fig. 4.12 we show the results for $R_{\text{diamond}} = 17\,\%$ (blue trace) and considering literature [29, 60, 63] for $R_{\text{diamond}} = 5\,\%$ (red trace).

The onset of the measured linear reflectivity (see Fig. 4.8(d)) agrees qualitatively well to the shape of the simulated traces with its gradual increase starting at the plasma frequency, if we assume that the carrier density grows with increasing pressure. The simulation confirms that it is possible to obtain a doubling of the linear reflection $R_{\text{lin}}$, as observed in the experiment (see Fig. 4.8(d)). The carrier density needed for such a doubling is still well below the the densities of charge carriers excited by the pump $n_{\text{e,pump}}$ needed to drive the ultrafast IMT (see section 4.4.5).

However, it is hard to draw further conclusions from the simulation, especially on the pump-probe signal amplitude. Pumping with the typical pump fluence of $10\,\text{mJ}\,\text{cm}^{-2}$ increases the free charge carrier density at the surface of the sample in the order of $10^{21}\,\text{cm}^{-3}$. Considering such a jump along the carrier density axis in Fig. 4.12 and the corresponding jump in reflectivity, it is not possible to explain the distinct decrease of

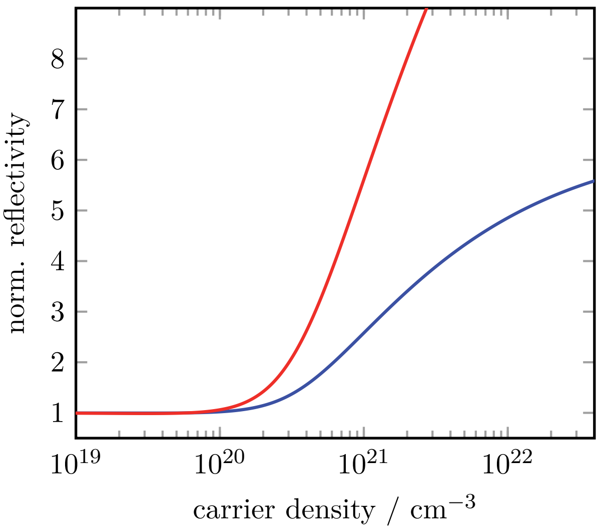

Figure 4.12: Simulated normalized linear reflectivity $R_{\text{lin}}$ for our probe at $\lambda_{\text{probe}} = 10\,\mu\text{m}$ ($\omega_{\text{probe}} = 2\pi \cdot 30\,\text{THz}$) as function of the density of free charge carriers. The simulation is based on equations (4.7) to (4.10), the normalization is relative to the linear reflectivity value at lowest carrier density (where the plasma frequency is much smaller than our probe frequency). The blue trace corresponds to $R_{\text{diamond}} = 17\,\%$, the red trace to $R_{\text{diamond}} = 5\,\%$.

the pump-probe amplitude at our highest pressures. This might be a consequence of an unrealistically high scattering rate $\omega_{\text{c}}$ which was taken from the metallic rutile-type phase. Possibly, for the equilibrium phase and the transient phase two different curves have to be considered. In conclusion, we cannot completely explain the pump-probe signal based on this simplified model. Nevertheless, it is not excluded that a more realistic model could explain the significant decrease of the pump-probe signal at our highest pressures.

Now we consider the impact of the difference between the observed ($R_{\text{lin}}$) and the intrinsic ($R_{\text{sample}}$) linear reflection of the sample on the relative pump-probe signal ($\Delta R/R$) and derived key parameters. The replacement of $R_{\text{lin}}(p)$ in equation (4.1) by the more realistic $R_{\text{sample}}(p)$ would lead to a higher calculated relative pump-probe amplitude. As $R_{\text{sample}}(p)$ grows with pressure, the correction of the calculated pump-probe signal would be smaller for higher pressures. Thus, the decrease of the pump-probe signal with increasing pressure beyond $p_{\text{c}}$ would be more pronounced (see Fig. 4.10). This would reduce the $m_1$ slope, however, the threshold values $\Phi_{\text{th}}$ would not be affected at all, as the fitted data points would all be scaled with the same correction factor. Overall, the observed anomaly at $p_{\text{c}}$ (see Fig. 4.8) persists independent of the replacement of $R_{\text{lin}}(p)$ by $R_{\text{sample}}(p)$.

Finally, we consider two special aspects about the pressure-induced linear reflection, on the one hand the saturation behaviour, on the other hand the role of thermal carrier activation.

In literature, saturation of the linear reflection is reported for pressures above 37–43 GPa [60, 63]. Therefore, it is surprising that we observe a constant linear reflection already for pressures above 16 GPa in one of the measurement series (black trace in Fig. 4.11(c)). In principle, such saturation could be expected when the scattering rate $\omega_\mathrm{c}$ is sufficiently low and the carrier density high enough to drive the plasma frequency beyond the frequency of the probe signal, or when a all carriers of the d-shell form a metallic conduction band. Both scenarios are not likely to apply to our measurements, since the pump-probe signal did not disappear with increasing pressure. Obviously, pumping creates additional charge carriers giving rise to an increased reflectivity. Since for a different measurement series (blue trace in Fig. 4.11(c)) no saturation of the linear reflectivity is observed, the saturation behaviour of the black trace might be related to the fact that in the first measurement series (black trace) the pressure was not increased monotonously, but released from 8 GPa to 4 GPa during the compression cycle.

The observed pressure-induced increase in reflection cannot be explained by thermal activation over the band gap, as shown below. The density of thermally activated charge carriers $n_\mathrm{thermal}$ can be estimated by the mass action law for semiconductors

$$n_\mathrm{thermal} = 2\left(\frac{k_\mathrm{B}T}{2\pi\hbar^2}\right)^{\frac{3}{2}} (m_e^* m_h^*)^{\frac{3}{4}}\, e^{-\frac{E_g}{2k_\mathrm{B}T}} = \sqrt{N_e N_h}\; e^{-\frac{E_g}{2k_\mathrm{B}T}}, \tag{4.11}$$

where $m_\mathrm{e}^*$ and $m_\mathrm{h}^*$ represent the effective masses and $N_\mathrm{e}$ and $N_\mathrm{h}$ the densities of electrons and holes, respectively. Equation (4.11) is derived by integrating the density of states of parabolic bands weighted with the Fermi distribution at finite temperatures. Assuming that all our carriers have the free electron mass $m_\mathrm{e}$, we obtain an intrinsic carrier density of $N_\mathrm{e} = 2.5 \cdot 10^{19}\,\mathrm{cm}^{-3}$ at a temperature $T = 300\,\mathrm{K}$. The thermally activated density of free charge carriers would be even reduced by the Boltzmann factor $e^{-\frac{E_\mathrm{g}}{2k_\mathrm{B}T}}$ in equation (4.11). As $n_\mathrm{thermal} < N_\mathrm{e}$ and $N_\mathrm{e} < n_\mathrm{probe,plasma}$, it is immediately clear that even across an arbitrary small band gap the thermal activation cannot provide sufficient charge carriers to lift the plasma frequency beyond the value corresponding to our probe frequency at $\lambda_\mathrm{probe} = 10\,\mu\mathrm{m}$. Therefore one has to assume the presence of partially filled delocalized electronic states within the energy gap in order to explain the pressure-induced increase of the mid-infrared reflectivity.

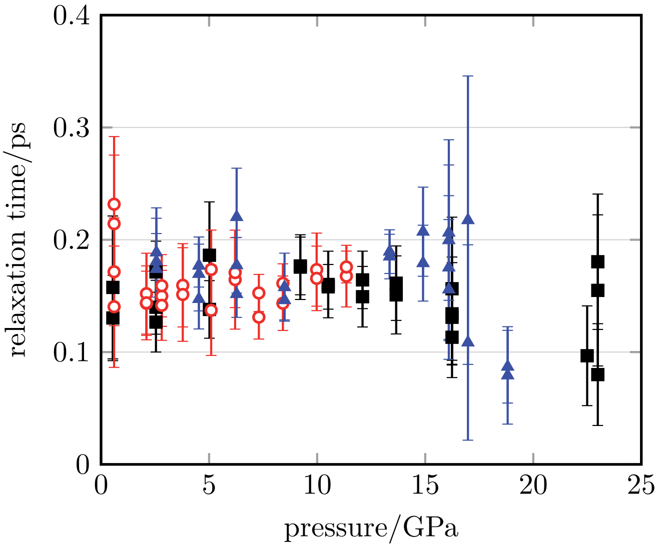

Figure 4.13: Fitted relaxation time constants for pump-probe traces corresponding to pump fluences within an interval of 5 mJ/cm$^2$ below the threshold fluence as function of pressure. The colour code corresponds to the three different samples shown in Fig. 4.8.

### 4.4.7 Relaxation dynamics

In order to study the relaxation dynamics of the fast (electronic) decay in the pump-probe traces, the pump-probe signal was fitted in the interval of the first picosecond with a mono-exponential function including an offset. Fig. 4.13 shows the time constants corresponding to pump fluences within an interval of 5 mJ/cm$^2$ below the threshold $\Phi_{\mathrm{th}}(p)$ as a function of pressure. There is no clear dependence on the fluence. The relaxation time constants scatter mainly around 0.15–0.20 ps in the whole pressure range. The slight drop of the time constants at higher pressures may be an artefact caused by a decreased signal-to-noise ratio, since the pump-probe amplitude gets very low at high pressures. The observed relaxation time scale matches with prior work [19].

According to Kübler *et al.* and Mayer *et al.*, a near-infrared pump photon generates an exciton locally on a V–V dimer that stays neutral [19, 132]. The fast relaxation is then due to excitonic self-trapping [132], it can only be connected to relaxation into the $\mathrm{d}_{||}$ band. The observation of a constant relaxation time at excitation levels below the threshold fluence indicates that the fast decay mechanism neither disappears nor changes under pressure. That the fast relaxation is independent of pressure while the slope $m_1$ changes under pressure is a strong hint that different states or decay channels are involved.

In comparison to the notable changes of other parameters, the observed pressure-independent relaxation time constant of the photoexcited charge carriers in $VO_2$ is remarkable. Maybe the dependence is too weak to be detected in our data. For the quasi-one-dimensional organic system ET-$F_2$TCNQ, a decrease of the relaxation time under compression was observed and even explained with a theoretical model [17]. There, a constant Coulomb repulsion $U$ was assumed, and an increasing hopping amplitude $t$ (proportional to the bandwidth $W$) and inter-site repulsion energy $V$ from nearest neighbours under pressure increase was derived [17]. However, these parameters are about an order of magnitude smaller than in the case of $VO_2$ [82], which might be the reason why we cannot observe a significant decrease of the relaxation time in $VO_2$.

## 4.5 Discussion

### 4.5.1 Band gap filling scenario

Combining our observations, it is possible to draw some conclusions about the band structure of $VO_2$ under pressure. Before presenting a tentative band scheme that can explain our results, we sum up the main points.

In the whole pressure range the band gap is still open, otherwise a saturation of the reflection, a vanishing of the threshold and of the pump probe signal, or – as demonstrated for the metallic rutile-type R phase – a slightly negative pump-probe signal would be expected. From the relaxation dynamics and its irreversible changes under decompression we conclude that the slope $m_1$ of the low-fluence asymptote is connected with the introduction of new states that do not disappear on pressure release. The growing reflection with pressure increase could be explained by a rising number of free charge carriers. The fact that the reflectivity still recovers under decompression means that the new states that withstand pressure release are no longer occupied or do not have delocalized character at low pressure. The lowering of the transmissivity at pressures below $p_c$ in combination with the pressure-independent reflectivity indicates an increased absorption in the sample which again could be a consequence of additional states.

These observations point towards band gap filling scenarios. In Fig. 4.14 the development of a tentative band scheme during compression is shown that could explain our observations. As in the band schemes of Fig. 4.6, the distribution of the density of states (DOS) is very roughly sketched on horizontal energy axes and the DOS coloured grey refers to filled states.

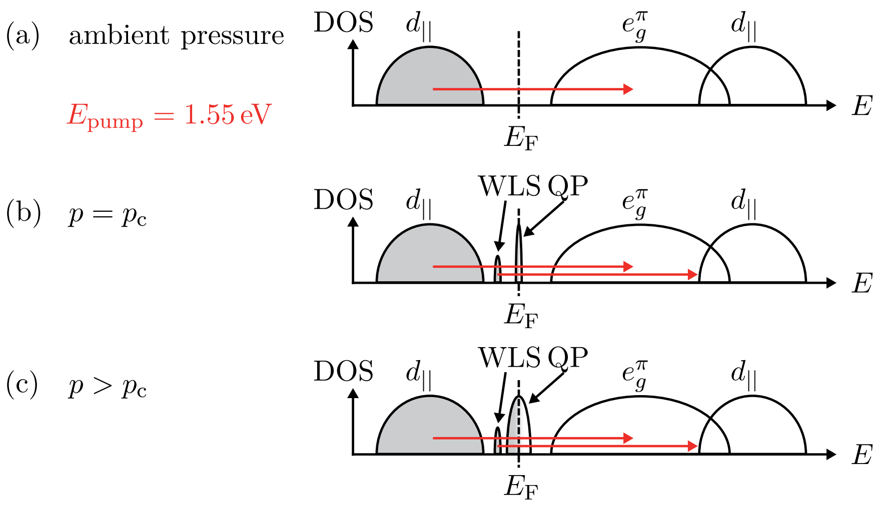

Figure 4.14: (a) Known band structure of monoclinic M1 phase, (b) and (c) tentative schematic band diagrams for $VO_2$ under compression with weakly localized states (WLS) and quasiparticle peak (QP). The red arrows correspond to pump excitation that increases the number of free charge carriers.

First we recall the band structure of the monoclinic M1 phase at ambient conditions in Fig. 4.14(a), as it has been presented in Figs. 4.3(b) and 4.6(b). For the probe photons of 0.12 eV the sample is transparent, we have high transmission. With our pump photons of 1.55 eV, electrons can be excited from the $\mathrm{d}_{||}$ band to the $e_g^{\pi}$ band.

Our suggestion for the band scheme under pressure assumes that above the critical pressure $p > p_\mathrm{c}$ spectral weight transfers to a partially filled, narrow band intra-gap quasiparticle peak (QP) containing delocalized quasiparticle states. A part of this spectral weight could be transferred to a low-energy satellite which we call weakly localized states (WLS). Our data do not allow us to decide the relative distribution of the DOS between the QP and the WLS, since not only the QP, but also WLS with binding energy smaller than the probe photon energy can contribute to the increase of the mid-infrared reflectivity. The onset of a finite slope of the low-fluence asymptote $m_1$ could be related to pump excitation of carriers from the WLS to free states. While for the localized states of the lower Hubbard band $\mathrm{d}_{||}$ the photoexcitation to metastable long-lived states is only possible *cooperatively*, which requires exceeding a pump threshold, from the WLS *non-cooperative* photoexcitation to such states is possible, *i. e.* without a threshold. As the QP at its onset is very narrow, the charge carrier mass will be very high. In such a situation, pumping of free charge carriers out of the QP to states with lower mass could also lead to increased reflectivity. At further elevated pressures, the QP and/or the WLS gain more spectral weight (see Fig. 4.14(c)) leading to the observed increase of the linear reflectivity (Fig. 4.8(d)). In parallel, the pump-probe signal $\Delta R/R$ and the slope $m_1$ decrease since the photo-induced relative change in the density of free charge carriers decreases for a given pump fluence. Finally, the QP and the WLS might merge leading to the vanishing of $m_1$.

Our experiments are consistent with a preservation of the dimerized monoclinic structure under pressure. Therefore the electronic system is supposed to play a major role for pressure-induced changes in $VO_2$. The simplest scenario in this case is a bandwidth-driven Mott-Hubbard phase transition, see section 2.2. The Hubbard model predicts that an increasing portion of spectral weight is transferred from the lower and upper Hubbard bands to a QP at the Fermi level when the effective correlation $U/t$ drops below a critical value [12, 143]. The Hubbard bands persist and finally merge with the broad QP in the limit of weak correlations. In our experiment the application of pressure improves the overlap between the orbitals leading to an increased hopping $t$ and hence to a decreasing effective correlation. The band gap still was present at our highest pressure, indicating that we just observed the onset and growing of the QP at pressures above $p_\mathrm{c}$.

While the Hubbard model can explain the appearance of the QP, the introduction of WLS is not covered. One explanation for the appearance of the WLS could be lattice defects in the $VO_2$ crystal. The initially delocalized electrons in the narrow QP have a high electron mass and therefore could be localized and bound to lattice defects. With increasing pressure leading to a broadening of the QP, the carrier mass should decrease. As a consequence the binding energy of the WLS might decrease so much that the states can be thermally ionized and the WLS merge with the QP. Another explanation for the WLS may be that they are an intrinsic feature of a more realistic Hubbard model. However, even recent material specific simulations of $VO_2$ only confirm the dominant role of the Mott mechanism for the IMT, but do not predict intra-gap states [111, 144]. Thus, the defect-related origin of the WLS appears to be more probable. Indeed, DMFT results by Weber *et al.* demonstrate that oxygen vacancies can induce localized intra-gap states in monoclinic $VO_2$ [108].

In addition, defects would remain after decompression, and thus could explain why $m_1$ does not reduce on pressure release. That $m_1$ even grows during decompression (see Fig. 4.11(b)) can directly be explained by the recovery of the linear reflectivity (see Fig. 4.11(c)), since at a low level of reflectivity the pump-induced changes become more pronounced. Considering our tentative band diagram, the decreasing reflectivity under decompression indicates that the spectral weight in the QP is lowered remarkably. This also would mean that the increase in reflectivity under compression is mainly due to the appearance of free charge carriers in the QP. Finally, defects could also explain why the transmission does not recover under decompression.

Under conditions when classical methods like photoemission cannot be applied in order to resolve details of the band structure, our pump-probe approach enabled us to get an indirect insight. The proposed band structure is tentative, the exact energy width of peaks cannot be evaluated without tuning the spectrum. We will now demonstrate that our results and the proposed band diagram are consistent with prior results reported in literature and discuss conditions that might affect our results.

### 4.5.2 Comparison of the proposed scenario with prior experimental studies

Our linear reflectivity and transmissivity data agree well with literature [29, 60, 63], see Fig. 4.8, but the observed critical pressure $p_\mathrm{c} \approx 7\,\mathrm{GPa}$ is distinctly lower in comparison to literature. Here we will discuss what can cause differences of $p_\mathrm{c}$ and what actually happens at this pressure. Finally, we focus on the band filling scenario and compare with the results of complementary measurement techniques.

The pressure medium CsI is known to be quasi-hydrostatic and may cause the observation of critical pressure values lowered by several GPa and by more than 20 % [140, 141]. Taking the work of Mitrano *et al.* as a reference, who used helium as pressure transmitting medium which minimizes deviation from hydrostatic conditions, the critical pressure for the structural transition from M1 to M1′ is around 12 GPa [59]. Therefore it appears possible that our critical pressure describes the same transition, albeit at lower apparent pressure. Critical pressures $p_\mathrm{c} < 12\,\mathrm{GPa}$ reported in literature [29] might as well follow from the use of a solid pressure transmitting medium as needed for reflection measurements [35], while on the other hand the pressure needed to reach the phase transition can also be higher when nanoparticle samples are used [60]. In conclusion, for our experiment a critical pressure $p_\mathrm{c} < 12\,\mathrm{GPa}$ can be expected, and it is resonable to connect the M1 to M1′ transition with the anomaly observed around 7 GPa.

Although such variations are an intrinsic problem for high-pressure measurements, which becomes quite obvious when comparing the pressure ranges for the coexistence regime as reported in the literature review at the introduction of this chapter (section 4.1), we shall have a closer look into this. Due to the large dimensions with edge lengths of about 80–100 µm it is likely that the observed lateral pressure inhomogeneity in the gasket hole filled with CsI (see section 3.1) will cause pressure gradients in our samples. In such a situation, our probe spot that typically had a FWHM diameter of 35 µm (in case of the first measurement series this diameter was 50 µm) would have averaged the response of an ensemble of slightly different pressures. This for example will broaden features like the drop of the fluence threshold $\Phi_{\mathrm{th}}$ at the critical pressure $p_{\mathrm{c}}$, see Fig. 4.8.

Another special form of pressure inhomogeneity is uniaxial pressure. Compressive strain along the $c_{\mathrm{R}}$ respectively the $a_{\mathrm{M1}}$ direction reduces the critical temperature $T_{\mathrm{c}}$ for the transition from the insulating monoclinic M1 to the metallic rutile-type R phase [69, 73, 145]. A slight uniaxial compression of 2 GPa reduces $T_{\mathrm{c}}$ by more than 20 K [69, 73, 145]. This effect is much stronger than the reduction of $T_{\mathrm{c}}$ at the boundary of the M1′ and the O phase, where for a comparable decrease of $T_{\mathrm{c}}$ the hydrostatic pressure has to be increased by 10 GPa [64]. In our case, the $c_{\mathrm{R}}$ or $a_{\mathrm{M1}}$ crystal axis was oriented parallel to the culet. The pressure inhomogeneity mentioned might act like uniaxial compression in the direction of this axis. On the one hand this mechanism may affect the critical pressure $p_{\mathrm{c}}$, on the other hand a reduction of $T_{\mathrm{c}}$ should lead to a smaller threshold fluence $\Phi_{\mathrm{th}}$.

This brings us to the discussion of the origin of the threshold drop around the critical pressure $p_{\mathrm{c}}$. The reduction of the energy barrier between the equilibrium and the transient photoexcited phase of $VO_2$ can be related to structural aspects, as well as an electronic reconfiguration, as will be discussed below.

At ambient conditions it has been reported that the threshold fluence matches the thermodynamic energy difference between the insulating monoclinic M1 and the metallic rutile-type R phase [120].

The enthalpies of M1 and M1′ are practically identical at $T = 0\,\mathrm{K}$ [64]. From this point of view, the pressure-induced isostructural transition from M1 to M1′ at the critical pressure $p_{\mathrm{c}}$ is not expected to lead to a drastic change of the threshold for the ultrafast IMT. However, as can be seen in the schematic phase diagram in Fig. 4.2, above the critical pressure $p_{\mathrm{c}}$ we have to suppose that the ultrafast IMT switches not to the rutile-type R phase, but to the O phase. According to Chen *et al.* [64], the enthalpy of the O phase is slightly smaller than that of the R phase, and always larger than that of M1 or M1′. The thermodynamic energy difference between the O phase and the M1′ phase depends on the temperature difference to $T_{\mathrm{c}}(p)$ and the latent heat. The latter is roughly 10 % smaller than for the M1 to R transition [64]. This and the decrease of $T_{\mathrm{c}}$ under pressure increase for the phase boundary between the M1′ and O phase [64] could explain a decrease in the threshold.

Besides the structural contributions on the development of the threshold, also the electron system can play an important role. The spectral weight transfer to the QP improves the screening of Coulomb interactions. Thus, the appearance of the intra-gap states and the corresponding depletion of the lower Hubbard band could not only be the sign of weaker correlations but also contribute to the reduction of the threshold fluence $\Phi_{\mathrm{th}}$.

The impact of the electron system might be even dominant. For example, Hsieh *et al.* reported that photoexcitation can induce a transient monoclinic metallic phase [18] at room temperature. In such case the threshold would not correspond to a critical density of phonons, but only to a critical density of electrons [121]. Cocker *et al.* had observed such Mott melting, the purely electronic switching to a metallic phase, only for temperatures below 180 K [121]. Here it is important to note that they performed their experiments in vacuum. When the sample is mounted in a DAC, the excited surface will be efficiently cooled by the diamond anvil, and the temperature increase induced by pumping is lower than when the sample surface is exposed to a vacuum. Thus, Mott melting might be even observed at an equilibrium temperature above 180 K. As our pump photons had only half the energy in comparison to the experiments of Hsieh *et al.* [18] in our measurements a Mott melting regime could appear more pronounced.

Finally, we emphasize that the proposed band scheme of Fig. 4.14 is compatible with both, lattice and electronic, mechanisms contributing to the anomaly in the threshold fluence.

In the following we compare our picture with prior experimental results reported in literature. Recent dc-resistivity measurements [64, 137] demonstrated a thermally activated character of the conductivity below $T_{\mathrm{c}}$ for pressures up to 20 GPa. This result is consistent with our proposed band scheme, since the resistivity behaviour only shows that a band gap exists. In the study of Chen *et al.* [64], the rising resistivity upon cooling can be interpreted to follow from a decreasing number of thermally activated charge carriers. However, free electrons in the QP could also contribute to the conductivity. With a QP centered at the Fermi level, its occupation would be almost temperature-independent. This leads to an overall conductivity

$$\sigma = \sigma_0 \mathrm{e}^{-\frac{E_{\mathrm{g}}}{2k_{\mathrm{B}}T}} + \sigma_{\mathrm{QP}}, \tag{4.12}$$

with the first term for the thermally activated part and $\sigma_{\mathrm{QP}}$ for the temperature-independent contribution of the quasiparticle peak. The corresponding resistance would be

$$\rho(T) = \frac{1}{\sigma_{\mathrm{QP}} + \sigma_0 e^{\frac{-E_{\mathrm{g}}}{2k_{\mathrm{B}}T}}}. \tag{4.13}$$

Because of their relatively small number and high effective mass it is possible that the contribution of the QP to the conductivity is only visible at low temperatures. When only measuring above room temperature like Chen *et al.* [64], the resistivity signal might

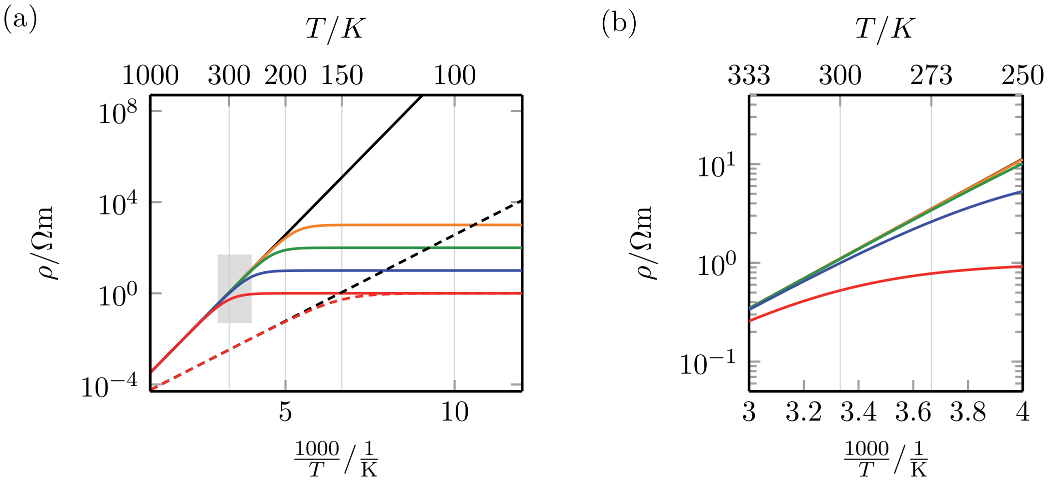

Figure 4.15: Simulation of the resistivity $\rho$ as function of the inverse temperature $\frac{1}{T}$ for different conductivity contribution from a quasiparticle peak $\sigma_{\mathrm{QP}}$ according to equation (4.13). On the upper horizontal axis, the temperature $T$ is shown. The simulations use a uniform $\sigma_0$. Solid traces were obtained with a band gap energy $E_{\mathrm{g}} = 0.6\,\mathrm{eV}$, dashed traces with $E_{\mathrm{g}} = 0.3\,\mathrm{eV}$. The black traces have a $\sigma_{\mathrm{QP}} = 0$, from orange via green and blue to red, $\sigma_{\mathrm{QP}}$ rises by three orders of magnitude. (b) is a magnification of the area shaded grey in (a).

be dominated by the thermally activated charge carriers and the contribution from the QP could be overlooked.

We demonstrate this in Fig. 4.15 by plotting the dc-resistivity $\rho$ as function of $\frac{1}{T}$ according to equation (4.13) for several values of $\sigma_{\mathrm{QP}}$ and a fixed $\sigma_0$. An increase of $\sigma_0$ (for example due to optimized contacts of crystal grains) would shift the whole plot to the right, *i. e.* to lower temperatures. For the solid traces, a band gap energy of 0.6 eV has been used and for the dashed 0.3 eV. For the black traces $\sigma_{\mathrm{QP}} = 0$, and therefore they do not saturate at low temperatures. All other traces have a finite $\sigma_{\mathrm{QP}}$. Actually, the red traces have the same finite $\sigma_{\mathrm{QP}}$, demonstrating that with a lower band gap energy, it becomes necessary to go to lower temperatures in order to be able to identify a possible contribution of $\sigma_{\mathrm{QP}}$. The same holds for fixed band gap energy and a lowered $\sigma_{\mathrm{QP}}$. For example, from the red to the orange trace, $\sigma_{\mathrm{QP}}$ decreases by three orders of magnitude, but only at low temperatures do the traces split, disclosing different contributions of $\sigma_{\mathrm{QP}}$. At a fixed temperature, $\sigma_{\mathrm{QP}}$ has to be sufficiently large in order to have an impact on the slope of the trace. For a band gap of 0.6 eV, the transition from maximum slope to minimum slope at a constant temperature spans over two orders of magnitude of $\sigma_{\mathrm{QP}}$, as can be seen in the enlarged view of Fig. 4.15(b).

According to this simple model, without checking the temperature dependence of the dc-resistivity at low temperatures, it is impossible to make any substantial conclusions which of the parameters, $E_g$, $\sigma_0$, or $\sigma_{QP}$ changes under pressure. The observed reduction in resistivity by one order of magnitude and the slight decrease of the slope of the temperature-dependent resistivity traces under pressure increase up to 20 GPa in the room temperature data of Chen *et al.* [64], could follow from an increase of $\sigma_0$ and a decrease of the band gap energy $E_g$. However, it is also possible that there is a finite $\sigma_{QP}$ that grows with increasing pressure and contributes to the reduction of the dc-resistivity. If there exists a QP with delocalized electronic states, the low-temperature resistivity will saturate. Recent high-pressure resistivity data of X. Zhang *et al.* [137] in the temperature range down to 90 K show the signature of such a behaviour. Thus, the dc-resistivity measurements available in literature do not contradict our proposed band scheme, but support it.

The same holds for the XANES study by Marini *et al.* [136]. Their data demonstrate only a slight spectral weight transfer. However, with an energy resolution in the order of the band gap energy they do not have the sensitivity to resolve the proposed intra-gap states.

Just as our reflectivity and transmissivity data fit to the results of Arcangeletti *et al.* [29], our tentative band scheme is also compatible with the frequency-dependent conductance that they derived from their results. As discussed in section 2.2, it is difficult to identify the contributions of intra-gap states to the conductivity spectrum. Indeed, Arcangeletti *et al.* [29] could only report that there appears band gap filling, but they could neither describe if it is due to band gap narrowing or intra-gap states, nor could they make a reliable conclusion about the persistence of the band gap or the conductivity at zero frequency.

Our proposed model for the insulator-to-metal is capable of describing dc-measurements, as we confirm the existence of the band gap in combination with band gap filling. Therefore this work can be a benchmark for future experimental studies as well as for theoretical modelling of $VO_2$ and strongly correlated electron systems in general.

## 4.6 Summary

Our NIR pump – MIR probe experiments on $VO_2$ under pressure give qualitatively new insight into the pressure-induced insulator-to-metal transition. With a wavelength of 10 µm, the used probe is ideal to detect free charge carriers since the photon energy is too low to excite electrons above the band gap of 0.6 eV at ambient pressure. The pump-probe approach allows to test, whether pumping at 1.55 eV can increase the number of free charge carriers.

Up to the highest pressures around 20 GPa, we observed a pump threshold for photo-induced switching to a metallic phase, which has been reproduced several times. This demonstrates that the band gap does not close under pressure. The relaxation time scale for excitation below threshold scattered around 0.15-0.20 ps, which matches literature values for ambient conditions, and did not show a clear pressure dependence.

On the other hand, at a critical pressure of about 7 GPa we observed an anomaly of several properties: a drop of the threshold fluence, the onset of a long-lived pump probe signal even at excitation below the threshold, the onset of an increase of the linear reflectivity, and a vanishing linear transmissivity. This change in behaviour can be explained by a pressure-driven band-filling scenario, as it is predicted in the DMFT solution [11, 12] of the Hubbard model for a bandwidth-driven insulator-to-metal transition. Thus, the rising linear reflectivity could be the consequence of a narrow quasiparticle peak at the Fermi level inside the band gap. This is further supported by the estimate of free charge carrier densities. The carrier density needed to lift the plasma frequency up to the level of the probe frequency is an order of magnitude below the pump-generated carrier density needed for the photo-induced IMT.

Under decompression, the linear reflectivity almost recovers, while the long-lived pump probe signal for pumping below the threshold does not return to the original values. This could be explained by the generation of pressure-induced defect states. In combination with a pressure-dependent Raman experiment, we conclude that the observed changes of the electronic structure are decoupled from a structural transition to the rutile-type phase of $VO_2$.

Overall, our data and interpretation is consistent with other experimental results on $VO_2$ reported in literature, including current dc-resistivity measurements. Our work gives valuable input for the improvement of the theoretical description of $VO_2$ and its pressure-induced IMT. For future experiments, it may be interesting to extend the pressure range, vary the pressure-transmitting medium and examine the properties of doped samples.

# 5 Ultrafast response of $Fe_2O_3$ under pressure

Iron oxides are among the most abundant compounds on and in the earth [146]. From early times mankind knew how to make use of these materials, first as pigments, later for example as precursor for iron and steel or as catalyst for chemical reactions [146]. Consequently there is broad interest in understanding the properties of these compounds.

Here we will focus on $Fe_2O_3$. Its most stable modification $\alpha$-$Fe_2O_3$ is also known as hematite [147]. This name originates from the ancient greek word αἷμα for blood and is related to the typical red colour of thin hematite layers as found in prehistoric paintings and well known from rust [146]. Today, hematite is attractive as an efficient photocatalyst for water splitting [147, 148]. In this field the understanding of the ultrafast carrier dynamics is essential which can be obtained by means of pump-probe techniques [148]. However, interest in hematite ranges beyond technological application and materials science. Thus, $Fe_2O_3$ is considered to play an important role in the inner earth oxygen cycle which demonstrates the importance of a better insight into this material for planetary and geological science [149–151]. Therefore hematite has been studied extensively under high pressure [150]. Besides a number of different structural and magnetic phases, a pressure-induced IMT was observed [151–153]. We will use pump-probe spectroscopy in order to obtain insight into the underlying mechanism of the IMT in a pressure range that corresponds to the earth's lower mantle conditions.

In section 5.1, a brief literature review on hematite is given. Section 5.2 addresses details of our experiment. The pump-probe results shown in section 5.3 will be discussed in section 5.4, which is followed by an outlook in section 5.5.

## 5.1 Introduction and motivation

### 5.1.1 Structural phases of $Fe_2O_3$

At ambient conditions two macroscopically existing polymorphs of the sesquioxide $Fe_2O_3$ are known: hematite ($\alpha$-$Fe_2O_3$) and maghemite ($\gamma$-$Fe_2O_3$) [147]. The $\beta$-$Fe_2O_3$ and $\varepsilon$-$Fe_2O_3$ modifications are stable only at the nanoscale [147]. Hematite crystallizes in the corundum structure (space group R$\bar{3}$c) [146]. This means that oxygen atoms are arranged in a slightly distorted hexagonal close packing and two thirds of the oxygen octahedra are regularly filled with $Fe^{3+}$ [154]. In contrast, maghemite ($\gamma$-$Fe_2O_3$) has a defect spinel structure (space group Fd$\bar{3}$m) [147]. In the cubic lattice both octahedrally and tetrahedrally coordinated $Fe^{3+}$ sites exist [146]. Besides by X-ray analysis, it is possible to distinguish between hematite and maghemite for example by means of Raman spectroscopy [155].

Here we will concentrate on hematite under pressure. In order to understand its electrical properties we will first have a closer look at the crystal structure of hematite before coming to phase transitions. Each oxygen octahedron surrounding $Fe^{3+}$ shares three edges with other octahedra in the same plane and one face with a second octahedron in a neighbouring plane [146]. Consequently, there are two lengths of Fe-O and Fe-Fe bonds [156] leading to a trigonal distortion of the octahedra [146]. While according to Rozenberg *et al.* [157] the distortion of the octahedra increases under pressure, the studies of Schouwink *et al.* [154] and especially the EXAFS studies of Sanson *et al.* [156] gave evidence that the octahedra are compressed nearly uniformly. Application of pressure leads to a slight decrease of the $c/a$ ratio [154, 157].

A pressure-induced phase transition discovered by shock wave and static compression experiments on hematite attracted many groups to contribute to the determination of $Fe_2O_3$ high-pressure structures [152, 153]. Here we will focus on the latest interpretation. The overview given by Bykova *et al.* [150] will be the basis for the following. As orientation, the tentative $p$–$T$ phase diagram shown in Fig. 5.1 presents the structural phases observed under compression in the pressure range up to 100 GPa and temperatures up to 1500 K.

At room temperature and a pressure around 50 GPa, when the volume is already decreased by about 17 % in comparison to ambient conditions, a structural transition from $\alpha$-$Fe_2O_3$ to $\zeta$-$Fe_2O_3$ appears [150]. This transition is accompanied by an additional drop of the volume by 8.4 % [150]. The crystal structure of $\zeta$-$Fe_2O_3$ had been assigned to a $GdFeO_3$-type orthorhombic perovskite (space group Pbnm) or a $Rh_2O_3$-II-type (space group Pbcn) [150, 156], only recently Bykova *et al.* figured out by single crystal diffraction studies that $\zeta$-$Fe_2O_3$ has triclinic symmetry (space group P$\bar{1}$) [150]. Due to insufficient data, a full refinement of $\zeta$-$Fe_2O_3$ in triclinic symmetry was not possible [150]. Instead, Bykova *et al.* describe the phase with a monoclinic cryolite-type double-perovskite structure (space group P$2_1$/n), also called *distorted perovskite*, and the general formula $A_2B'B''O_6$ [150, 159]. This structure consists of tilted corner-sharing octahedra around crystallographically different $B'$ and $B''$-sites and bicapped trigonal-prismatic A-sites for the Fe atoms [159]. Accordingly, the coordination number

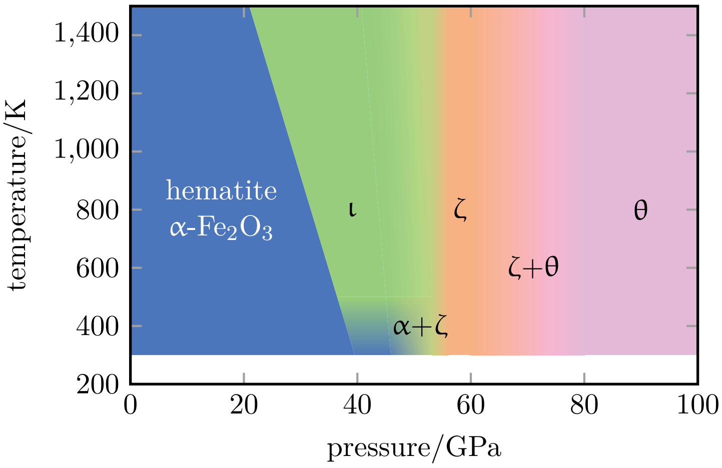

Figure 5.1: Schematic pressure–temperature phase diagram of $Fe_2O_3$ structures under compression. Adapted from [150] including data of [151, 158]. Shaded areas symbolize uncertainties of the phase boundaries. The sums indicate that phases have been observed coexisting in the sample volume of a DAC.

of B-sites is 6 and that of A-sites is 8 [159]. When pressure is increased, the structure becomes more symmetric, coming closer to the $GdFeO_3$-type perovskite [150]. The transition from hematite to the $\zeta$-$Fe_2O_3$ phase has been also observed in pressure-dependent Raman measurements [160].

At room temperature and a pressure around 67 GPa a structural transition occurs from $\zeta$-$Fe_2O_3$ to $\theta$-$Fe_2O_3$, an orthorhombic phase with space group Aba2 [150]. It is accompanied by a small drop of the unit cell volume by 1.7 % [150]. In the $\theta$-$Fe_2O_3$ phase, all Fe atoms are 6-fold coordinated [151]. Remarkably, in their EXAFS data Sanson *et al.* do not observe a signature of a phase transition in the pressure range above 55 GPa [156]. When $\theta$-$Fe_2O_3$ is heated beyond 1600 K, components with a $CaIrO_3$-post-perovskite-type structure (space group Cmcm), named $\eta$-$Fe_2O_3$ are observed [150]. Further high-temperature results described by Bykova *et al.* [150] are beyond the scope of this short review.

Finally, it should be mentioned that starting from hematite it is possible to thermally drive a phase transition into a $Rh_2O_3$-II-type structure of $Fe_2O_3$ [158, 161]. This phase, also assigned as $\iota$-$Fe_2O_3$ phase [150], separates the $\zeta$-$Fe_2O_3$ modification from $\alpha$-$Fe_2O_3$ as demonstrated by Ito *et al.* [158] in the temperature range from 1400 K down to 500 K, as schematically depicted in the $p$–$T$ phase diagram in Fig. 5.1. Extrapolating the phase boundary to room temperature results in a transition pressure of 39.7 GPa for a possible structural transition from hematite to $\iota$-$Fe_2O_3$ [158]. The observation of a pressure-induced transition from hematite to $\iota$-$Fe_2O_3$ at room temperature might be hidden because of slow reaction kinetics [158, 159].

### 5.1.2 Magnetic and electronic properties of $Fe_2O_3$ under pressure

At ambient conditions, hematite is a Mott insulator [152, 162] with ferromagnetic order within the planes of Fe atoms (111) and antiferromagnetic stacking of these sheets [163]. The Néel temperature is about $T_N = 960\,\mathrm{K}$ [163].

Hematite is well-known for the Morin transition [164], a spin flip by 90 degree with no change of crystal structure [163]. The transition occurs at ambient pressure when hematite is cooled below 250-260 K, leading to a drop of the magnetic susceptibility [163, 164]. The transition temperature increases when pressure is applied. At room temperature the Morin transition appears at a pressure of 1.5 GPa [163].

The magnetic and electronic properties of hematite and its high-pressure phases have been characterized by Mössbauer spectroscopy [150–152, 165, 166]. The Mössbauer spectrum of $\alpha$-$Fe_2O_3$ contains only a strongly split sextet and indicates that all iron atoms are $Fe^{3+}$ in a high-spin (HS) state [151]. With five electrons remaining in the d-shell, the iron atoms have $d^5$ configuration and consequently $S = \frac{5}{2}$ (see section 2.2).

At the onset of the distorted perovskite phase $\zeta$-$Fe_2O_3$, besides the 6 peaks of the hematite phase a doublet and another sextet appear in Mössbauer spectra [150]. The two new features have equal weight, demonstrating that in the new phase one half of the Fe atoms enter a non-magnetic phase [150]. According to Bykova *et al.* [150] and Greenberg *et al.* [151] the oxidation state of all Fe atoms remains +3 in the $\zeta$-$Fe_2O_3$ phase. Consequently the pressure-induced additional sextet in the Mössbauer spectrum corresponds to $Fe^{3+}$ sites in HS state with $S = \frac{5}{2}$, while the other $Fe^{3+}$ sites of the $\zeta$-$Fe_2O_3$ phase are considered to be in the low-spin (LS) state [150, 151]. That also for LS states with finite $S = \frac{1}{2}$ and even at low temperature only a non-magnetic signature, *i. e.* a quadrupole, but no hyperfine splitting, is observed at the Mössbauer experiment, indicates an itinerant character of the carriers of the LS sites [151]. Under further compression, first the weight of hematite disappears in the Mössbauer spectra, and finally the weight of the non-magnetic signature starts to dominate [150, 151]. In the $\theta$-$Fe_2O_3$ phase, only a doublet is observed, the spin-transition from HS to LS is completed [150, 152].

The coexistence of LS and HS sites in $\zeta$-$Fe_2O_3$ can be related to its distorted perovskite structure. DFT+DMFT calculations by Greenberg *et al.* predict that $Fe^{3+}$ ions at A-sites are in the HS state and at B-sites in the LS state [151]. The HS–LS transition accompanying the structural transition from hematite to $\zeta$-$Fe_2O_3$ can explain the significant volume decrease since it is known that the volume of an ion in the LS state is smaller than in the HS state [12, 150, 156]. In general, switching of one ion to LS decreases the total energy of the system and can stabilize surrounding HS ions, thus giving a hint why there exists a phase with coexistence of HS and LS states [12, 151].

In dc-resistivity measurements [151, 152] a decrease of the resistance by 6 orders of magnitude is observed when pressure is increased from 35 to 60 GPa. The resistivity curve measured by Greenberg *et al.* [151] has a kink around 40 GPa which interrupts the decrease of the resistance. The main decrease of the resistance happens above 50 GPa in agreement with Pasternak *et al.* [152]. Metallization is completed when the $\theta$-$Fe_2O_3$ phase is reached, which agrees with the Mössbauer data [151]. In temperature dependent dc-resistivity data, a pressure-induced switching from a clear semiconducting behaviour, *i. e.* decreasing resistance with increasing temperature, to a better conducting phase with weak temperature dependence of the resistance has been observed for pressures between 42 and 48 GPa [152]. At a pressure of 59 GPa the resistance increases when the temperature is increased, which indicates metallic behaviour [152]. A minimum of the resistivity in the temperature-dependent resistivity trace at low temperature might be explained by Kondo physics or electronic correlation effects [151].

Remarkably, under decompression Greenberg *et al.* observe an increase of the resistance and saturation within the $\zeta$-$Fe_2O_3$ phase accompanied by a volume increase of about 7 % [151]. This behaviour is interpreted as an isostructural site-selective Mott transition to a Mott insulating state, since the metal-to-insulator transition is related to the spin-transition of the structural subset of 6-fold coordinated $Fe^{3+}$ sites in the absence of any structural transition [151]. The important role of the spin configuration is in line with the considerations that for compounds with $d^5$ configuration $U_{\mathrm{eff}}$ in the LS state is much smaller than in the HS state (see section 2.2).

The band structure of hematite and its high-pressure phase has been studied via XAS [167, 168], X-ray photoelectron spectroscopy [167, 169], linear optical spectroscopy [162, 170], ultrafast pump-probe spectroscopy [171–173] and theoretical simulations [151, 174, 175].

In Fig. 5.2 the band scheme of hematite at ambient pressure is sketched. The density of states (DOS) plotted here in vertical direction is in reality much more complicated [151, 167–169]. At ambient pressure, hematite has a band gap of about $E_{\mathrm{gap}} \approx 2.1\,\mathrm{eV}$ which is obvious from absorption measurements and causes the characteristic red colour [146, 162, 173]. Considering their $d^5$ configuration and their octahedral oxygen surrounding for all Fe atoms in the $\alpha$-$Fe_2O_3$ phase, the lowest unoccupied states are the antibonding $t_{2g}$ and $e_g$ bands, which can be understood by ligand field theory [12]. From the distance of the peaks in an XAS spectrum it can be concluded that the crystal field splitting $\Delta_{\mathrm{cf}}$ between the $t_{2g}$ and $e_g$ band is about 1.4 eV at ambient conditions [168]. As shown in Fig. 5.2, the energy difference between the bottom of the $t_{2g}$ to the top of the $e_g$ band is about $\Delta E \approx 2.3\,\mathrm{eV}$, which Sorenson *et al.* extracted from photo-induced optical absorption measurements [173]. The trigonal distortion of the oxygen

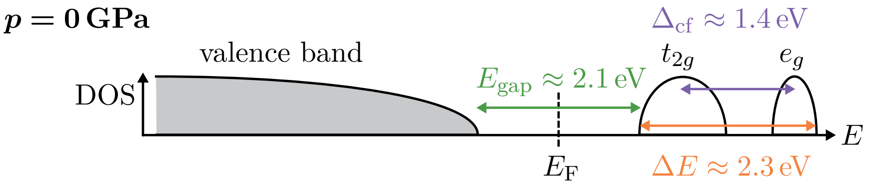

Figure 5.2: Schematic band structure of $Fe_2O_3$ at ambient conditions. Occupied states are coloured grey. The values for the band gap energy $E_{\mathrm{gap}}$, the crystal field splitting energy $\Delta_{\mathrm{cf}}$ and the energy difference $\Delta E$ between the bottom of the $t_{2g}$ and the top of the $e_g$ band are taken from [168, 173].

octahedra leads to a negligible further splitting of the $t_{2g}$ states into two low-energy $e_g^\pi$ orbitals and an $a_{1g}$ orbital by about 0.2 eV [174].

XAS experiments reveal the qualitative splitting into $t_{2g}$ and $e_g$ bands at least up to a pressure of 48 GPa [168]. The absence of a third peak demonstrates that the trigonal distortions remain low. This confirms also the aforementioned results [156] of structural analysis which indicate uniform compression of the octahedra. According to the XAS data at 48 GPa the crystal field splitting energy $\Delta_{\mathrm{cf}}$ is about 1.85 eV [168]. With this crystal field splitting and assuming a Hund's coupling energy of $J = 0.86\,\mathrm{eV}$ [151] which, in contrast to the crystal field splitting, is essentially independent of the applied pressure [12], we can evaluate the simple criterion for the HS–LS transition $\Delta_{\mathrm{cf}} > 3J$ [12] (see section 2.2). Since the crystal field splitting is far too low to fulfill the criterion, in the $\alpha$-$Fe_2O_3$ phase no transition to LS can be expected. Thus, the estimate agrees with the Mössbauer results which did not give any hint for a HS to LS transition in hematite under pressure. At a pressure of 56 GPa, in the $\zeta$-$Fe_2O_3$ phase, the XAS spectrum broadens and the two-peak structure disappears [168]. Considering that in the $\zeta$-$Fe_2O_3$ phase the Fe sites have different coordination, such changes in the XAS spectrum are not surprising.

According to DFT+DMFT calculations of Kuneš *et al.* [175] and Greenberg *et al.* [151], the band gap energy decreases under pressure. The signature of this behaviour is observed by absorption spectroscopy [170].

As mentioned above, the band structure of hematite has also been studied by pump-probe spectroscopy [171–173, 176]. Pump pulses centered around a wavelength of 400 nm (photon energy 3.1 eV) have been used, allowing the excitation of electrons from the valence band to the $t_{2g}$ band. The majority of studies focus on transient absorption [171–173, 176], there are much less data available about transient reflection [172, 173]. The pump-probe signal scales linearly with the fluence [173]. Sorenson *et al.* [173]

systematically discussed possible probe interactions like photo-induced absorption and bleaching after photoexcitation of charge carriers to the $t_{2g}$ band. This enables them to determine the energy difference between the bottom of the $t_{2g}$ and the top of the $e_g$ band, for example.

The pump-probe experiments revealed relaxation time scales of about 0.3 ps and 3–5 ps [172, 173]. In addition, relaxation on a time scale of several hundred picoseconds is reported [172, 173]. The fast time scale is interpreted as cooling, the others are both considered to correspond to recombination, trapping or recombination of trapped photo-induced charge carriers [172, 173]. Joly *et al.* [172] report the observation of coherent acoustic phonons at 68 GHz which corresponds to a cycle duration of 15 ps. Form this they determine the sound velocity in crystalline hematite to be about $6 \cdot 10^3$ m/s.

Remarkably, recent optical pump – XUV probe experiments [177–180] demonstrated that excitation with a pump around 400 nm leads to charge transfer from O 2*p* to Fe 3*d*-orbitals, but not Fe *d*–*d* transitions. Considering a $d^6$ configuration of Fe sites caused by this transient photoexcitation, the conditions for the HS–LS would be changed (see section 2.2) and pumping might strongly modify $U_{\mathrm{eff}}$, especially in combination with the pressure-controlled crystal field splitting energy.

Overall, for a full understanding of the electronic transition under compression further data are needed giving insight into the electronic configuration. How does the band gap close under pressure and what is the driving mechanism for the IMT? What is the impact of pressure on the ultrafast dynamics of charge carriers? How does the ultrafast response change across the pressure-induced metallization? These are questions we address with the first pump-probe measurements on $Fe_2O_3$ under pressure.

## 5.2 Experimental details

Single crystal $\alpha$-$Fe_2O_3$ samples have been provided by the group of Leonid Dubrovinsky at Bayerisches Geoinstitut. The crystals had been obtained by slow oxidation of pure iron at high temperatures [150, 154]. Their edge length is about 10 to 20 µm. In Fig. 5.3(a) an exemplary Raman spectrum of such a hematite crystal measured under ambient conditions is shown. For comparison, a Raman spectrum of $\alpha$-$Fe_2O_3$ reported in literature [160] is plotted in Fig. 5.3(b). Our observed phonon frequencies perfectly agree with literature. There is no Raman signature present of maghemite ($\gamma$-$Fe_2O_3$) [155, 181].

For our pump-probe measurements, large samples with flat and parallel surfaces (at least on two opposing sides) have been selected. Since the available hematite crystals

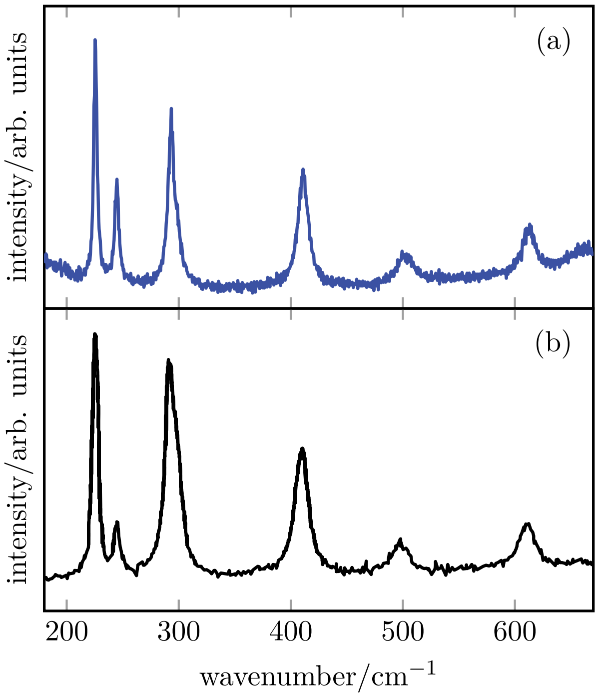

Figure 5.3: (a) Raman spectrum of $\alpha$-$Fe_2O_3$ at ambient pressure captured at one of our sample crystals, (b) Raman spectrum of hematite at ambient pressure taken from [160].

are tiny, samples have been always mounted in a DAC for pump-probe measurements, even at ambient pressure, in order to ensure good cooling.

The optical pump – NIR probe measurements on $\alpha$-$Fe_2O_3$ were performed with a slight adaption of the set-up shown in Fig. 3.6. Simultaneously to the signal measured in reflection, the pump induced change of the transmission was captured with a second photodiode and lock-in amplifier. The pump spot with a FWHM in the order of 35–40 µm was clearly larger than the hematite sample crystal with edge lengths between 10 and 20 µm. The probe was focused to a FWHM of 7–11 µm, ensuring that the main part of the probe light hits the sample when the set-up is well aligned and a large sample crystal is chosen. After tuning the pressure of the DAC, the focus position of the DAC was found by the crossing point of two alignment lasers on the gasket and the correct lateral position was found as local minimum of the linear transmission signal.

The pump-probe traces are affected by an offset. Blocking the probe centered at 800 nm did not have an impact on the finite pump-probe amplitude at negative delay time. This gives evidence that despite low-pass filters installed in front of the photodiodes, the offset is caused by the pump light centered at 400 nm. In the following the offset is subtracted in all plots.

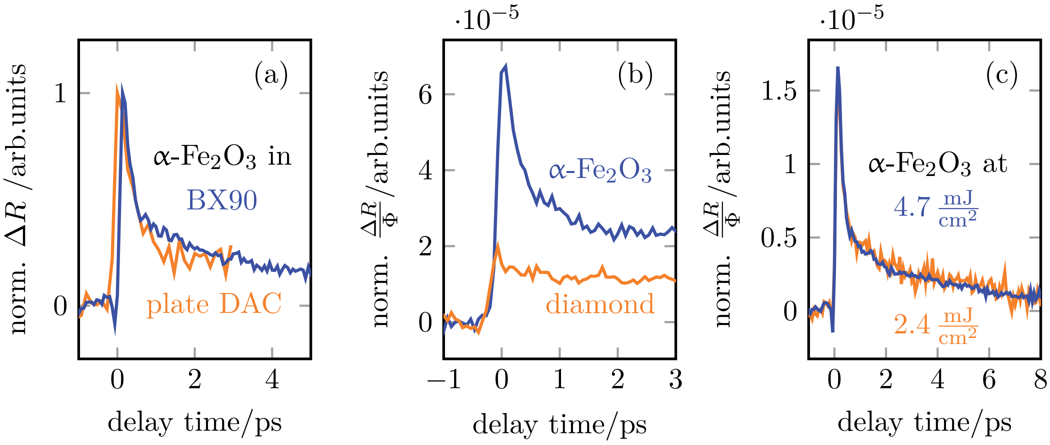

Figure 5.4: (a) Comparison of normalized pump-probe traces obtained from hematite mounted in a BX90 DAC (blue line) or in a plate DAC (orange). (b) Comparison of pump-probe traces measured on hematite (blue) mounted in the plate DAC and on the diamonds (orange) of the empty plate DAC, normalized to the fluence. (c) Pump-probe traces obtained on hematite at 17 GPa in the BX90 for two different pump fluences normalized to the fluence.

The pump-probe response in reflection obtained from hematite under low pressure in a DAC agrees well with prior work at ambient pressure reported in literature [173]. A fast decay on the time scale of a few hundred femtoseconds is followed by a relaxation on a picosecond time scale, see Fig. 5.4(a). Tests with our empty plate DAC showed that a finite pump-probe signal can also be obtained from the diamond anvils as shown in Fig. 5.4(b). This signal originates from impurities or defect states in the diamonds, further analysis is given in the appendix. We have to stress that we used type IIa diamonds, the diamonds with lowest concentration of optically active impurities. This means it is not avoidable that there might be a contribution from the diamonds to the pump-probe signal. However, in contrast to the pump-probe response of hematite, it is roughly step like, see Fig. 5.4(b). Thus, in first approximation, the observed relaxation dynamics should originate from hematite – when it is not distorted by the pressure transmitting medium. For example, the pressure transmitting medium KCl can be excited at 400 nm giving rise to a pump-probe signal that relaxes on a picosecond time scale, see appendix. For a filling with hematite surrounded by KCl we are still able to measure the signature of hematite in reflection geometry, which demonstrates the tight focus of the probe spot that is smaller than the cross section of a sample crystal.

In order to be able to apply sufficient pressure for the pressure-induced electronic transition, a BX90 DAC equipped with rhenium gasket was used for the experiments (see section 3.1). The pressure cell was loaded at the Bayerisches Geoinstitut. The gasket was preindented from the thickness of 200 µm to about 22 µm. In order to reduce the stress on the diamond anvils, preindentation was done in two steps. After partial preindentation, a gasket hole was cut which became smaller under further preindentation. Finally, when preindentation was finished, the hole was cut to final size. Neon was used as pressure-transmitting medium. After filling, the gasket hole diameter was about 80 µm and a pressure of 4.8 GPa was measured via ruby fluorescence. This means that the neon was solidified [44] and kept the sample in a fixed position.

As shown in Fig. 5.4(a), the pump-probe signal obtained from hematite in the BX90 and the plate DAC are consistent. The time scale of relaxation dynamics agrees with measurements performed on free standing samples reported in literature [171–173]. This demonstrates that our signal traces are not distorted by pressure transmitting media. In agreement with prior work [173] we observe that the pump-probe signal of $\alpha$-$Fe_2O_3$ scales linearly with the pump fluence, see Fig. 5.4(c).

## 5.3 Pump-probe results

In Fig. 5.5 the pump-probe response at a pump fluence of 4.7 mJ/cm$^2$ is shown for a series of pressures up to 60 GPa. Each trace is corrected for its pump offset and normalized to its absolute maximum. The blue traces mark the reflection signal, the grey correspond to the changes in transmission.

For pressures below 40 GPa we observe a pump-induced increase of reflection, followed by a sub-picosecond relaxation dynamics and a slower decrease on a picosecond time scale. In addition, a transient reduction of the transmission is observed. Its duration is comparable to the temporal resolution of the pump-probe scans, which is 66 fs. This is similar to the rise time of the pump-induced reflection signal. Remarkably, the dip in the transmission signal slightly precedes the onset of the reflection, see Figs. 5.5(a)-(d). The reflection signal reaches its maximum when the transmission change returns to zero. This temporal hierarchy is a reliable result since the reflection and transmission signal have been captured simultaneously using the same delayed probe pulse. The delay time zero was set to the delay stage position with the pump-induced minimum transmission at a pressure of 5 GPa. Exactly the same scale has been used for all other pump-probe traces shown in Fig. 5.5. With pressure increase up to 27 GPa the peak in the transmission signal at delay time zero becomes weaker on an absolute scale. In the normalized plots of Figs. 5.5(b) and 5.5(c) therefore the relative negative signal at positive delay times becomes more pronounced as well as does the noise level. However, the absolute negative pump-probe signal amplitude in transmission and its noise level at positive delay times are almost independent of pressure.

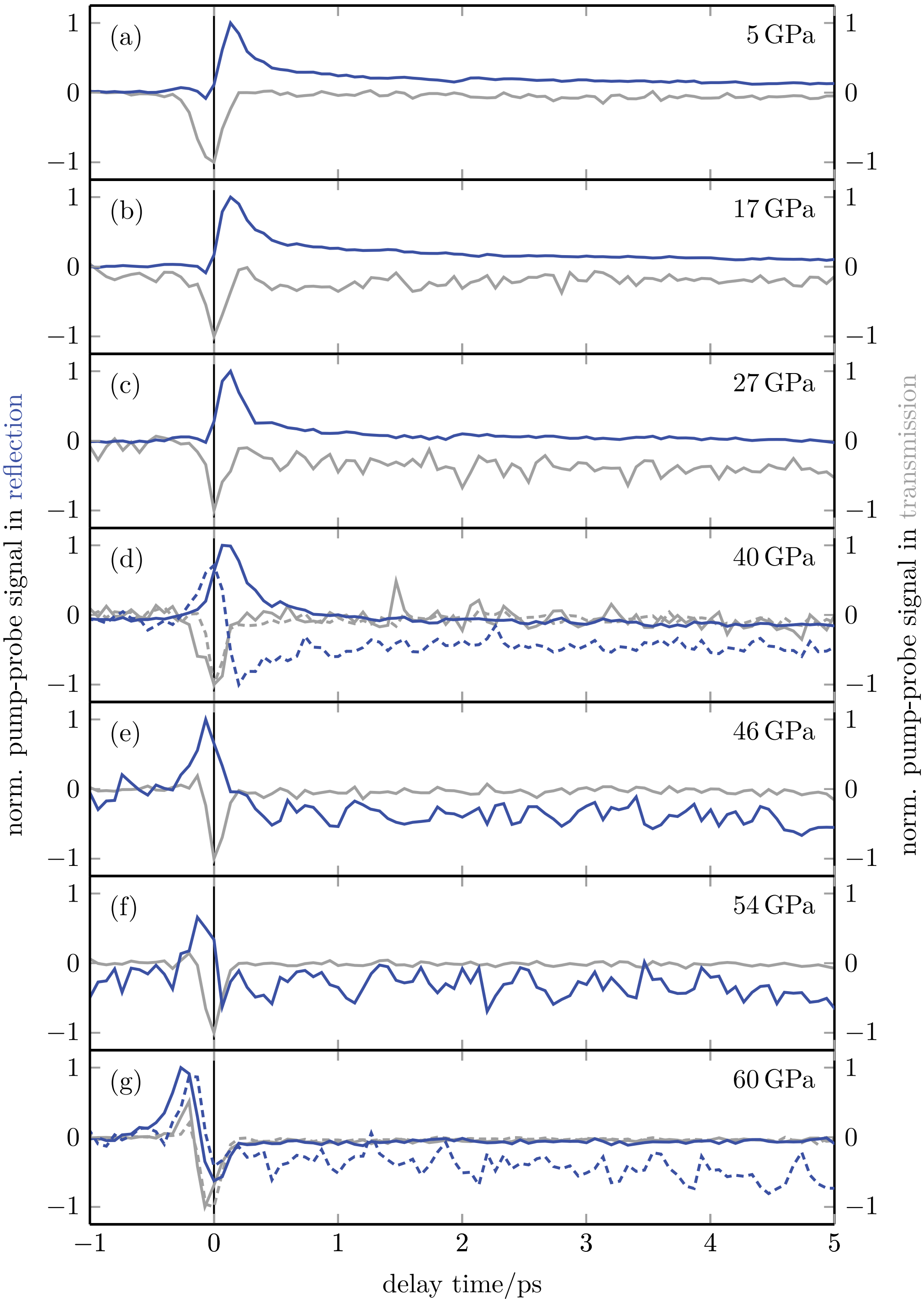

Figure 5.5: Normalized pump-probe results on $Fe_2O_3$ in reflection (blue) and transmission (grey) under pressure. (d) The dashed traces have been captured several minutes after the measurement of the solid traces. (g) The dashed traces have been captured immediately before the spatial pump-probe overlap has been realigned and the solid traces have been measured.

At a pressure of 40 GPa we observed qualitatively different pump-probe responses. In a first measurement we obtained a similar trace as at 27 GPa (compare blue solid lines in Figs. 5.5(c) and 5.5(d)). The dashed blue line (see Fig. 5.5(d)) was obtained in a reproduction test a few minutes later. Without any changes in the set-up, a drastically different pump-probe signal was observed in reflection. The reflectivity is increased only transiently around the zero delay time. Afterwards, a negative pump-induced change of the reflectivity is observed that recovers on a picosecond time scale and much slower. The transition point from positive to negative sign is at the delay stage position with the former maximum in the transient reflection signal. In transmission, the repetition of the measurement shows a slightly increased amplitude of the peak at delay time zero, while the absolute noise level does not change. This trend holds also under further compression.

With further pressure increase, the reflectivity signal became more noisy and the positive response in reflection appears to precede the ultrafast response in transmission, see Figs. 5.5(e)-(g). Finally, at a pressure of 60 GPa the spatial overlap of pump and probe was realigned for a reproduction test (solid traces in Fig. 5.5(g)) by slightly tuning the position of the pump spot with the last mirror in front of the DAC. It turned out that the pump-probe overlap had drifted. By re-alignment, the amplitude of the transient transmission signal could be increased by a factor of two. In addition the pump-offset in reflection geometry and with this also the noise level was drastically reduced. A small long-lasting negative pump-probe signal in reflection remained. The realignment of the pump-probe overlap comes along with a slight shift of delay time zero, see Fig. 5.5(g). The latter can be explained by the changed optical path length for the pump.

In order to clarify the pressure dependence of the pump-probe signal of $\alpha$-$Fe_2O_3$ a second measurement series was performed. Unfortunately, with the used BX90 a dominant pump-probe signal from the diamond anvils was detected which made it impossible to extract information on hematite, see appendix.

Thus, we concentrate here on the analysis of the data obtained for pressures up to 40 GPa. For better comparison, we show the corresponding normalized pump-probe traces in one plot in Fig. 5.6. At positive delay times above 2 ps all traces are parallel. Accordingly, bi-exponential fitting gives similar time constants for all traces. In Fig. 5.6 an exemplary fitting curve is shown for the data taken at 17 GPa. The time constants are about 0.20 ps and 3.5 ps. This is close to literature values for hematite at ambient conditions [171–173]. It is remarkable that during the relaxation, the pump-probe signal changes from positive to negative sign at the two higher pressures plotted in Fig. 5.6. Moreover, at negative delay times up to $-2$ ps, a negative pump-probe signal is observed.

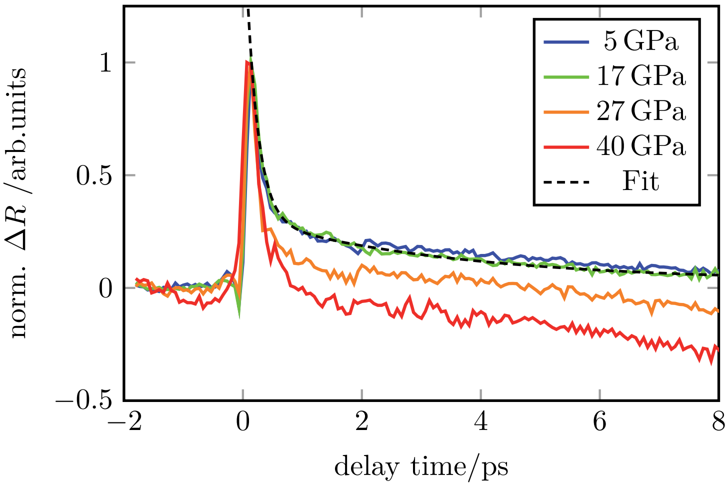

Figure 5.6: Normalized pump-probe signal received on $Fe_2O_3$ in reflection geometry. The dashed black line represents a bi-exponential fit on the pump-probe signal measured at a pressure of 17 GPa.

## 5.4 Discussion

### 5.4.1 Origin of the pump-probe response

First we will discuss the reflection signal considering the absorptions from the valence band to the $t_{2g}$ band and between the $t_{2g}$ and the $e_g$ band.

At low pressures, the ultrafast response in reflection agrees well with literature. The pump photons with 3.1 eV excite charge carriers into the $t_{2g}$ band as illustrated in Fig. 5.7(a). Immediately after photoexcitation the thermalized hot carriers will occupy states significantly above the bottom of the $t_{2g}$ band as depicted with the grey occupation in Fig. 5.7(b). These carriers can be further excited from the $t_{2g}$ to the $e_g$ band. Thus, pumping induces an absorption band, as depicted by the black solid trace in Fig. 5.8. Consequently, the real part of the refractive index (solid blue trace in Fig. 5.8) of $\alpha$-$Fe_2O_3$ is altered. Our probe with photon energy around 1.55 eV is below the absorption resonance [173] and the vicinity to the absorption resonance leads to a significant increase of the real part of the refractive index. At ambient pressure, the refractive index of hematite is around 2.6 [182, 183] which is above that of diamond that is about 2.4 [48]. Thus, the difference of the refractive indexes of $\alpha$-$Fe_2O_3$ and diamond is increased by pumping, which leads to an increased reflectivity for our probe pulses.

The fast relaxation appears on a time scale typical of carrier cooling [173, 184]. In Fig. 5.7(c) the band structure after the initial cooling of the photo-induced electrons is

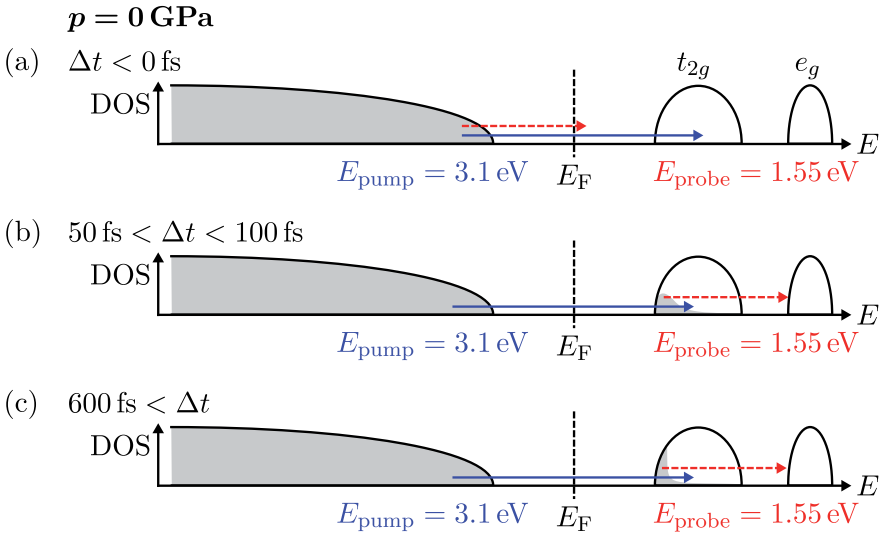

Figure 5.7: Schematic band structure of Fe$_2$O$_3$ at ambient pressure (a) in the ground state, (b) immediately after photoexcitation with pump-photons of 3.1 eV and thermalization of the photo-induced charge carriers, (c) after completion of sub-picosecond cooling dynamics. Occupied states are coloured grey. The blue arrows correspond to pump excitation, the length of the red arrows correspond to the probe photon energy. Solid arrows show how photons can be absorbed, while the dashed arrows only serve as guide for the eye to estimate how close the probe energy is to a resonance.

shown. In comparison to the situation immediately after thermalization, the bandwidth of the photo-induced absorption band is lowered through a shift of the low-energy absorption wing to higher energy. According to Sorenson *et al.*, at ambient pressure, the main weight of the long-time pump-induced absorption concentrates at 2.0–2.3 eV [173]. This corresponds to a shift of the absorption band away from the energy of our probe photons of 1.55 eV to higher energies. As shown by the dashed traces in Fig. 5.8 due to such a shift, the impact on the real part of the refractive index is decreased. Thus, the cooling of the photo-induced electrons in the $t_{2g}$ band can explain the fast decay of the pump-probe signal measured in reflection shown in Fig. 5.6.

When the probe is non-resonant, only transient pump-probe signals from $\chi^{(3)}$ can be expected in transmission. Such nonlinearities might be the reason for the negative peak at delay time zero preceding the response in reflection. That the transmission pump-probe signal almost vanishes at the moment of maximum reflection signal, indicates that even for the hot carrier distribution only few carriers are in states that allow the resonant absorption of probe photons. As mentioned above, the simultaneous measurement of

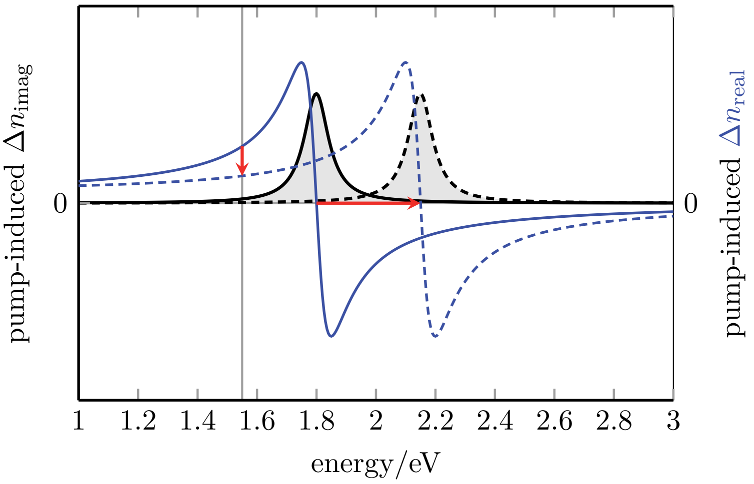

Figure 5.8: Schematic explanation of the impact of pump-induced changes of the imaginary part of the refractive index, here absorption bands (black traces), on the real part of the refractive index (blue traces). The red arrows from the solid to the dashed traces demonstrate how an upshift of the pump-induced absorption band modifies the pump-induced change of the real part of the refractive index. The vertical grey line marks our probe photon energy of 1.55 eV.

the reflection and transmission signals excludes that the transmission trace is time-shifted against the reflection trace. Therefore the negative amplitude at delay time zero cannot be due to probe-induced transitions from the $t_{2g}$ to the $e_g$ band. The small negative transmission amplitude at positive delay times might be due to absorption between different sub-bands of the broad valence band.

### 5.4.2 The band structure under pressure

With pressure increase, the crystal field splitting increases leading to a larger energy difference between the $t_{2g}$ and the $e_g$ bands. According to the XAS data of Wang *et al.* the crystal field splitting at 40 GPa is about 0.4 eV larger than at ambient pressure [168]. Consequently, the absorption band for the transitions of cooled charge carriers from the $t_{2g}$ to the $e_g$ band will shift to higher energies. In analogy to the effect described in Fig. 5.8, it can be expected that the pump-induced increase of the real part of the refractive index is weakened and therefore the reflectivity increase at the energy of our probe photons is lowered. While the increased crystal field splitting can explain the pressure-dependent decrease of the pump-probe amplitude in reflection after the initial cooling of photo-induced charge carriers, it cannot explain why the change between

5 and 17 GPa is much smaller than at higher pressure, see Fig. 5.6. Moreover, it is surprising that the pump-probe signal at longer delays changes sign at these elevated pressures.

A negative pump-probe amplitude in reflection could be caused by an absorption band at lower energy than the probe photon energy or by bleaching effects. The splitting of the $t_{2g}$ orbitals into $e_g^\pi$ and $a_{1g}$ orbitals caused by the trigonal deformation enables absorption at energies below our probe photon energy and this splitting might increase with pressure. However, the XAS data of Wang *et al.* [168] has no signature of such behaviour.

Bleaching could become important, when the band gap between the valence band and the $t_{2g}$ band gets smaller under pressure. The photo-induced charge carriers in the $t_{2g}$ band reduce the phase space available for absorption processes from the valence band to the $t_{2g}$ band. In principle, contributions of pump-induced bleaching and absorption to the real part of the refractive index exist in parallel. Which effect dominates at a certain energy, depends strongly on the density of states (DOS) of the corresponding initial and final states of the transitions [173]. At ambient pressure the higher DOS in the $t_{2g}$ and $e_g$ band can explain the dominance of the photo-induced absorption [173]. The situation at ambient pressure after the sub-picosecond cooling is depicted in Fig. 5.9(a). The band gap energy of 2.1 eV is comparable to the energy difference between the bottom of the $t_{2g}$ and the top of the $e_g$ band [173]. Therefore the total impact on the real part of the refractive index $\Delta n_{\mathrm{real}}$ (red line in Fig. 5.9(a)) corresponds to the appearance of a pump-induced absorption band.

In case of a decreasing band gap under high pressure, the pump-induced bleaching will shift to lower photon energies. Moreover, the pressure-induced increase of the crystal field splitting will shift the pump-induced absorption band to higher photon energies. As demonstrated in Fig. 5.9(b), it is then possible that the bleaching dominates the response at our probe photon energy and the real part of the refractive index is lowered by pumping. The situation of Fig. 5.9(b) would fit to the observed pump-induced decrease of reflectivity to negative values at a pressure of 27 GPa, see Fig. 5.6. This scenario cannot only explain the pump-induced decrease of reflectivity, but also that the change in reflection from 27 to 40 GPa is much larger than for the step from 5 to 17 GPa. The latter is due to the nonlinear increase of the impact of the bleaching band, when it shifts down to the probe photon energy. In analogy to the explanation how the application of pressure can change the sign of the long-lived pump-probe signal from positive to negative, it can be understood that the reflection pump-probe signal decreases during the ultrafast cooling. Immediately after excitation, before the cooling on the sub-picosecond time scale, the components of the pump-induced absorption

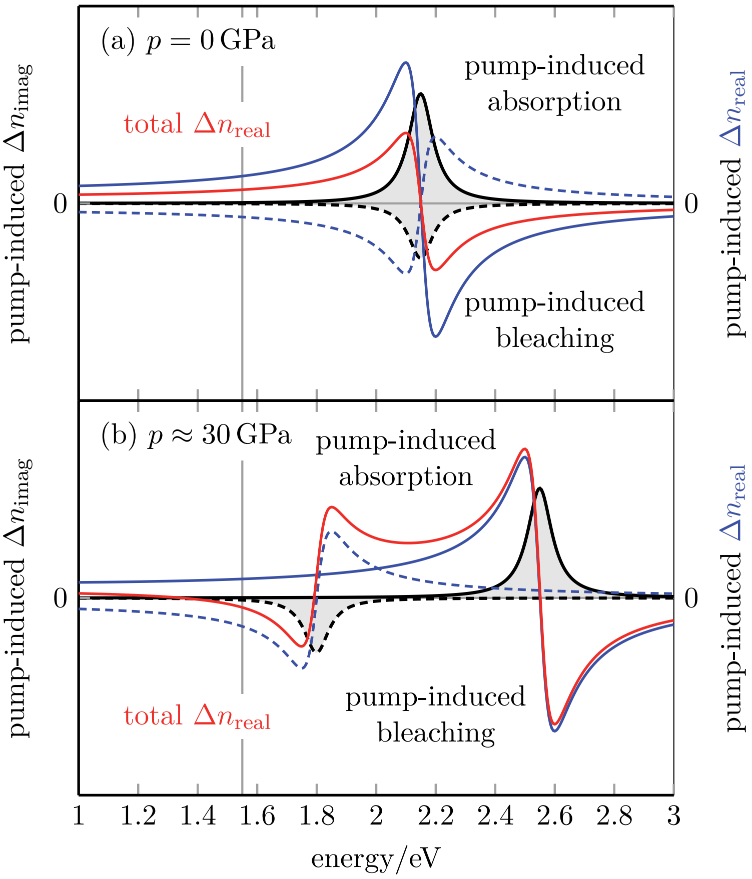

Figure 5.9: Schematic description of pump-induced changes of the imaginary and real part of the energy-dependent refractive index of $\alpha$-$Fe_2O_3$ after the initial electron cooling at (a) ambient pressure and (b) at elevated pressure in the order of 30 GPa. Pump-induced absorption bands are plotted as black solid lines, pump-induced bleaching bands with black dashed lines. The blue traces (solid and dashed) show corresponding impact on the real part of the refractive index. By summing the contribution of pump-induced absorption and bleaching the red traces are obtained. The probe photon energy of 1.55 eV is marked with a grey vertical line.

band will be at lower photon energies and components of the pump-induced bleaching at higher energies than in Fig. 5.9(b).

In Fig. 5.10 we summarize the changes in the band structure for the proposed scenario. The known band structure at ambient pressure is shown in Fig. 5.10(a). The probe photon energy (dashed red arrow) is far off resonance with the band gap and therefore bleaching has only a weak impact. At elevated pressure this can change as demonstrated with the dashed red arrow in Fig. 5.10(b) starting from the valence band. With the

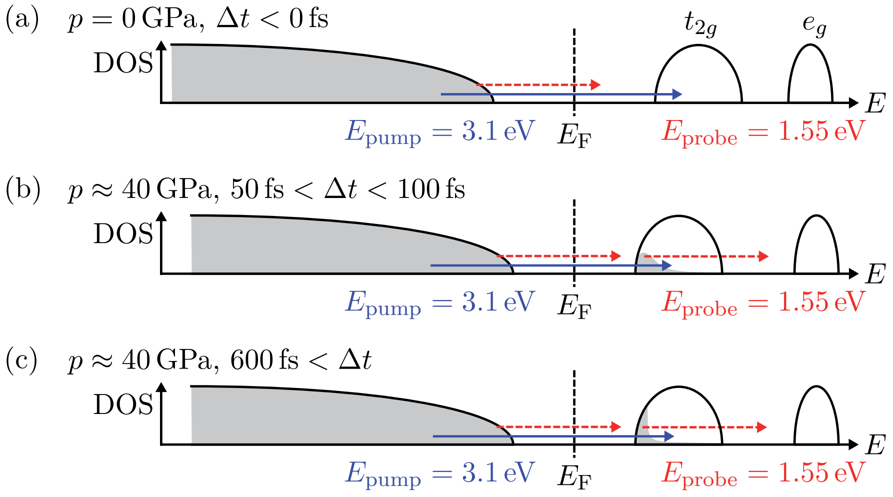

Figure 5.10: (a) Schematic band structure of $Fe_2O_3$ in the ground state at ambient pressure. (b) Tentative schematic band structure at a pressure around 40 GPa after photoexcitation with pump-photons of 3.1 eV and thermalization of the photo-induced charge carriers in the $t_{2g}$ band, (c) at a pressure around 40 GPa after completion of the sub-picosecond cooling dynamics of the photo-induced charge carriers. Occupied states are coloured grey. The blue arrows correspond to pump excitation, the length of the red arrows correspond to the probe photon energy. Solid arrows show how photons can be absorbed, while the dashed arrows only serve as guide to the eye in order to visualize how close the probe energy is to a resonance.

pressure-induced increase of the crystal field splitting, the probe becomes clearly non-resonant to the transition of photoexcited charge carriers from the $t_{2g}$ to the $e_g$ band, as depicted by the other red arrow. After completion of the cooling this effect is even stronger which can be understood from Fig. 5.10(c). While at elevated pressure the probe is closer to be resonant to the band gap and not to transitions from the $t_{2g}$ to the $e_g$ band, the opposite is the case at ambient pressure, as can be seen by comparison with Fig. 5.7(c).

The proposed moderate band gap shrinkage agrees to calculations of the band structure [151, 175] and the monotonous reduction of the dc-resistivity [151, 152] in this pressure range. The slight pressure-induced modifications of the transmission signal are consistent with the proposed band scheme where the probe is still non-resonant. The decrease of the amplitude at delay time zero could be explained by a pressure-induced decrease of the $\chi^{(3)}$ nonlinearity or deterioration of the phase matching conditions.

### 5.4.3 Slow relaxation dynamics

When photoexcited electrons recombine with holes, the pump-induced bleaching and absorption decrease. Remarkably, on the picosecond time scale we observe an increase of the absolute amplitude of the pump-probe signals at 27 and 40 GPa after they go negative, see Fig. 5.6. This observation gives clear evidence that this relaxation time scale is not related to recombination.

In contrast to literature [171–173] we consider the underlying relaxation as a slow cooling process. The effect of cooling on more than one time scale is well known from other materials [184, 185]. Perfetti *et al.* describe such behaviour with a 3-temperature model, the temperature of the electron system, the temperature of phonons that are well coupled to the electron system and phonons that are almost decoupled from the electrons [185]. Acoustic phonons belong to the latter group, while LO phonons are known to be strongly coupled to electrons in polar materials via the Fröhlich mechanism [184, 186]. The fast relaxation ends when the hot electrons have heated the well coupled part of the phonon spectrum so that they both are at the same temperature [185]. Afterwards, the temperature dynamics of the hot electrons and the hot phonons are similar and depend on the anharmonic decay of hot phonons and the electronic coupling with cold phonons [185].

The observed sub-picosecond time scale might be related to the emission of LO-phonons, which at ambient pressure are about 82 meV and at 40 GPa about 98 meV [160] in hematite. This energy (corresponding to a temperature around 1000 K) could explain that the main shift of pump-induced absorption and bleaching bands will be finished on the sub-picosecond time scale, but clearly recognizable cooling occurs afterwards.

### 5.4.4 Transition at 40 GPa

The qualitative difference between the solid and the dashed trace of the pump-probe response in Fig. 5.5(d) indicates a strong change in the electronic band structure. During the pump-probe experiment, the pressure in the BX90 increased by 0.3 GPa. Therefore, it is quite remarkable that we get an opposite picosecond relaxation behaviour.

That the negative pump-probe signal recovers to a long-lived negative value would be consistent with pump-induced heating of a metal, where hot carriers are less conducting and therefore the reflectivity decreases. This view is also supported by the fact that at even higher pressures always a slightly negative long-lived signal amplitude is observed. We recall that qualitatively the traces in reflection are quite similar for all pressures above 40 GPa. Even after the improvement of the pump-probe overlap there is a slightly negative pump-probe signal at positive delay time.

A suboptimal pump-probe overlap cannot explain the changes at 40 GPa in Fig. 5.5(d), since the pump-probe signal would have to change linearly proportional to the pump fluence incident on the sample. It can be excluded that the probe was not well aligned on the $Fe_2O_3$ sample. After each change of the pressure, the lateral DAC position was aligned according to the minimum in transmission and there always was a good contrast between the transmission of the $Fe_2O_3$ sample and just neon.

The dc-resistivity data of Greenberg *et al.* [151] and Pasternak *et al.* [152] indicate that the electronic band structure of hematite changes around a pressure of 40 GPa. Thus, in the data of Pasternak *et al.* the main decrease of resistivity starts at a pressure around 40 GPa. In the pressure-dependent resistance trace of Greenberg *et al.* [151] there is a kink around 40 GPa that seems to separate two pressure ranges of drastic resistivity decrease. The first drop by one order of magnitude occurs in the pressure range from 32 to 40 GPa, the main drop by four orders of magnitude from 44 to 60 GPa. According to the Mössbauer data of Greenberg *et al.* [151] the first drop of the resistance is completed before the transition to the distorted perovskite phase appears.

Ito *et al.* have mentioned that at room temperature there might be a structural phase transition from $\alpha$-$Fe_2O_3$ to $\iota$-$Fe_2O_3$ around a pressure of 39.7 GPa [158]. At ambient temperature the reaction kinetics might be slow, but heating can drive the phase transition [158]. At 500 K the hematite phase and the $\zeta$-$Fe_2O_3$ phase are clearly separated by the $\iota$-$Fe_2O_3$ phase [158], see Fig. 5.1. Thus, we will estimate the heating impact of our pump.

We consider that the pump energy is completely absorbed at the sample surface within the absorption length $d_{\mathrm{absorption}}$. The temperature difference $\Delta T$ in the pumped thin surface layer can then be calculated as

$$\Delta T = \frac{\Phi V_{\mathrm{s}}(p) N_{\mathrm{A}}}{5 C_{\mathrm{m}} d_{\mathrm{absorption}}}, \tag{5.1}$$

where $\Phi$ is the pump fluence, $V_{\mathrm{s}}(p)$ the pressure-dependent volume of a structural unit, $N_{\mathrm{A}}$ the Avogadro constant, and $C_{\mathrm{m}} = 3R$ the molar heat capacity defined by the gas constant $R$. The heat capacity of $Fe_2O_3$ is approximated by means of the Dulong-Petit law to $5C_{\mathrm{m}}$ which according to the data of Shim *et al.* [160] is close to the real value. The values of the absorption length that can be extracted from literature vary widely, ranging from about 20 nm [176] over 45 nm [162] to about 110 nm [173]. This uncertainty probably results from the use of very thin samples and the reflection corrections in the absorption measurements. With $V_{\mathrm{s}}(p = 40\,GPa) = 43.6\,\text{Å}^3$ [150], $d_{\mathrm{absorption}} = 20\,nm$ and the pump fluence $\Phi = 4.7\,\mathrm{mJ/cm^2}$ we obtain a transient temperature increase $\Delta T = 496\,\mathrm{K}$, induced by a single pump laser pulse in a 20 nm thin surface layer of the sample. For an absorption length of 45 nm, the temperature increase would be about 220 K, and for $d_{\mathrm{absorption}} = 110\,\mathrm{nm}$ only 90 K. These estimates show that in principle it might be possible by pumping to thermally switch the sample to the $\iota$-$Fe_2O_3$ phase. The heat will diffuse away into the diamond anvils and the volume of the $Fe_2O_3$ crystal, which is several hundred times thicker than its photoexcited surface layer. At a pressure of 40 GPa, it might be possible that the sample does not relax back to the hematite phase once it has been switched photo-assisted to the $\iota$-$Fe_2O_3$ phase. Such a phase-switching scenario might explain the observed qualitative changes of the pump-probe signal at 40 GPa. There is a lack of data about electronic properties of the $Rh_2O_3$-II-type $\iota$-$Fe_2O_3$. However, the $Rh_2O_3$-II-type structure had also been taken into consideration for the $\zeta$-$Fe_2O_3$ phase [161], where metallization is known to occur. The observations described above might be an indication that even a transition to the $\iota$-$Fe_2O_3$ phase can lead to improved conductance.

Finally, we estimate the pump-induced carrier density. Assuming that over an absorption lenght $d_{\mathrm{absorption}} = 20\,\mathrm{nm}$ all pump light is homogeneously absorbed, the pump-induced electron density would be $n_{\mathrm{e,pump}} = 4.7 \cdot 10^{21}\,\mathrm{cm}^{-3}$ at a fluence of $4.7\,\mathrm{mJ/cm}^2$. For $d_{\mathrm{absorption}} = 110\,\mathrm{nm}$ the density would be only $n_{\mathrm{e,pump}} = 8.6 \cdot 10^{20}\,\mathrm{cm}^{-3}$. For comparison, we calculate the density of free charge carriers in the metallic phase of $Fe_2O_3$. If we assume that five electrons of the Fe d-shell contribute to the conductivity, the free charge carrier density would be about $n_{\mathrm{e}} = 2.0 \cdot 10^{23}\,\mathrm{cm}^{-3}$. Here we calculated with a structural unit volume of $50.3\,\text{Å}^3$ [150] which corresponds to the situation at ambient pressure. At the pressure of 40 GPa the electron density should be about 15 % higher. Compared to the density of free electrons in the metallic phase, we photo-induce only roughly 0.4 % to 2.4 %. This relative value is lower than the critical density that we determined to be required for the ultrafast IMT in $VO_2$, while the absolute pump-induced carrier densities are comparable. Therefore a filling-controlled mechanism might be an alternative scenario for the induction of a more conducting phase in $Fe_2O_3$.

## 5.5 Summary and outlook

Our pump-probe study on hematite and its pressure-induced polymorphs have shown that the relaxation time scales of the transient response are essentially pressure-independent. The relaxation on a picosecond time scale is identified as cooling dynamics, not recombination. In the pressure range up to 40 GPa, the observed changes in the signal amplitude could be interpreted by changes in the pump-induced absorption and bleaching following an increase of the crystal field splitting and a decrease of the band gap energy. A qualitatively different response at 40 GPa indicates that at this pressure probably a phase transition appears. Possible explanations could be a thermally-driven transition or a transition driven by a critical photo carrier density.

In order to be able to draw more precise conclusions, further experiments will be necessary. First, it is desirable to test the reproducibility of the results. For this, it would be advisable to find a pair of diamonds with minimum pump-probe response before filling the BX90. At further pump-probe measurements, the fluence dependence of the response should be verified in the pressure range around 40 GPa. In order to find out whether pumping leads to a long-lasting phase transition, it would be useful to have a reference sample in the DAC which is not pumped. To meet this requirement, it may be also necessary to lower pressure or cool the DAC between the pump-probe scans. In addition, it would be interesting to determine the pressure-dependent changes of the band gap by means of linear spectroscopy.

# 6 Summary and conclusions

We have combined ultrafast pump-probe spectroscopy and diamond anvil cell (DAC) high-pressure technology in order to gain insight into the mechanism of the pressure-induced insulator-to-metal transition (IMT) of strongly correlated electron systems. The limits of the studied pressure range and the probe wavelength have been successfully advanced in comparison to previous studies: Optical pump – near-infrared (NIR) probe experiments have been carried out up to 60 GPa and NIR pump – mid-infrared probe experiments have been demonstrated up to 23 GPa, at a probe wavelength of 10 µm. In addition, successful pump-probe test measurements in a DAC with probe pulses centered at 30 µm and provided from the free electron laser FELBE at the HZDR have been demonstrated. The basis for the success of such experiments with a probe spot diameter almost in the order of the sample cross-section was the robust design of the whole set-up. A probe with large wavelength is desirable since it is sensitive to free charge carriers only.

Remarkable results have been obtained on the archetypal transition metal compound $VO_2$. They indicate a band gap filling scenario for the pressure-induced IMT. In the whole pressure range under study it was possible to photo-induce a transient metallic phase when the pump fluence exceeded a pressure-dependent threshold. Even at a pressure of 23 GPa a large pump-probe signal was observed, which demonstrates that up to this pressure the band gap does not close. However, above a critical pressure of 7 GPa the linear reflectivity starts to grow, which can be explained by the scenario of a bandwidth-driven Mott-Hubbard transition. Our interpretation is based on calculations published in literature that predict for the Hubbard model an evolution of the IMT over a three-peak structure, where the spectral weight of the two Hubbard bands is transferred to an inner gap quasiparticle peak which is populated with carriers of high effective mass [11]. Further anomalies, like a drop of the threshold fluence at the critical pressure, a vanishing transmissivity and the onset of a finite long-lived pump-probe signal even with an excitation below the threshold are compatible with this description. When pressure was released, the linear reflectivity recovered, while the long-lived pump-probe signal for photoexcitation below the threshold survived. This indicates non-reversible pressure-induced changes in the sample, probably defects. In a high-pressure Raman study no structural transition to the rutile-type phase was observed, hence we can conclude that the pressure-induced changes of the electronic structure of $VO_2$ are decoupled from the structural transition to the rutile-type phase. In the pressure range studied, the relaxation time scale of the photoexcited carriers was always around 0.15-0.20 ps, not showing a clear pressure dependence. Here, an extension of the pressure range could be interesting for the future, however, we had been limited by our DAC.

In order to achieve sufficiently high pressures necessary for the optical pump – NIR probe experiments on $\alpha$-$Fe_2O_3$, we used a BX90 DAC of the Bayerisches Geoinstitut. The time scales of relaxation after photoexcitation were found to be essentially pressure-independent. However, we observed changes of the pump-probe signal amplitude and sign under pressure which can be explained by pump-induced absorption and bleaching effects in combination with an increasing crystal field splitting. This change of the sign demonstrates that cooling of the electron system is the origin of the picosecond relaxation process. At a pressure of 40 GPa, the pump-probe response shows a sharp qualitative change, which indicates a rearrangement of the electronic band structure and might be a consequence of an IMT facilitated by optical pumping. A pump-probe signal was even obtained at 60 GPa. In order to be able to draw further conclusions, the experiment should be reproduced. At such an attempt with another BX90, unfortunately it turned out that the mounted diamond anvils absorb the 400 nm pump light giving rise to a quite dominant pump-probe response that scales linearly with the pump. The next step is to find a pair of diamonds that do not disturb the measurement. Further tests with our own DAC demonstrate that qualitatively different pump-probe signals can be obtained even when there is a small contribution of the diamond to the pump-probe signal.

In the course of this work, a highly robust alignment procedure for pump-probe measurements in a DAC has been developed. This allows the reproduction of measurements, as it has been demonstrated several times for $VO_2$. While there the DAC had to be always removed from the set-up in order to change the pressure, in the future the use of a membrane DAC will simplify the procedure. However, for the intended experiments at low temperatures, it can be expected that the DAC changes position slightly when the temperature is altered. Thus, the alignment procedure described in this work can be beneficial for such experiments.

Our pump-probe approach allows indirect insights into the pressure-dependent electronic band structures, when classical methods like angle-resolved photoemission spectroscopy cannot be applied for technical reasons. Thus, our results, especially on $VO_2$, can serve as benchmark for future experimental studies as well as the development of improved models for materials.

# Appendix: Additional pump-probe results on diamond and KCl

As described in section 5.2 we observed a finite pump-probe response from diamond when using a pump wavelength around 400 nm. In this appendix we show further data in order to demonstrate the qualitatively different character of the pump-probe signal from diamond and KCl, as well as their linear scaling with the pump fluence.

In Figs. App.1(a) and App.1(b) pump-probe results obtained in reflection geometry at the BX90 with absorbing diamonds are shown. After the focal position was aligned, the pump-probe response at a lateral position corresponding to $Fe_2O_3$ (blue trace) and neon (green) was captured. Similarly, after the DAC has been opened the response from diamond (orange) was measured at the empty BX90. The normalized plots of Fig. App.1(a) demonstrate that the response is independent of the lateral alignment. As shown in Fig. App.1(b), where the same pump-probe traces have been normalized to the pump fluence, from the empty cell a larger signal was obtained than from neon or hematite. These observation indicate a dominant pump-probe signal from the diamond anvils. Further analyses showed that this signal scales linearly with the fluence.

It has been excluded that the similar results obtained for different lateral positions of the BX90 are caused by an improper alignment of the focus. With the same alignment as it was used for the shown BX90 pump-probe results, it has been possible to resolve qualitative different signals from our plate DAC filled with a hematite crystal surrounded by KCl as pressure-transmitting medium. The response obtained from KCl is shown in Fig. App.1(c) for fluences of 2.4 (green trace) and 4.7 $\mathrm{mJ/cm^2}$ (orange). The pump-probe signal scales almost linearly. In contrast to the response of $Fe_2O_3$ (compare Fig. 5.4) no sub-picosecond relaxation is observed and the picosecond dynamics is faster.

In Fig. App.1(d) we further show results obtained on the empty plate DAC, *i. e.*, on diamond for different pump-fluences. The traces captured at 1.2 (blue trace), 2.4 (green) and 4.7 $\mathrm{mJ/cm^2}$ (orange) coincide when normalized to the fluence. This means that the pump-probe signal from the diamond anvils scales linearly with the pump fluence. Consequently it is not caused by two-photon absorption, but by single photon absorp-

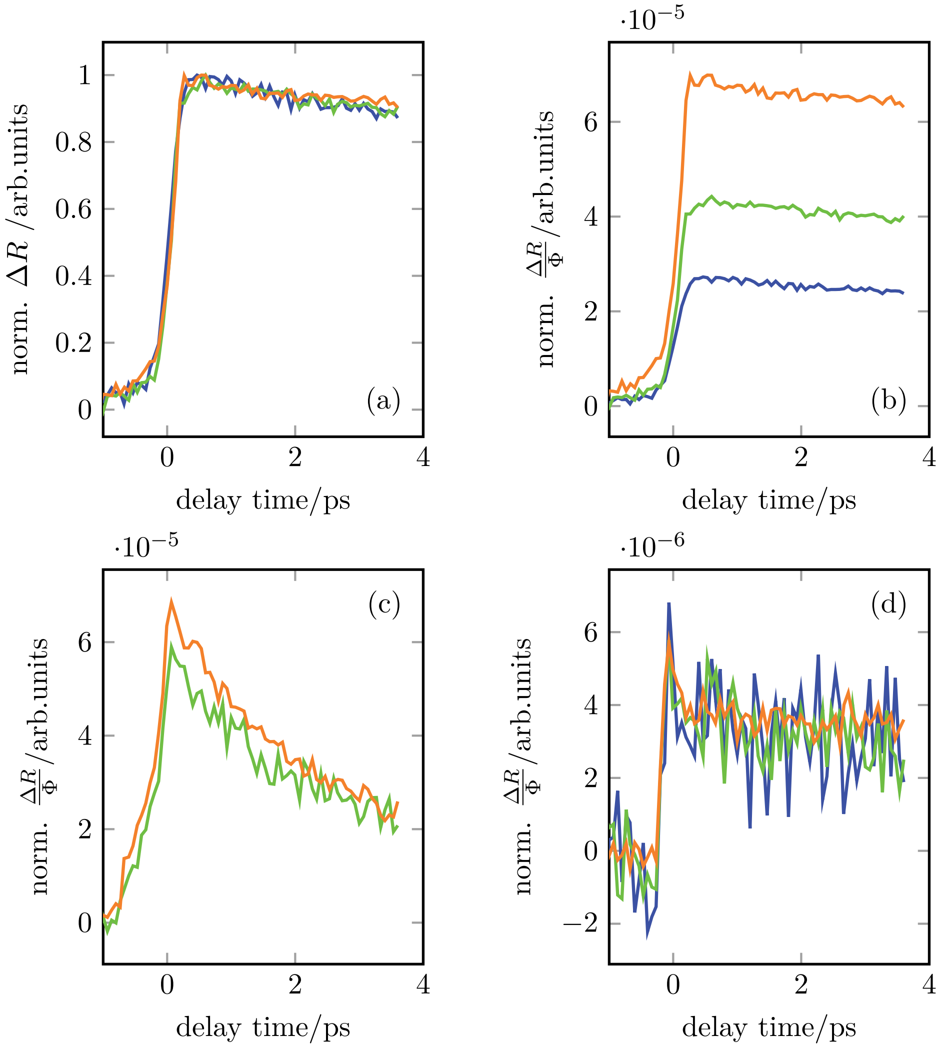

Figure App.1: (a) Normalized pump-probe signal of $Fe_2O_3$ (blue), neon (green) and diamond (orange) using the BX90 with absorptive diamond anvils and (b) the same pump-probe signals normalized to the fluence. (c) Pump-probe signal from KCl filled in the plate DAC normalized to the fluence. (d) Pump-probe signal of diamonds of empty plate DAC normalized to the fluence. (a)-(d) All traces have been corrected for an offset.

tion. Since diamond has a much larger band gap energy than the used pump-photon energy of 3.1 eV, the pump-probe signal originates from defect states or impurities.

# Bibliography

[1] H. G. Drickamer and C. W. Frank, ‘Electronic Structure, Electronic Transitions, and the High Pressure Chemistry and Physics of Solids’, Annu. Rev. Phys. Chem. **23**, 39–64 (1972).

[2] A. R. Goñi, K. Strössner, K. Syassen and M. Cardona, ‘Pressure dependence of direct and indirect optical absorption in GaAs’, Phys. Rev. B **36**, 1581–1587 (1987).

[3] D. Olego, M. Cardona and H. Müller, ‘Photoluminescence in heavily doped GaAs. II. Hydrostatic pressure dependence’, Phys. Rev. B **22**, 894–903 (1980).

[4] J. Schilling, N. Hillier and N. Foroozani, ‘What have we learned from high-pressure experiments on Cu-oxide and Fe-based superconductors?’, J. Phys. Conf. Ser. **449**, 012021 (2013).

[5] J. G. Bednorz and K. A. Müller, ‘Possible High $T_c$ Superconductivity in the Ba-La-Cu-O System’, Zeitschrift für Phys. B Condens. Matter **64**, 189–193 (1986).

[6] C. W. Chu, P. H. Hor, R. L. Meng, L. Gao, Z. J. Huang, Wang and Y. Q., ‘Evidence for Superconductivity above 40 K in the La-Ba-Cu-O Compound System’, Phys. Rev. Lett. **58**, 405–407 (1987).

[7] M. K. Wu, J. R. Ashburn, C. J. Torng, P. H. Hor, R. L. Meng, L. Gao, Z. J. Huang, Y. Q. Wang and C. W. Chu, ‘Superconductivity at 93 K in a New Mixed-Phase Y-Ba-Cu-O Compound System at Ambient Pressure’, Phys. Rev. Lett. **58**, 908–910 (1987).

[8] F. P. Bundy, H. T. Hall, H. M. Strong and R. H. Wentorf, ‘Man-Made Diamonds’, Nature **176**, 51–55 (1955).

[9] A. P. Drozdov, M. I. Eremets, I. A. Troyan, V. Ksenofontov and S. I. Shylin, ‘Conventional superconductivity at 203 K at high pressures in the sulfur hydride system’, Nature **525**, 73–76 (2015).

[10] Y. Ma, M. Eremets, A. R. Oganov, Y. Xie, I. Trojan, S. Medvedev, A. O. Lyakhov, M. Valle and V. Prakapenka, ‘Transparent dense sodium’, Nature **458**, 182–185 (2009).

[11] G. Kotliar and D. Vollhardt, ‘Strongly Correlated Materials: Insights From Dynamical Mean-Field Theory’, Phys. Today **57**, 53–59 (2004).

[12] D. I. Khomskii, *Transition Metal Compounds* (Cambridge University Press, Cambridge, 2014).

[13] I. Kantor, V. Prakapenka, A. Kantor, P. Dera, A. Kurnosov, S. Sinogeikin, N. Dubrovinskaia and L. Dubrovinsky, ‘BX90: A new diamond anvil cell design for X-ray diffraction and optical measurements’, Rev. Sci. Instrum. **83**, 125102 (2012).

[14] D. Kraus, N. J. Hartley, S. Frydrych, A. K. Schuster, K. Rohatsch, M. Rödel, T. E. Cowan, S. Brown, E. Cunningham, T. van Driel, L. B. Fletcher, E. Galtier, E. J. Gamboa, A. Laso Garcia, D. O. Gericke, E. Granados, P. A. Heimann, H. J. Lee, M. J. MacDonald, A. J. MacKinnon, E. E. McBride, I. Nam, P. Neumayer, A. Pak, A. Pelka, I. Prencipe, A. Ravasio, R. Redmer, A. M. Saunders, M. Schölmerich, M. Schörner, P. Sun, S. J. Turner, A. Zettl, R. W. Falcone, S. H. Glenzer, T. Döppner and J. Vorberger, ‘High-pressure chemistry of hydrocarbons relevant to planetary interiors and inertial confinement fusion’, Phys. Plasmas **25**, 056313 (2018).

[15] N. Dubrovinskaia, L. Dubrovinsky, N. A. Solopova, A. Abakumov, S. Turner, M. Hanfland, E. Bykova, M. Bykov, C. Prescher, V. B. Prakapenka, S. Petitgirard, I. Chuvashova, B. Gasharova, Y.-L. Mathis, P. Ershov, I. Snigireva and A. Snigirev, ‘Terapascal static pressure generation with ultrahigh yield strength nanodiamond’, Sci. Adv. **2**, e1600341 (2016).

[16] L. Dubrovinsky, N. Dubrovinskaia, E. Bykova, M. Bykov, V. Prakapenka, C. Prescher, K. Glazyrin, H.-P. Liermann, M. Hanfland, M. Ekholm, Q. Feng, L. V. Pourovskii, M. I. Katsnelson, J. M. Wills and I. A. Abrikosov, ‘The most incompressible metal osmium at static pressures above 750 gigapascals’, Nature **525**, 226–229 (2015).

[17] M. Mitrano, G. Cotugno, S. R. Clark, R. Singla, S. Kaiser, J. Stähler, R. Beyer, M. Dressel, L. Baldassarre, D. Nicoletti, A. Perucchi, T. Hasegawa, H. Okamoto, D. Jaksch and A. Cavalleri, ‘Pressure-Dependent Relaxation in the Photoexcited Mott Insulator ET–$F_2$TCNQ: Influence of Hopping and Correlations on Quasiparticle Recombination Rates’, Phys. Rev. Lett. **112**, 117801 (2014).

[18] W.-P. Hsieh, M. Trigo, D. A. Reis, G. A. Artioli, L. Malavasi and W. L. Mao, ‘Evidence for photo-induced monoclinic metallic $VO_2$ under high pressure’, Appl. Phys. Lett. **104**, 021917 (2014).

[19] C. Kübler, H. Ehrke, R. Huber, R. Lopez, A. Halabica, R. F. Haglund and A. Leitenstorfer, 'Coherent Structural Dynamics and Electronic Correlations during an Ultrafast Insulator-to-Metal Phase Transition in $VO_2$', Phys. Rev. Lett. **99**, 116401 (2007).

[20] J. M. Braun, H. Schneider, M. Helm, R. Mirek, L. A. Boatner, R. E. Marvel, R. F. Haglund and A. Pashkin, 'Ultrafast response of photoexcited carriers in $VO_2$ at high-pressure', New J. Phys. **20**, 083003 (2018).

[21] X. Zhu, Y. Cao, J. Zhang, E. W. Plummer and J. Guo, 'Classification of charge density waves based on their nature', Proc. Natl. Acad. Sci. **112**, 2367–2371 (2015).

[22] M. Eichberger, H. Schäfer, M. Krumova, M. Beyer, J. Demsar, H. Berger, G. Moriena, G. Sciaini and R. J. D. Miller, 'Snapshots of cooperative atomic motions in the optical suppression of charge density waves', Nature **468**, 799–802 (2010).

[23] R. E. Peierls, *Quantum Theory of Solids*, 2nd ed. (Oxford University Press, Oxford, 1956).

[24] J. Hubbard, 'Electron correlations in narrow energy bands', Proc. R. Soc. A Math. Phys. Eng. Sci. **276**, 238–257 (1963).

[25] N. F. Mott and R. Peierls, 'Discussion of the paper by de Boer and Verwey', Proc. Phys. Soc. **49**, 72–73 (1937).

[26] M. Imada, A. Fujimori and Y. Tokura, 'Metal-insulator transitions', Rev. Mod. Phys. **70**, 1039–1263 (1998).

[27] D. Vollhardt, 'Dynamical mean-field theory for correlated electrons', Ann. Phys. **524**, 1–19 (2012).

[28] M. J. Rozenberg, G. Kotliar, H. Kajueter, G. A. Thomas, D. H. Rapkine, J. M. Honig and P. Metcalf, 'Optical Conductivity in Mott-Hubbard Systems', Phys. Rev. Lett. **75**, 105–108 (1995).

[29] E. Arcangeletti, L. Baldassarre, D. Di Castro, S. Lupi, L. Malavasi, C. Marini, A. Perucchi and P. Postorino, 'Evidence of a Pressure-Induced Metallization Process in Monoclinic $VO_2$', Phys. Rev. Lett. **98**, 196406 (2007).

[30] P. W. Anderson, 'Absence of Diffusion in Certain Random Lattices', Phys. Rev. **109**, 1492–1505 (1958).

[31] V. Dobrosavljević, 'Introduction to Metal–Insulator Transitions', in *Conductor-Insulator Quantum Phase Transitions* (Oxford University Press, June 2012), pp. 3–63.

[32] A. Lagendijk, B. van Tiggelen and D. S. Wiersma, ‘Fifty years of Anderson localization’, Phys. Today **62**, 24–29 (2009).

[33] S.-i. Kimura and H. Okamura, ‘Infrared and Terahertz Spectroscopy of Strongly Correlated Electron Systems under Extreme Conditions’, J. Phys. Soc. Japan **82**, 021004 (2013).

[34] A. Jayaraman, ‘Diamond anvil cell and high-pressure physical investigations’, Rev. Mod. Phys. **55**, 65–108 (1983).

[35] A. Perucchi, L. Baldassarre, P. Postorino and S. Lupi, ‘Optical properties across the insulator to metal transitions in vanadium oxide compounds’, J. Phys. Condens. Matter **21**, 323202 (2009).

[36] H.-K. Mao, X.-J. Chen, Y. Ding, B. Li and L. Wang, ‘Solids, liquids, and gases under high pressure’, Rev. Mod. Phys. **90**, 015007 (2018).

[37] J. Loveday, ed., *High-pressure physics* (CRC Press, Boca Raton London New York, 2012).

[38] J. M. Recio, J. M. Menendez and A. Otero de la Roza, eds., *An Introduction to High-Pressure Science and Technology* (CRC Press, Boca Raton London New York, 2015).

[39] C. Rullière, T. Amand and X. Marie, ‘Spectroscopic Methods for Analysis of Sample Dynamics’, in *Femtosecond Laser Pulses : Principles and Experiments*, edited by C. Rullière, 2nd ed. (Springer, New York, 2005), pp. 223–281.

[40] R. P. Mildren, ‘Intrinsic Optical Properties of Diamond’, in *Optical Engineering of Diamond*, edited by R. P. Mildren and J. R. Rabeau (Wiley-VCH Verlag GmbH & Co. KGaA, Weinheim, Germany, 2013), pp. 1–34.

[41] C. J. H. Wort and R. S. Balmer, ‘Diamond as an electronic material’, Mater. Today **11**, 22–28 (2008).

[42] R. Boehler and K. De Hantsetters, ‘New anvil designs in diamond-cells’, High Press. Res. **24**, 391–396 (2004).

[43] D. J. Dunstan, ‘Theory of the gasket in diamond anvil high-pressure cells’, Rev. Sci. Instrum. **60**, 3789–3795 (1989).

[44] S. Klotz, J. C. Chervin, P. Munsch and G. Le Marchand, ‘Hydrostatic limits of 11 pressure transmitting media’, J. Phys. D. Appl. Phys. **42**, 075413 (2009).

[45] H. K. Mao, J. Xu and P. M. Bell, ‘Calibration of the ruby pressure gauge to 800 kbar under quasi-hydrostatic conditions’, J. Geophys. Res. **91**, 4673–4676 (1986).

[46] M. Hanfland and K. Syassen, ‘A Raman study of diamond anvils under stress’, J. Appl. Phys. **57**, 2752–2756 (1985).

[47] Y. Akahama and H. Kawamura, ‘Pressure calibration of diamond anvil Raman gauge to 310 GPa’, J. Appl. Phys. **100**, 043516 (2006).

[48] M. I. Eremets, V. V. Struzhkin, J. A. Timofeev, I. A. Trojan, A. N. Utjuzh and A. M. Shirokov, ‘Refractive index of diamond under pressure’, High Press. Res. **9**, 347–350 (1992).

[49] J. M. Tomczak and S. Biermann, ‘Optical properties of correlated materials – Or why intelligent windows may look dirty’, Phys. Status Solidi B **246**, 1996–2005 (2009).

[50] K. J. Miller, R. F. Haglund and S. M. Weiss, ‘Optical phase change materials in integrated silicon photonic devices: review’, Opt. Mater. Express **8**, 2415–2429 (2018).

[51] F. Cilento, C. Giannetti, G. Ferrini, S. Dal Conte, T. Sala, G. Coslovich, M. Rini, A. Cavalleri and F. Parmigiani, ‘Ultrafast insulator-to-metal phase transition as a switch to measure the spectrogram of a supercontinuum light pulse’, Appl. Phys. Lett. **96**, 021102 (2010).

[52] F. J. Morin, ‘Oxides Which Show a Metal-to-Insulator Transition at the Neel Temperature’, Phys. Rev. Lett. **3**, 34–36 (1959).

[53] J. B. Goodenough, ‘The Two Components of the Crystallographic Transition in $VO_2$’, J. Solid State Chem. **3**, 490–500 (1971).

[54] J. Galy and G. Miehe, ‘Ab initio structures of (M2) and (M3) $VO_2$ high pressure phases’, Solid State Sci. **1**, 433–448 (1999).

[55] D. B. McWhan, M. Marezio, J. P. Remeika and P. D. Dernier, ‘X-ray diffraction study of metallic $VO_2$’, Phys. Rev. B **10**, 490–495 (1974).

[56] G. Andersson, ‘Studies on Vanadium Oxides: II. The Crystal Structure of Vanadium Dioxide’, Acta Chem. Scand. **10**, 623–628 (1956).

[57] M. Baldini, P. Postorino, L. Malavasi, C. Marini, K. W. Chapman and H.-k. Mao, ‘Pair distribution function analysis: The role of structural degrees of freedom in the high-pressure insulator to metal transition of $VO_2$’, Phys. Rev. B **93**, 245137 (2016).

[58] D. Kucharczyk and T. Niklewski, ‘Accurate X-ray Determination of the Lattice Parameters and the Thermal Expansion Coefficients of $VO_2$ near the Transition Temperature’, J. Appl. Crystallogr. **12**, 370–373 (1979).

[59] M. Mitrano, B. Maroni, C. Marini, M. Hanfland, B. Joseph, P. Postorino and L. Malavasi, ‘Anisotropic compression in the high-pressure regime of pure and chromium-doped vanadium dioxide’, Phys. Rev. B **85**, 184108 (2012).

[60] Q. Li, H. Zhang, C. Lin, F. Tian, J. S. Smith, C. Park, B. Liu and G. Shen, ‘Pressure-induced phase transitions and insulator-metal transitions in $VO_2$ nanoparticles’, J. Alloys Compd. **709**, 260–266 (2017).

[61] L. Bai, Q. Li, S. A. Corr, Y. Meng, C. Park, S. V. Sinogeikin, C. Ko, J. Wu and G. Shen, ‘Pressure-induced phase transitions and metallization in $VO_2$’, Phys. Rev. B **91**, 104110 (2015).

[62] H. He, H. Gao, W. Wu, S. Cao, J. Hong, D. Yu, G. Deng, Y. Gao, P. Zhang, H. Luo and W. Ren, ‘Phonon instability and pressure-induced isostructural semiconductor-semimetal transition of monoclinic $VO_2$’, Phys. Rev. B **94**, 205127 (2016).

[63] H. Zhang, Q. Li, B. Cheng, Z. Guan, R. Liu, B. Liu, Z. Liu, X. Li, T. Cui and B. Liu, ‘The pressure-induced metallization of monoclinic vanadium dioxide’, RSC Adv. **6**, 104949–104954 (2016).

[64] Y. Chen, S. Zhang, F. Ke, C. Ko, S. Lee, K. Liu, B. Chen, J. W. Ager, R. Jeanloz, V. Eyert and J. Wu, ‘Pressure–Temperature Phase Diagram of Vanadium Dioxide’, Nano Lett. **17**, 2512–2516 (2017).

[65] S.-Y. Xie, L. Wang, F. Liu, X.-B. Li, L. Bai, V. B. Prakapenka, Z. Cai, H.-k. Mao, S. Zhang and H. Liu, ‘Correlated High-Pressure Phase Sequence of $VO_2$ under Strong Compression’, J. Phys. Chem. Lett. **9**, 2388–2393 (2018).

[66] M. Marezio, D. B. McWhan, J. P. Remeika and P. D. Dernier, ‘Structural Aspects of the Metal-Insulator Transitions in Cr-Doped $VO_2$’, Phys. Rev. B **5**, 2541–2551 (1972).

[67] J. P. Pouget, H. Launois, T. M. Rice, P. Dernier, A. Gossard, G. Villeneuve and P. Hagenmuller, ‘Dimerization of a linear Heisenberg chain in the insulating phases of $V_{1-x}Cr_xO_2$’, Phys. Rev. B **10**, 1801–1815 (1974).

[68] B. L. Chamberland, ‘New Defect Vanadium Dioxide Phases’, J. Solid State Chem. **7**, 377–384 (1973).

[69] J. H. Park, J. M. Coy, T. S. Kasirga, C. Huang, Z. Fei, S. Hunter and D. H. Cobden, ‘Measurement of a solid-state triple point at the metal–insulator transition in $VO_2$’, Nature **500**, 431–434 (2013).

[70] B. T. O'Callahan, A. C. Jones, J. Hyung Park, D. H. Cobden, J. M. Atkin and M. B. Raschke, 'Inhomogeneity of the ultrafast insulator-to-metal transition dynamics of $VO_2$', Nat. Commun. **6**, 6849 (2015).

[71] M. A. Huber, M. Plankl, M. Eisele, R. E. Marvel, F. Sandner, T. Korn, C. Schüller, R. F. Haglund, R. Huber and T. L. Cocker, 'Ultrafast Mid-Infrared Nanoscopy of Strained Vanadium Dioxide Nanobeams', Nano Lett. **16**, 1421–1427 (2016).

[72] H. Guo, K. Chen, Y. Oh, K. Wang, C. Dejoie, S. A. Syed Asif, O. L. Warren, Z. W. Shan, J. Wu and A. M. Minor, 'Mechanics and Dynamics of the Strain-Induced M1–M2 Structural Phase Transition in Individual $VO_2$ Nanowires', Nano Lett. **11**, 3207–3213 (2011).

[73] J. Cao, Y. Gu, W. Fan, L. Q. Chen, D. F. Ogletree, K. Chen, N. Tamura, M. Kunz, C. Barrett, J. Seidel and J. Wu, 'Extended Mapping and Exploration of the Vanadium Dioxide Stress-Temperature Phase Diagram', Nano Lett. **10**, 2667–2673 (2010).

[74] Y. Oka, T. Yao and N. Yamamoto, 'Structural Phase Transition of $VO_2$(B) to $VO_2$(A)', J. Mater. Chem. **1**, 815–818 (1991).

[75] Y. Wang, J. Zhu, W. Yang, T. Wen, M. Pravica, Z. Liu, M. Hou, Y. Fei, L. Kang, Z. Lin, C. Jin and Y. Zhao, 'Reversible switching between pressure-induced amorphization and thermal-driven recrystallization in $VO_2$(B) nanosheets', Nat. Commun. **7**, 12214 (2016).

[76] B. Cheng, Q. Li, H. Zhang, R. Liu, B. Liu, Z. Yao, T. Cui, J. Liu, Z. Liu, B. Sundqvist and B. Liu, 'Pressure-induced metallization and amorphization in $VO_2$(A) nanorods', Phys. Rev. B **93**, 184109 (2016).

[77] J. Lu, K. G. West and S. A. Wolf, 'Very large anisotropy in the dc conductivity of epitaxial $VO_2$ thin films grown on (011) rutile $TiO_2$ substrates', Appl. Phys. Lett. **93**, 262107 (2008).

[78] N. B. Aetukuri, A. X. Gray, M. Drouard, M. Cossale, L. Gao, A. H. Reid, R. Kukreja, H. Ohldag, C. A. Jenkins, E. Arenholz, K. P. Roche, H. A. Dürr, M. G. Samant and S. S. P. Parkin, 'Control of the metal–insulator transition in vanadium dioxide by modifying orbital occupancy', Nat. Phys. **9**, 661–666 (2013).

[79] A. X. Gray, J. Jeong, N. P. Aetukuri, P. Granitzka, Z. Chen, R. Kukreja, D. Higley, T. Chase, A. H. Reid, H. Ohldag, M. A. Marcus, A. Scholl, A. T. Young, A. Doran, C. A. Jenkins, P. Shafer, E. Arenholz, M. G. Samant, S. S. P. Parkin and H. A. Dürr, 'Correlation-Driven Insulator-Metal Transition in Near-Ideal Vanadium Dioxide Films', Phys. Rev. Lett. **116**, 116403 (2016).

[80] L. A. Ladd and W. Paul, 'Optical and transport properties of high quality crystals of $V_2O_4$ near the metallic transition temperature', Solid State Commun. **7**, 425–428 (1969).

[81] V. Eyert, '$VO_2$: A Novel View from Band Theory', Phys. Rev. Lett. **107**, 016401 (2011).

[82] S. Biermann, A. Poteryaev, A. I. Lichtenstein and A. Georges, 'Dynamical Singlets and Correlation-Assisted Peierls Transition in $VO_2$', Phys. Rev. Lett. **94**, 026404 (2005).

[83] R. J. Powell, C. N. Berglund and W. E. Spicer, 'Photoemission from $VO_2$', Phys. Rev. **178**, 1410–1415 (1969).

[84] S. Shin, S. Suga, M. Taniguchi, M. Fujisawa, H. Kanzaki, A. Fujimori, H. Daimon, Y. Ueda, K. Kosuge and S. Kachi, 'Vacuum-ultraviolet reflectance and photoemission study of the metal-insulator phase transitions in $VO_2$, $V_6O_{13}$, and $V_2O_3$', Phys. Rev. B **41**, 4993–5009 (1990).

[85] R. Eguchi, M. Taguchi, M. Matsunami, K. Horiba, K. Yamamoto, Y. Ishida, A. Chainani, Y. Takata, M. Yabashi, D. Miwa, Y. Nishino, K. Tamasaku, T. Ishikawa, Y. Senba, H. Ohashi, Y. Muraoka, Z. Hiroi and S. Shin, 'Photoemission evidence for a Mott-Hubbard metal-insulator transition in $VO_2$', Phys. Rev. B **78**, 075115 (2008).

[86] M. W. Haverkort, Z. Hu, A. Tanaka, W. Reichelt, S. V. Streltsov, M. A. Korotin, V. I. Anisimov, H. H. Hsieh, H.-J. Lin, C. T. Chen, D. I. Khomskii and L. H. Tjeng, 'Orbital-Assisted Metal-Insulator Transition in $VO_2$', Phys. Rev. Lett. **95**, 196404 (2005).

[87] T. C. Koethe, Z. Hu, M. W. Haverkort, C. Schüßler-Langeheine, F. Venturini, N. B. Brookes, O. Tjernberg, W. Reichelt, H. H. Hsieh, H.-J. Lin, C. T. Chen and L. H. Tjeng, 'Transfer of Spectral Weight and Symmetry across the Metal-Insulator Transition in $VO_2$', Phys. Rev. Lett. **97**, 116402 (2006).

[88] C. Marini, S. Pascarelli, O. Mathon, B. Joseph, L. Malavasi and P. Postorino, 'Tracking competitive lattice distortions in strongly correlated $VO_2$-based systems: A temperature-dependent EXAFS study', Europhys. Lett. **102**, 66004 (2013).

[89] D. Wegkamp, M. Herzog, L. Xian, M. Gatti, P. Cudazzo, C. L. McGahan, R. E. Marvel, R. F. Haglund, A. Rubio, M. Wolf and J. Stähler, 'Instantaneous Band Gap Collapse in Photoexcited Monoclinic $VO_2$ due to Photocarrier Doping', Phys. Rev. Lett. **113**, 216401 (2014).

[90] J. Laverock, S. Kittiwatanakul, A. A. Zakharov, Y. R. Niu, B. Chen, S. A. Wolf, J. W. Lu and K. E. Smith, 'Direct Observation of Decoupled Structural and Electronic Transitions and an Ambient Pressure Monocliniclike Metallic Phase of $VO_2$', Phys. Rev. Lett. **113**, 216402 (2014).

[91] M. F. Jager, C. Ott, P. M. Kraus, C. J. Kaplan, W. Pouse, R. E. Marvel, R. F. Haglund, D. M. Neumark and S. R. Leone, 'Tracking the insulator-to-metal phase transition in $VO_2$ with few-femtosecond extreme UV transient absorption spectroscopy', Proc. Natl. Acad. Sci. **114**, 9558–9563 (2017).

[92] H. W. Verleur, A. S. Barker and C. N. Berglund, 'Optical Properties of $VO_2$ between 0.25 and 5 eV', Rev. Mod. Phys. **40**, 737–737 (1968).

[93] C. N. Berglund and H. J. Guggenheim, 'Electronic Properties of $VO_2$ near the Semiconductor-Metal Transition', Phys. Rev. **185**, 1022–1033 (1969).

[94] C. N. Berglund and A. Jayaraman, 'Hydrostatic-Pressure Dependence of the Electronic Properties of $VO_2$ Near the Semiconductor-Metal Transition Temperature', Phys. Rev. **185**, 1034–1039 (1969).

[95] C. H. Neuman, A. W. Lawson and R. F. Brown, 'Pressure Dependence of the Resistance of $VO_2$', J. Chem. Phys. **41**, 1591–1595 (1964).

[96] A. Gavini and C. C. Y. Kwan, 'Optical Properties of Semiconducting $VO_2$ Films', Phys. Rev. B **5**, 3138–3143 (1972).

[97] A. S. Barker, H. W. Verleur and H. J. Guggenheim, 'Infrared Optical Properties of Vanadium Dioxide Above and Below the Transition Temperature', Phys. Rev. Lett. **17**, 1286–1289 (1966).

[98] A. Zimmers, L. Aigouy, M. Mortier, A. Sharoni, S. Wang, K. G. West, J. G. Ramirez and I. K. Schuller, 'Role of Thermal Heating on the Voltage Induced Insulator-Metal Transition in $VO_2$', Phys. Rev. Lett. **110**, 056601 (2013).

[99] M. M. Qazilbash, M. Brehm, G. O. Andreev, A. Frenzel, P.-C. Ho, B.-G. Chae, B.-J. Kim, S. J. Yun, H.-T. Kim, A. V. Balatsky, O. G. Shpyrko, M. B. Maple, F. Keilmann and D. N. Basov, 'Infrared spectroscopy and nano-imaging of the insulator-to-metal transition in vanadium dioxide', Phys. Rev. B **79**, 075107 (2009).

[100] R. M. Wentzcovitch, W. W. Schulz and P. B. Allen, '$VO_2$: Peierls or Mott-Hubbard? A View from Band Theory', Phys. Rev. Lett. **72**, 3389–3392 (1994).

[101] T. M. Rice, H. Launois and J. P. Pouget, 'Comment on "$VO_2$: Peierls or Mott-Hubbard? A View from Band Theory"', Phys. Rev. Lett. **73**, 3042 (1994).

[102] R. M. Wentzcovitch, W. W. Schulz and P. B. Allen, 'Wentzcovitch *et al.* Reply', Phys. Rev. Lett. **73**, 3043 (1994).

[103] A. Georges, G. Kotliar, W. Krauth and M. J. Rozenberg, 'Dynamical mean-field theory of strongly correlated fermion systems and the limit of infinite dimensions', Rev. Mod. Phys. **68**, 13–125 (1996).

[104] D. N. Basov, R. D. Averitt, D. van der Marel, M. Dressel and K. Haule, 'Electrodynamics of correlated electron materials', Rev. Mod. Phys. **83**, 471–541 (2011).

[105] M. J. Rozenberg, G. Kotliar and H. Kajueter, 'Transfer of spectral weight in spectroscopies of correlated electron systems', Phys. Rev. B **54**, 8452–8468 (1996).

[106] V. Eyert, 'The metal-insulator transitions of $VO_2$ : A band theoretical approach', Ann. Phys. **11**, 650–702 (2002).

[107] J. M. Tomczak, F. Aryasetiawan and S. Biermann, 'Effective bandstructure in the insulating phase versus strong dynamical correlations in metallic $VO_2$', Phys. Rev. B **78**, 115103 (2008).

[108] C. Weber, D. D. O'Regan, N. D. M. Hine, M. C. Payne, G. Kotliar and P. B. Littlewood, 'Vanadium Dioxide: A Peierls-Mott Insulator Stable against Disorder', Phys. Rev. Lett. **108**, 256402 (2012).

[109] M. van Veenendaal, 'Ultrafast photoinduced insulator-to-metal transitions in vanadium dioxide', Phys. Rev. B **87**, 235118 (2013).

[110] W. H. Brito, M. C. O. Aguiar, K. Haule and G. Kotliar, 'Metal-Insulator Transition in $VO_2$: A DFT+DMFT Perspective', Phys. Rev. Lett. **117**, 056402 (2016).

[111] O. Nájera, M. Civelli, V. Dobrosavljević and M. J. Rozenberg, 'Multiple crossovers and coherent states in a Mott-Peierls insulator', Phys. Rev. B **97**, 045108 (2018).

[112] M. Gatti, F. Bruneval, V. Olevano and L. Reining, 'Understanding Correlations in Vanadium Dioxide from First Principles', Phys. Rev. Lett. **99**, 266402 (2007) (2007).

[113] D. Plašienka, R. Martoňák and M. C. Newton, 'Ab initio molecular dynamics study of the structural and electronic transition in $VO_2$', Phys. Rev. B **96**, 054111 (2017).

[114] D. Lee, B. Chung, Y. Shi, G.-Y. Kim, N. Campbell, F. Xue, K. Song, S.-Y. Choi, J. P. Podkaminer, T. H. Kim, P. J. Ryan, J.-W. Kim, T. R. Paudel, J.-H. Kang, J. W. Spinuzzi, D. A. Tenne, E. Y. Tsymbal, M. S. Rzchowski, L. Q. Chen, J. Lee and C. B. Eom, 'Isostructural metal-insulator transition in $VO_2$', Science **362**, 1037–1040 (2018).

[115] J. Nag, R. F. Haglund, E. Andrew Payzant and K. L. More, 'Non-congruence of thermally driven structural and electronic transitions in $VO_2$', J. Appl. Phys. **112**, 103532 (2012).

[116] M. M. Qazilbash, M. Brehm, B.-G. Chae, P.-C. Ho, G. O. Andreev, B.-J. Kim, S. J. Yun, A. V. Balatsky, M. B. Maple, F. Keilmann, H.-T. Kim and D. N. Basov, 'Mott Transition in $VO_2$ Revealed by Infrared Spectroscopy and Nano-Imaging', Science **318**, 1750–1753 (2007).

[117] M. F. Becker, A. B. Buckman, R. M. Walser, T. Lépine, P. Georges and A. Brun, 'Femtosecond laser excitation of the semiconductor-metal phase transition in $VO_2$', Appl. Phys. Lett. **65**, 1507–1509 (1994).

[118] A. Cavalleri, C. Tóth, C. W. Siders, J. A. Squier, F. Ráksi, P. Forget and J. C. Kieffer, 'Femtosecond Structural Dynamics in $VO_2$ during an Ultrafast Solid-Solid Phase Transition', Phys. Rev. Lett. **87**, 237401 (2001).

[119] A. Cavalleri, T. Dekorsy, H. H. W. Chong, J. C. Kieffer and R. W. Schoenlein, 'Evidence for a structurally-driven insulator-to-metal transition in $VO_2$: A view from the ultrafast timescale', Phys. Rev. B **70**, 161102 (2004).

[120] A. Pashkin, C. Kübler, H. Ehrke, R. Lopez, A. Halabica, R. F. Haglund, R. Huber and A. Leitenstorfer, 'Ultrafast insulator-metal phase transition in $VO_2$ studied by multiterahertz spectroscopy', Phys. Rev. B **83**, 195120 (2011).

[121] T. L. Cocker, L. V. Titova, S. Fourmaux, G. Holloway, H.-C. Bandulet, D. Brassard, J.-C. Kieffer, M. A. El Khakani and F. A. Hegmann, 'Phase diagram of the ultrafast photoinduced insulator-metal transition in vanadium dioxide', Phys. Rev. B **85**, 155120 (2012).

[122] D. J. Hilton, R. P. Prasankumar, S. Fourmaux, A. Cavalleri, D. Brassard, M. A. El Khakani, J. C. Kieffer, A. J. Taylor and R. D. Averitt, 'Enhanced Photosusceptibility near $T_c$ for the Light-Induced Insulator-to-Metal Phase Transition in Vanadium Dioxide', Phys. Rev. Lett. **99**, 226401 (2007).

[123] M. Nakajima, N. Takubo, Z. Hiroi, Y. Ueda and T. Suemoto, 'Photoinduced metallic state in $VO_2$ proved by the terahertz pump-probe spectroscopy', Appl. Phys. Lett. **92**, 011907 (2008).

[124] M. R. Bionta, V. Wanie, V. Gruson, J. Chaillou, N. Émond, D. Lepage, P. Lassonde, M. Chaker and F. Légaré, 'Probing the phase transition in $VO_2$ using few-cycle 1.8 µm pulses', Phys. Rev. B **97**, 125126 (2018).

[125] S. Lysenko, N. Kumar, A. Rúa, J. Figueroa, J. Lu and F. Fernández, 'Ultrafast structural dynamics of $VO_2$', Phys. Rev. B **96**, 075128 (2017).

[126] A. Cavalleri, H. H. W. Chong, S. Fourmaux, T. E. Glover, P. A. Heimann, J. C. Kieffer, B. S. Mun, H. A. Padmore and R. W. Schoenlein, 'Picosecond soft x-ray absorption measurement of the photoinduced insulator-to-metal transition in $VO_2$', Phys. Rev. B **69**, 153106 (2004).

[127] A. Cavalleri, M. Rini, H. H. W. Chong, S. Fourmaux, T. E. Glover, P. A. Heimann, J. C. Kieffer and R. W. Schoenlein, 'Band-Selective Measurements of Electron Dynamics in $VO_2$ Using Femtosecond Near-Edge X-Ray Absorption', Phys. Rev. Lett. **95**, 067405 (2005).

[128] S. Wall, D. Wegkamp, L. Foglia, K. Appavoo, J. Nag, R. F. Haglund, J. Stähler and M. Wolf, 'Ultrafast changes in lattice symmetry probed by coherent phonons', Nat. Commun. **3**, 721 (2012).

[129] S. Wall, L. Foglia, D. Wegkamp, K. Appavoo, J. Nag, R. F. Haglund, J. Stähler and M. Wolf, 'Tracking the evolution of electronic and structural properties of $VO_2$ during the ultrafast photoinduced insulator-metal transition', Phys. Rev. B **87**, 115126 (2013).

[130] P. Baum, D.-S. Yang and A. H. Zewail, '4D Visualization of Transitional Structures in Phase Transformations by Electron Diffraction', Science **318**, 788–792 (2007).

[131] V. R. Morrison, R. P. Chatelain, K. L. Tiwari, A. Hendaoui, A. Bruhács, M. Chaker and B. J. Siwick, 'A photoinduced metal-like phase of monoclinic $VO_2$ revealed by ultrafast electron diffraction', Science **346**, 445–448 (2014).

[132] B. Mayer, C. Schmidt, A. Grupp, J. Bühler, J. Oelmann, R. E. Marvel, R. F. Haglund, T. Oka, D. Brida, A. Leitenstorfer and A. Pashkin, 'Tunneling breakdown of a strongly correlated insulating state in $VO_2$ induced by intense multiterahertz excitation', Phys. Rev. B **91**, 235113 (2015).

[133] M. Liu, H. Y. Hwang, H. Tao, A. C. Strikwerda, K. Fan, G. R. Keiser, A. J. Sternbach, K. G. West, S. Kittiwatanakul, J. Lu, S. A. Wolf, F. G. Omenetto, X. Zhang, K. A. Nelson and R. D. Averitt, 'Terahertz-field-induced insulator-to-metal transition in vanadium dioxide metamaterial', Nature **487**, 345–348 (2012).

[134] M. Rini, Z. Hao, R. W. Schoenlein, C. Giannetti, F. Parmigiani, S. Fourmaux, J. C. Kieffer, A. Fujimori, M. Onoda, S. Wall and A. Cavalleri, 'Optical switching in $VO_2$ films by below-gap excitation', Appl. Phys. Lett. **92**, 181904 (2008).

[135] C. Marini, E. Arcangeletti, D. Di Castro, L. Baldassare, A. Perucchi, S. Lupi, L. Malavasi, L. Boeri, E. Pomjakushina, K. Conder and P. Postorino, 'Optical properties of $V_{1-x}Cr_xO_2$ compounds under high pressure', Phys. Rev. B **77**, 235111 (2008).

[136] C. Marini, M. Bendele, B. Joseph, I. Kantor, M. Mitrano, O. Mathon, M. Baldini, L. Malavasi, S. Pascarelli and P. Postorino, 'Probing the electronic and local structural changes across the pressure-induced insulator-to-metal transition in $VO_2$', Europhys. Lett. **108**, 36003 (2014).

[137] X. Zhang, J. Zhang, F. Ke, G. Li, Y. Ma, X. Liu, C. Liu, Y. Han, Y. Ma and C. Gao, 'Anomalous semiconducting behavior on $VO_2$ under high pressure', RSC Adv. **5**, 54843–54847 (2015).

[138] J. D. Budai, J. Hong, M. E. Manley, E. D. Specht, C. W. Li, J. Z. Tischler, D. L. Abernathy, A. H. Said, B. M. Leu, L. A. Boatner, R. J. McQueeney and O. Delaire, 'Metallization of vanadium dioxide driven by large phonon entropy', Nature **515**, 535–539 (2014).

[139] T.-Y. Chen, C.-H. Hsia, H. S. Son and D. H. Son, 'Ultrafast Energy Transfer and Strong Dynamic Non-Condon Effect on Ligand Field Transitions by Coherent Phonon in $\gamma$-$Fe_2O_3$ Nanocrystals', J. Am. Chem. Soc. **129**, 10829–10836 (2007).

[140] C. A. Kuntscher, S. Frank, A. Pashkin, M. Hoinkis, M. Klemm, M. Sing, S. Horn and R. Claessen, 'Possible pressure-induced insulator-to-metal transition in low-dimensional TiOCl', Phys. Rev. B **74**, 184402 (2006).

[141] C. A. Kuntscher, A. Pashkin, H. Hoffmann, S. Frank, M. Klemm, S. Horn, A. Schönleber, S. van Smaalen, M. Hanfland, S. Glawion, M. Sing and R. Claessen, ‘Mott-Hubbard gap closure and structural phase transition in the oxyhalides TiOBr and TiOCl under pressure’, Phys. Rev. B **78**, 035106 (2008).

[142] M. M. Qazilbash, K. S. Burch, D. Whisler, D. Shrekenhamer, B. G. Chae, H. T. Kim and D. N. Basov, ‘Correlated metallic state of vanadium dioxide’, Phys. Rev. B **74**, 205118 (2006).

[143] X. Y. Zhang, M. J. Rozenberg and G. Kotliar, ‘Mott Transition in the $d = \infty$ Hubbard Model at Zero Temperature’, Phys. Rev. Lett. **70**, 1666–1669 (1993).

[144] O. Nájera, M. Civelli, V. Dobrosavljević and M. J. Rozenberg, ‘Resolving the $VO_2$ controversy: Mott mechanism dominates the insulator-to-metal transition’, Phys. Rev. B **95**, 035113 (2017).

[145] J. Cao, W. Fan, K. Chen, N. Tamura, M. Kunz, V. Eyert and J. Wu, ‘Constant threshold resistivity in the metal-insulator transition of $VO_2$’, Phys. Rev. B **82**, 241101 (2010).

[146] R. M. Cornell and U. Schwertmann, *The Iron Oxides. Structure, Properties, Reactions, Occurences and Uses*, 2nd ed. (Wiley-VCH Verlag GmbH & Co. KGaA, Weinheim, 2003).

[147] J. Tuček, L. Machala, S. Ono, A. Namai, M. Yoshikiyo, K. Imoto, H. Tokoro, S.-i. Ohkoshi and R. Zbořil, ‘Zeta-$Fe_2O_3$ – A new stable polymorph in iron(III) oxide family’, Sci. Rep. **5**, 15091 (2015).

[148] J. B. Baxter, C. Richter and C. A. Schmuttenmaer, ‘Ultrafast Carrier Dynamics in Nanostructures for Solar Fuels’, Annu. Rev. Phys. Chem. **65**, 423–447 (2014).

[149] S.-H. Shim, A. Bengtson, D. Morgan, W. Sturhahn, K. Catalli, J. Zhao, M. Lerche and V. Prakapenka, ‘Electronic and magnetic structures of the postperovskite-type $Fe_2O_3$ and implications for planetary magnetic records and deep interiors’, Proc. Natl. Acad. Sci. **106**, 5508–5512 (2009).

[150] E. Bykova, L. Dubrovinsky, N. Dubrovinskaia, M. Bykov, C. McCammon, S. V. Ovsyannikov, H.-P. Liermann, I. Kupenko, A. I. Chumakov, R. Rüffer, M. Hanfland and V. Prakapenka, ‘Structural complexity of simple $Fe_2O_3$ at high pressures and temperatures’, Nat. Commun. **7**, 10661 (2016).

[151] E. Greenberg, I. Leonov, S. Layek, Z. Konopkova, M. P. Pasternak, L. Dubrovinsky, R. Jeanloz, I. A. Abrikosov and G. K. Rozenberg, 'Pressure-Induced Site-Selective Mott Insulator-Metal Transition in $Fe_2O_3$', Phys. Rev. X **8**, 031059 (2018).

[152] M. P. Pasternak, G. K. Rozenberg, G. Y. Machavariani, O. Naaman, R. D. Taylor and R. Jeanloz, 'Breakdown of the Mott-Hubbard State in $Fe_2O_3$: A First-Order Insulator-Metal Transition with Collapse of Magnetism at 50 GPa', Phys. Rev. Lett. **82**, 4663–4666 (1999).

[153] E. Knittle and R. Jeanloz, 'High-pressure electrical resistivity measurements of $Fe_2O_3$: Comparison of static-compression and shock-wave experiments to 61 GPa', Solid State Commun. **58**, 129–131 (1986).

[154] P. Schouwink, L. Dubrovinsky, K. Glazyrin, M. Merlini, M. Hanfland, T. Pippinger and R. Miletich, 'High-pressure structural behavior of $\alpha$-$Fe_2O_3$ studied by single-crystal X-ray diffraction and synchrotron radiation up to 25 GPa', Am. Mineral. **96**, 1781–1786 (2011).

[155] A. M. Jubb and H. C. Allen, 'Vibrational Spectroscopic Characterization of Hematite, Maghemite, and Magnetite Thin Films Produced by Vapor Deposition', ACS Appl. Mater. Interfaces **2**, 2804–2812 (2010).

[156] A. Sanson, I. Kantor, V. Cerantola, T. Irifune, A. Carnera and S. Pascarelli, 'Local structure and spin transition in $Fe_2O_3$ hematite at high pressure', Phys. Rev. B **94**, 014112 (2016).

[157] G. K. Rozenberg, L. S. Dubrovinsky, M. P. Pasternak, O. Naaman, T. Le Bihan and R. Ahuja, 'High-pressure structural studies of hematite $Fe_2O_3$', Phys. Rev. B **65**, 064112 (2002).

[158] E. Ito, H. Fukui, T. Katsura, D. Yamazaki, T. Yoshino, Y. Aizawa, A. Kubo, S. Yokoshi, K. Kawabe, S. Zhai, A. Shatzkiy, M. Okube, A. Nozawa and K.-I. Funakoshi, 'Determination of high-pressure phase equilibria of $Fe_2O_3$ using the Kawai-type apparatus equipped with sintered diamond anvils', Am. Mineral. **94**, 205–209 (2009).

[159] E. Bykova, M. Bykov, V. Prakapenka, Z. Konôpková, H.-P. Liermann, N. Dubrovinskaia and L. Dubrovinsky, 'Novel high pressure monoclinic $Fe_2O_3$ polymorph revealed by single-crystal synchrotron X-ray diffraction studies', High Press. Res. **33**, 534–545 (2013).

[160] S.-H. Shim and T. S. Duffy, 'Raman spectroscopy of $Fe_2O_3$ to 62 GPa', Am. Mineral. **87**, 318–326 (2002).

[161] L. Dubrovinsky, T. Boffa-Ballaran, K. Glazyrin, A. Kurnosov, D. Frost, M. Merlini, M. Hanfland, V. B. Prakapenka, P. Schouwink, T. Pippinger and N. Dubrovinskaia, ‘Single-crystal X-ray diffraction at megabar pressures and temperatures of thousands of degrees’, High Press. Res. **30**, 620–633 (2010).

[162] L. A. Marusak, R. Messier and W. B. White, ‘Optical absorption spectrum of hematite, $\alpha$-$Fe_2O_3$ near IR to UV’, J. Phys. Chem. Solids **41**, 981–984 (1980).

[163] S. Klotz, T. Strässle and T. Hansen, ‘Pressure dependence of Morin transition in $\alpha$-$Fe_2O_3$ hematite’, EPL **104**, 16001 (2013).

[164] F. J. Morin, ‘Magnetic Susceptibility of $\alpha Fe_2O_3$ and $\alpha Fe_2O_3$ with Added Titanium’, Phys. Rev. **78**, 819–820 (1950).

[165] Y. Syono, A. Ito, S. Morimoto, T. Suzuki, T. Yagi and S.-i. Akimoto, ‘Mössbauer study on the high pressure phase of $Fe_2O_3$’, Solid State Commun. **50**, 97–100 (1984).

[166] K. Kurimoto, S. Nasu, S. Nagatomo, S. Endo and F. Fujita, ‘Mössbauer study of $\alpha$-$Fe_2O_3$ under ultra-high pressure’, Phys. B+C **139-140**, 495–498 (1986).

[167] Y. Ma, P. D. Johnson, N. Wassdahl, J. Guo, P. Skytt, J. Nordgren, S. D. Kevan, J.-E. Rubensson, T. Böske and W. Eberhardt, ‘Electronic structures of $\alpha$-$Fe_2O_3$ and $Fe_3O_4$ from O $K$-edge absorption and emission spectroscopy’, Phys. Rev. B **48**, 2109–2111 (1993).

[168] S. Wang, W. L. Mao, A. P. Sorini, C.-C. Chen, T. P. Devereaux, Y. Ding, Y. Xiao, P. Chow, N. Hiraoka, H. Ishii, Y. Q. Cai and C.-C. Kao, ‘High-pressure evolution of $Fe_2O_3$ electronic structure revealed by x-ray absorption’, Phys. Rev. B **82**, 144428 (2010).

[169] T. Droubay and S. A. Chambers, ‘Surface-sensitive Fe 2$p$ photoemission spectra for $\alpha$-$Fe_2O_3$ (0001): The influence of symmetry and crystal-field strength’, Phys. Rev. B **64**, 205414 (2001).

[170] T. Kawamura, S. Endo, M. Kobayashi and S.-i. Narita, ‘Optical Study of $\alpha$-$Fe_2O_3$ under Ultrahigh Pressure’, J. Phys. Soc. Japan **53**, 3684–3686 (1984).

[171] N. J. Cherepy, D. B. Liston, J. A. Lovejoy, H. Deng and J. Z. Zhang, ‘Ultrafast Studies of Photoexcited Electron Dynamics in $\gamma$- and $\alpha$-$Fe_2O_3$ Semiconductor Nanoparticles’, J. Phys. Chem. B **102**, 770–776 (1998).

[172] A. G. Joly, J. R. Williams, S. A. Chambers, G. Xiong, W. P. Hess and D. M. Laman, 'Carrier dynamics in $\alpha$-$Fe_2O_3$ (0001) thin films and single crystals probed by femtosecond transient absorption and reflectivity', J. Appl. Phys. **99**, 053521 (2006).

[173] S. Sorenson, E. Driscoll, S. Haghighat and J. M. Dawlaty, 'Ultrafast Carrier Dynamics in Hematite Films: The Role of Photoexcited Electrons in the Transient Optical Response', J. Phys. Chem. C **118**, 23621–23626 (2014).

[174] A. V. Kozhevnikov, A. V. Lukoyanov, V. I. Anisimov and M. A. Korotin, 'Transition of Iron Ions from High-Spin to Low-Spin State and Pressure-Induced Insulator–Metal Transition in Hematite $Fe_2O_3$', J. Exp. Theor. Phys. **105**, 1035–1042 (2007).

[175] J. Kuneš, D. M. Korotin, M. A. Korotin, V. I. Anisimov and P. Werner, 'Pressure-Driven Metal-Insulator Transition in Hematite from Dynamical Mean-Field Theory', Phys. Rev. Lett. **102**, 146402 (2009).

[176] D. Hayes, R. G. Hadt, J. D. Emery, A. A. Cordones, A. B. F. Martinson, M. L. Shelby, K. A. Fransted, P. D. Dahlberg, J. Hong, X. Zhang, Q. Kong, R. W. Schoenlein and L. X. Chen, 'Electronic and nuclear contributions to time-resolved optical and X-ray absorption spectra of hematite and insights into photoelectrochemical performance', Energy Environ. Sci. **9**, 3754–3769 (2016).

[177] J. Vura-Weis, C.-M. Jiang, C. Liu, H. Gao, J. M. Lucas, F. M. F. de Groot, P. Yang, A. P. Alivisatos and S. R. Leone, 'Femtosecond $M_{2,3}$-Edge Spectroscopy of Transition-Metal Oxides: Photoinduced Oxidation State Change in $\alpha$-$Fe_2O_3$', J. Phys. Chem. Lett. **4**, 3667–3671 (2013).

[178] J. Husek, A. Cirri, S. Biswas and L. R. Baker, 'Surface electron dynamics in hematite ($\alpha$-$Fe_2O_3$): correlation between ultrafast surface electron trapping and small polaron formation', Chem. Sci. **8**, 8170–8178 (2017).

[179] S. Biswas, J. Husek and L. R. Baker, 'Elucidating ultrafast electron dynamics at surfaces using extreme ultraviolet (XUV) reflection–absorption spectroscopy', Chem. Commun. **54**, 4216–4230 (2018).

[180] L. M. Carneiro, S. K. Cushing, C. Liu, Y. Su, P. Yang, A. P. Alivisatos and S. R. Leone, 'Excitation-wavelength-dependent small polaron trapping of photoexcited carriers in $\alpha$-$Fe_2O_3$', Nat. Mater. **16**, 819–825 (2017).

[181] D. L. A. de Faria, S. Venâncio Silva and M. T. de Oliveira, 'Raman Microspectroscopy of Some Iron Oxides and Oxyhydroxides', J. Raman Spectrosc. **28**, 873–878 (1997).

[182] C. T. Chen and B. D. Cahan, ‘Visible and ultraviolet optical properties of single-crystal and polycrystalline hematite measured by spectroscopic ellipsometry’, J. Opt. Soc. Am. **71**, 932–934 (1981).

[183] K. Mörl, U. Röpke, B. Knappe, J. Lehmann, R. Perthel and H. Schröder, ‘Optical properties of sputtered $Fe_2O_3$ films’, Thin Solid Films **60**, 49–53 (1979).

[184] A. Leitenstorfer, C. Fürst, A. Laubereau, W. Kaiser, G. Tränkle and G. Weimann, ‘Femtosecond Carrier Dynamics in GaAs Far from Equilibrium’, Phys. Rev. Lett. **76**, 1545–1548 (1996).

[185] L. Perfetti, P. A. Loukakos, M. Lisowski, U. Bovensiepen, H. Eisaki and M. Wolf, ‘Ultrafast Electron Relaxation in Superconducting $Bi_2Sr_2CaCu_2O_{8+\delta}$ by Time-Resolved Photoelectron Spectroscopy’, Phys. Rev. Lett. **99**, 197001 (2007).

[186] B. K. Ridley, *Quantum Processes in Semiconductors*, 5th ed. (Oxford University Press, Oxford, 2013).

# List of abbreviations

| | |
|---|---|
| BBO | Beta-barium borate, $\beta$-$BaB_2O_4$ |
| CDW | Charge density wave |
| DAC | Diamond anvil cell |
| DFG | Difference frequency generation |
| DFT | Density functional theory |
| DMFT | Dynamical mean-field theory |
| DOS | Density of states |
| FEL | Free electron laser |
| FWHM | Full width at half maximum |
| HS | High-spin |
| IMT | Insulator-to-metal transition |
| IR | Infrared |
| LHB | Lower Hubbard band |
| LS | Low-spin |
| MCT | Mercury cadmium telluride |
| MIR | Mid-infrared |
| NIR | Near-infrared |
| OPA | Optical parametric amplifier |
| PES | Photoemission spectroscopy |
| PLD | Periodic lattice distortion |

| | |
|---|---|
| QP | Quasiparticle peak |
| RegA | Regenerative amplifier |
| SHG | Second harmonic generation |
| SPT | Structural phase transition |
| UED | Ultrafast electron diffraction |
| UHB | Upper Hubbard band |
| UV | Ultraviolet |
| WLS | Weakly localized states |
| XANES | X-ray absorption near-edge structure |
| XAS | X-ray absorption spectroscopy |
| XRD | X-ray diffraction |

# Publications

## Papers and Proceedings

- **J. M. Braun**, H. Schneider, M. Helm, R. Mirek, L. A. Boatner, R. E. Marvel, R. F. Haglund and A. Pashkin,
  *Ultrafast response of photoexcited carriers in* $VO_2$ *at high-pressure*,
  New Journal of Physics **20**, 083003 (2018).
  DOI: `http://doi.org/10.1088/1367-2630/aad4ef`

- **J. M. Braun**, H. Schneider, M. Helm, R. Mirek, L. A. Boatner, R. E. Marvel, R. F. Haglund and A. Pashkin,
  *Optical Pump – THz Probe Response of* $VO_2$ *under High Pressure*,
  Proceedings of the XXI International Conference on Ultrafast Phenomena, 15.-20.07.2018, Hamburg, Germany (to be published by EPJ Web of Conferences).

## Conference talks

- **J. M. Braun**, H. Schneider, M. Helm, R. Mirek, L. A. Boatner, R. E. Marvel, R. F. Haglund and A. Pashkin,
  *Pressure-induced insulator-to-metal transition in* $VO_2$ *studied by near-infrared pump – mid-infrared probe spectroscopy*,
  55th European High Pressure Research Group (EHPRG) Meeting on High Pressure Science and Technology, 03.-08.09.2017, Poznań, Poland

- **J. M. Braun**, H. Schneider, M. Helm, R. Mirek, L. A. Boatner, R. E. Marvel, R. F. Haglund and A. Pashkin,
  *Pressure-Induced Metallization in* $VO_2$ *Studied by Optical Pump – THz Probe Spectroscopy*,
  Conference on Lasers and Electro-Optics (CLEO), 14.-19.05.2017, San Jose, USA

- **J. M. Braun**, H. Schneider, M. Helm, R. Mirek, L. A. Boatner, R. E. Marvel, R. F. Haglund and A. Pashkin,

*Bandwidth-controlled metallization in pressurized $VO_2$ revealed by optical pump – THz probe spectroscopy*,
Conference on Optical Terahertz Science and Technology (OTST), 02.-07.04.2017, London, United Kingdom

- **J. M. Braun**, H. Schneider, M. Helm, R. Mirek, L. A. Boatner, R. E. Marvel, R. F. Haglund and A. Pashkin,
  *The nature of the pressure-induced metallization in $VO_2$*,
  DPG-Frühjahrstagung 2017, 19.-24.03.2017, Dresden, Germany

- **J. M. Braun**, J. F. Schmidt, D. V. Seletskiy, H. Schneider, M. Helm and A. Pashkin,
  *Ultrafast nonlinear response of GaAs under high pressures*,
  DPG-Frühjahrstagung 2016, 06.-11.03.2016, Regensburg, Germany

## Conference posters

- **J. M. Braun**, H. Schneider, M. Helm, R. Mirek, L. A. Boatner, R. E. Marvel, R. F. Haglund and A. Pashkin,
  *Ultrafast dynamics in $VO_2$ under high pressures*,
  NextGen@Helmholtz 2016 Conference, 28.-30.09.2016, Braunschweig, Germany

- **J. M. Braun**, H. Schneider, M. Helm, R. Mirek, L. A. Boatner, R. E. Marvel, R. F. Haglund and A. Pashkin,
  *Ultrafast dynamics in $VO_2$ under high pressures*,
  54th European High Pressure Research Group (EHPRG) International Meeting on High Pressure Science and Technology, 04.-09.09.2016, Bayreuth, Germany

- **J. M. Braun**, J. F. Schmidt, D. V. Seletskiy, H. Schneider, M. Helm and A. Pashkin,
  *Ultrafast nonlinear response of GaAs under high pressures*,
  Joint AIRAPT-25th & EHPRG-53rd International Conference on High Pressure Science and Technology, 30.08.-04.09.2015, Madrid, Spain

- **J. M. Braun**, J. F. Schmidt, D. V. Seletskiy, H. Schneider, M. Helm and A. Pashkin,
  *Ultrafast nonlinear response of GaAs under high pressures*,
  German THz Conference 2015, 08.-10.06.2015, Dresden, Germany

- J. Tauch, **J. M. Braun**, J. Keller, C. Hinz, J. Haase, D. V. Seletskiy, A. Leitenstorfer and A. Pashkin,
  *Pressure-induced shift of energy levels and structural phase transition in CdSe/ZnS quantum dots*,
  DPG-Frühjahrstagung 2015, 15.-20.03.2015, Berlin, Germany
- J. Tauch, **J. M. Braun**, J. Keller, C. Hinz, J. Haase, D. V. Seletskiy, A. Leitenstorfer and A. Pashkin,
  *Pressure-induced shift of energy levels and structural phase transition in CdSe/ZnS quantum dots*,
  Pressure and Strain Effects in Correlated Electron Materials, 06.-10.10.2014, Dresden, Germany

## Other scientific written publications

- **Johannes M. Braun** und Mario Hirt,
  *„Ein Königreich für einen Mühldorfer!“ Ein bühnentechnisches Genie des 19. Jahrhunderts in Bayreuth*, in:
  Universität Bayreuth, Bayerische Verwaltung der staatlichen Schlösser, Gärten und Seen, Historischer Verein für Oberfranken (Hrsg.). Sammelband anlässlich der Wiedereröffnung des Markgräflichen Opernhauses Bayreuth (in Drucklegung)
- **Johannes Braun** und Mario Hirt,
  *Hightech des 18. Jahrhunderts. Rekonstruktion der barocken Bühnentechnik des Markgräflichen Opernhauses zu Bayreuth*,
  Shaker, Aachen 2009

# Danksagung

Zum Gelingen dieser Arbeit haben viele Personen beigetragen, denen ich herzlich danken möchte.

Mein Dank gilt zuvorderst meinem wissenschaftlichen Betreuerteam unter der Leitung von Herrn Prof. Dr. Manfred Helm. Letzterem danke ich insbesondere für die Möglichkeit, an einer spannenden wie herausfordernden Aufgabenstellung zu arbeiten, für das technischen Hürden und Verzögerungen zum Trotz fortwährend entgegengebrachte Vertrauen, seine auch kurzfristig stets für Diskussionen offenen Ohren, sowie sein hilfreiches, präzise angebrachtes Feedback. Aufs herzlichste danke ich Herrn Dr. Alexej Pashkin. Nicht nur, dass er ein breites Expertenwissen hat und es ohne ihn dieses Projekt nicht gegeben hätte – er hat die Mittel eingeworben – es war für mich eine große Freude mit Alexej zusammenarbeiten zu dürfen. Danke für die vielen kleinen und großen Hilfen mit Rat und Tat, beherztes, offenes Feedback, die vorgelebte (für Hochdruckexperimente essentielle) grenzenlose Geduld, seine motivierend-begeisternde Art. Ich nehme davon gerne weit mehr mit als physikalische Erkenntnisgewinne und beglückwünsche all jene, die noch in den Genuss ähnlicher Erfahrung kommen. Herrn Dr. Harald Schneider danke ich für nützliche Ratschläge und Lektorentätigkeiten, sowie seine freundliche, wertschätzende Art, die den Umgang in der Spektroskopie-Gruppe prägt.

Unseren Kooperationspartnern sei herzlich für ihre nachdrückliche Unterstützung gedankt. Herrn Prof. Dr. Lynn A. Boatner vom Oak Ridge National Laboratory, USA, Herrn Dr. Robert E. Marvel und Herrn Prof. Dr. Richard F. Haglund von der Vanderbilt University, USA, danke ich für wiederholte Lieferungen hochqualitativer $VO_2$ Proben. Rafał Mirek von der University of Warsaw danke ich für seine Assistenz bei Aufnahme der ersten $VO_2$-Messreihe. Herrn Prof. Dr. Leonid Dubrovinsky, Herrn Timofey Fedotenko und Frau Dariia Simonova vom Bayerischen Geoinstitut Bayreuth danke ich für die Bereitstellung hochqualitativer $Fe_2O_3$ Proben und die wiederholte Befüllung und Überlassung einer ihrer BX90 Druckzellen.

Für hilfreiche Diskussionen danke ich den Herren Prof. Dr. Alfred Leitenstorfer von der Universität Konstanz und Prof. Dr. Peter Oppeneer von der Uppsala Universitet.

Herrn Prof. Dr. Jure Demsar danke ich für die Übernahme des Zweitgutachtens dieser Arbeit.

Für die gute Zusammenarbeit, Abstimmung und gegenseitige Hilfe möchte ich meinen Laborkollegen, den Herren Johannes Schmidt, Markus Hähnel, Ivan Fotev, sowie Frau Si Shan ausdrücklich danken. Besonders erwähnenswert ist dabei die von Herrn Markus Hähnel programmierte Messsoftware THz-Shaker. Dem ELBE Team und insbesondere den Herren Dr. Mike Klopf und Dr. Wolfgang Seidel danke ich für gute FEL-Strahlzeiten. Des Weiteren bedanke ich mich bei Herrn Dr. Stephan Winnerl, Frau Uta Lucchesi, den Herren Dr. Rakesh Rana und Dr. Jacob König-Otto, sowie Frau Leila Balaghi für physikalische und technische Hilfen.

Der gesamten Spektroskopie-Gruppe, die Alumni eingeschlossen, bin ich außerordentlich dankbar für die vielen bereichernden Gespräche und Diskussionen, die angenehme Arbeitsatmosphäre und das freundschaftliche Miteinander.

Größten Dank schulde ich aber meinen Eltern, die mir das Studium der Physik überhaupt erst ermöglicht haben und die zusammen mit meinem Bruder und meinen Freunden mich stets unterstützt haben.

# Versicherung

Hiermit versichere ich, dass ich die vorliegende Arbeit ohne unzulässige Hilfe Dritter und ohne Benutzung anderer als der angegebenen Hilfsmittel angefertigt habe; die aus fremden Quellen direkt oder indirekt übernommenen Gedanken sind als solche kenntlich gemacht. Die Arbeit wurde bisher weder im Inland noch im Ausland in gleicher oder ähnlicher Form einer anderen Prüfungsbehörde vorgelegt.

Diese Dissertation wurde am Institut für Ionenstrahlphysik und Materialforschung des Helmholtz-Zentrum Dresden-Rossendorf (HZDR) unter der wissenschaftlichen Betreuung von Prof. Dr. Manfred Helm, Professor am Institut für Angewandte Physik der Technischen Universität Dresden, angefertigt.

Ich erkenne die Promotionsordnung des Bereichs Mathematik und Naturwissenschaften der Technischen Universität Dresden in der gültigen Fassung vom 23.02.2011 an.

Ferner erkläre ich, noch nie ein Promotionsverfahren eröffnet zu haben.

Dresden, den 19.12.2018

Johannes M. Braun

Bautzner Landstr. 400
01328 Dresden, Germany
Tel. +49 351 260-3287
Fax +49 351 260-3285
a.pashkin@hzdr.de
http://www.hzdr.de